UC Merced

UC Merced Electronic Theses and Dissertations

Title

MODELING OF SURFACE CHEMICAL REACTIONS AT THE ATOMISTIC LEVEL

Permalink

https://escholarship.org/uc/item/9qk5g9q2

Author

Romero Garcia, Sergio

Publication Date

2024

Copyright Information

This work is made available under the terms of a Creative Commons Attribution-NonCommercial-NoDerivatives License, available at https://creativecommons.org/licenses/by-nc-nd/4.0/

Peer reviewed|Thesis/dissertation

eScholarship.org Powered by the California Digital Library
University of California

UNIVERSITY OF CALIFORNIA, MERCED

MODELING OF SURFACE CHEMICAL REACTIONS AT THE ATOMISTIC LEVEL

A dissertation submitted in partial satisfaction of the
requirements for the degree
Doctor of Philosophy

in

Materials and Biomaterials Science and Engineering

by

Sergio Romero Garcia

Committee in charge:

Professor Roberto Andresen Eguiluz, Chair
Professor Ashlie Martini, Advisor
Professor David Strubbe
Professor Mehmet Baykara

2024

Copyright
Sergio Romero Garcia, 2024
All rights reserved.

The dissertation of Sergio Romero Garcia is approved, and it is acceptable in quality and form for publication on microfilm and electronically:

(Professor Ashlie Martini, Advisor)

(Professor David Strubbe)

(Professor Mehmet Baykara)

(Professor Roberto Andresen Eguiluz, Chair)

University of California, Merced

2024

DEDICATION

I dedicate this dissertation to my wife Kelsey Romero, for her unconditional love and constant support to keep moving forward despite the adversities. My children Liliana & Nikolas, whose curiosity is an inspiration to keep learning. My sister Natalia, who has loved us unconditionally during this journey. My parents Marco Romero & Rosario Garcia, for their sacrifice, support, and encouragement to achieve more than what society expected from me. My parents Simeon & Patricia Dahl, for opening their doors and creating a safe space for me to feel loved and supported. My brother Rafael Vasconcellos, for the fun times, encouragement, and constant support.

Gracias a su apoyo he podido "torcerle el osico al destino".

EPIGRAPH

I learned not to try to convince anyone. The work of convincing is a lack of respect, it is an attempt to colonize the other

—José Saramago

TABLE OF CONTENTS

Signature Page . . . iii

Dedication . . . iv

Epigraph . . . v

Table of Contents . . . vi

List of Figures . . . viii

List of Tables . . . xiv

Acknowledgements . . . xv

Vita and Publications . . . xvii

Abstract . . . xix

Chapter 1 Introduction . . . 1
1.1 Surface Science . . . 1
1.2 Surface Coatings as Solid Lubricants . . . 2
1.3 Sputtering Deposition of Surface Coatings . . . 3
1.4 Simulation Techniques for Modeling Sputtering Deposition . . . 6
1.5 Surface Functionalization for On-Surface Mechanochemistry . . . 7
1.6 Modeling Surface Functionalization for Mechanochemistry . . . 9
1.7 Dissertation Outline . . . 10

Chapter 2 Ni-doped MoS_2 Dry Film Lubricant Life . . . 12
2.1 Introduction . . . 12
2.2 Methods . . . 15
2.3 Results and Discussion . . . 17
2.4 Conclusions . . . 30

Chapter 3 Molecular Dynamics Simulations of Undoped and Ni-doped MoS_2 Dry Film Lubricants . . . 32
3.1 Introduction . . . 32
3.2 Methods . . . 35
3.2.1 Deposition and Annealing to Evaluate the Potential . . . 35
3.2.2 Sputtering Deposition at Different Temperatures and Ni Concentrations . . . 36
3.2.3 Effect of Ni Concentration on DFL Shear Behavior . . . 39
3.3 Results and Discussion . . . 39

3.3.1 Deposition and Annealing to Evaluate the Potential . . . 39
3.3.2 Sputtering Deposition at Different Temperatures and Ni Concentrations . . . 41
3.3.3 Effect of Ni Concentration on DFL Shear Behavior . . . 45
3.4 Conclusions . . . 62

Chapter 4 Surface Functionalization for Mechanochemical Studies . . . 63
4.1 Introduction . . . 63
4.2 Methods . . . 64
4.3 Results and Discussion . . . 68
4.3.1 Reactive Simulations of Silica Functionalization with Aromatic Hydrocarbons . . . 68
4.3.2 Acceleration of Diels-Alder Reactions by Mechanical Distortion . . . 75
4.4 Conclusions . . . 82

Chapter 5 Summary and Future Work . . . 84
5.1 Summary . . . 84
5.2 Future Work . . . 86
5.2.1 Modeling MoS_2 DFLs . . . 86
5.2.2 Surface Mechanochemistry . . . 87
5.2.3 Simulation Timescales . . . 87
5.3 Concluding Remarks . . . 88

LIST OF FIGURES

Figure 1.1: Schematic of the sputtering deposition sub-processes. There is an initial cathode bombardment with ions that allows for bond breaking of atoms/molecules from the bulk material. The sputtered elements travel towards the substrate at high energies that are reduced due to gas phase collisions with inert ions and other sputtered atoms/molecules. Finally, sputtered atoms are deposited on the substrate forming a thin film. 4

Figure 2.1: SEM micrographs of (a) undoped and (b) Ni-doped MoS_2 coating morphologies showing columnar structures consistent with Type I coatings and flat tops resulting from burnishing. 17

Figure 2.2: Representative CoF traces at (a) 300 MPa and 1 m/s (b) 500 MPa and 0.77 m/s (c) 800 MPa and 0.44 m/s, and (d) 1100 MPa at 0.1 m/s for undoped and Ni-doped MoS_2 coatings run until coating failure. . . 18

Figure 2.3: EDS compositional maps showing partially worn (left wear track), unworn (center region) and fully worn (right wear track) regions of undoped MoS_2 coating. The partial and fully worn tracks were generated in sliding tests at 300 MPa contact pressure after 18,000 and 80,000 cycles, respectively. 19

Figure 2.4: EDS compositional maps showing two fully worn wear tracks and unworn regions on a Ni-doped MoS_2 coating. The left and right tracks were generated in sliding tests at 500 MPa contact pressure after 34,000 and 43,000 cycles, respectively. 19

Figure 2.5: Wear life of undoped and Ni-doped MoS_2 at different contact pressure / sliding speed conditions. The results are plotted against pressure on the abscissa, but the speed is also different for each case. Ni dopant improves wear life compared to the undoped samples at low pressures. 20

Figure 2.6: Wear profiles for (a) undoped MoS_2 at 300 MPa and 1 m/s, (b) undoped MoS_2 at 1100 MPa and 0.1 m/s, (c) Ni-doped MoS_2 at 300 MPa and 1 m/s, and (d) Ni-doped MoS_2 at 1100 MPa and 0.1 m/s showing the evolution of the wear tracks during the run-in tests. 21

Figure 2.7: Wear depth as a function of cycle during run-in tests at 300 and 1100 MPa contact pressures on undoped and Ni-doped MoS_2. Wear tracks are shallower (less wear) on the Ni-doped sample at both pressures. . . 23

Figure 2.8: SEM micrographs of (a) undoped and (b) doped MoS_2 coatings after 10 cycles at 1100 MPa and 0.1 m/s. The images on the right show close-up views of the partially worn material. These images show representative features where the undoped coatings exhibit cracking while the doped coatings exhibit cracking and delamination. 24

Figure 2.9: SEM micrographs of the regions between the cracked or delaminated columnar zone for (a) undoped and (b) Ni-doped MoS_2 coating after 10 cycles at 1100 MPa and 0.1 m/s. The material underneath the failed columnar zone is distinctly rougher for the Ni-doped coating. 25
Figure 2.10: SEM micrographs of dense flakes of MoS_2 within or near the wear track from run-in tests of (a and b) Ni-doped coatings after 10 cycles, (c) an undoped coating after 250 cycles, and (d) a Ni-doped coating after 250 cycles. All images from tests at 1100 MPa and 0.1 m/s. . . . 26
Figure 2.11: Wear width as a function of cycle during run-in tests at 300 and 1100 MPa contact pressures on undoped and Ni-doped MoS_2. Wear tracks widths are larger at the higher pressures. In all cases, the width increases gradually with sliding cycles. 27
Figure 2.12: (a) Average lateral force during progressive load scratch tests on doped and undoped samples. Lines represent the average of three tests and the band represents standard deviation. SEM images and Mo/Fe signals from EDS taken at the start of the test on (b) undoped and (c) Ni-doped coatings. 28
Figure 2.13: SEM micrographs of (a) undoped and (b) Ni-doped MoS_2 coatings during a representative progressive load scratch test (at approximately 62 N load). The doped and undoped coatings are distinctly different at the edges of the wear tracks (for example, the regions identified by the dashed lines). 29
Figure 2.14: Schematic illustration of the proposed wear process that occurs through densification followed by cracking and, for Ni-doped MoS_2, delamination. The flakes generated during the cracking and/or delamination process lubricate the contact subsequently as they are continuously supplied as the wear track widens and more flakes are made available to facilitate sliding. 30

Figure 3.1: Snapshot representations of the simulations steps: (A) sputtering deposition, (B) equilibration, (C) compression, and (D) shearing of the 300 K, 10% Ni doped MoS_2 thin film. Red, yellow, and green spheres represent Ni, S, and Mo atoms respectively 37
Figure 3.3: Radial distribution functions for (a) 2H MoS_2 substrate before deposition and (b) system after annealing. Similar peak locations for Ni–S and Mo–S, and for Ni–Mo and Mo–Mo, indicate occupation of Mo sites by Ni after annealing. 41
Figure 3.5: Snapshot representations of (A) undoped, (B) 2 % Ni, (C) 10 % Ni, and (D) 15 % Ni doped MoS_2 depositions at 670 K after equilibration. Colors are same as those defined in Fig. 1 of the main paper. 42

Figure 3.2: Side-view snapshots (top) and radial distribution function (bottom) of the model system, (I) before deposition, (II) at the end of the deposition, and (III) at the end of the annealing stage. A clear transition from amorphous to crystalline is observed (II) → (III). Spheres represent S (yellow), Mo (green), and Ni (red) atoms. The black lines in the top snapshots correspond to the periodic boundaries of the cell during the annealing stage. 48
Figure 3.4: Snapshot representations of (A) undoped, (B) 2 % Ni doped, (C) 10 % Ni doped, and (D) 15 % Ni doped MoS_2 depositions at 300 K after equilibration. 49
Figure 3.6: (A) Snapshot representation of binned regions used to calculate vertical position dependent density. (B) Average density of all bins where the error bars are the standard deviation for each deposition at 300K and 670K. 50
Figure 3.7: Time-averaged density with respect to vertical position for all Ni percentage deposited films at (A) 300 K and (B) 670 K. 50
Figure 3.8: Time-averaged crystallinity with respect to vertical position for all Ni percentage deposited films at (A) 300 K and (B) 670 K. 51
Figure 3.9: (A) Snapshot of the crystal formation during deposition at different times where crystalline atoms are shown in blue and amorphous atoms are shown in partially transparent yellow. (B) Mean crystallinity calculated for the last 0.5 ns of the post-deposition equilibration. 51
Figure 3.10: Radial distribution function analysis for Mo-S, Ni-S, and Mo-Ni atom pairs at (A) 300 K and (B) 670 K. 52
Figure 3.11: Evolution of Ni cluster sizes over time for deposition temperatures 300 and 670 K. Color bars represent the log function of the percentage of a given size. 52
Figure 3.12: Snapshot representations of Ni atoms at time 1 ns for equilibrated depositions at 300 K. Red, yellow and green spheres represent Ni, S, and Mo atoms, respectively, with non-substrate Mo and S atoms shown faded to emphasize the Ni positions and clustering. 53
Figure 3.13: Time-averaged Ni cluster sizes distribution for deposition at (A) 300 K and (B) 670 K. Shaded regions correspond to skewed distributions fitted to the cluster size data. 54
Figure 3.14: Evolution of shear stress during shearing of films sputter deposited at 300 K. 55
Figure 3.15: Snapshots of the structural evolution at different times (0, 1, and 2.6 ns) for (A) 0%, (B) 2%, (C) 10%, and (D) 15% Ni doped films deposited at 300K during shear. 56
Figure 3.16: Snapshot representation of (A) 0%, (B) 2 %, (C) 10%, and (D) 15% Ni-doped films during shearing at time 2.4 ns. The color represents the x-direction displacement magnitude of the atoms. 57

Figure 3.17: Evolution of density as a function of vertical position and time for the shearing simulations (after compression is complete) with color map representing the log of the density for (A) 0 %, (B) 2%, (C) 10%, and (D) 15% Ni doped MoS_2 films. 58
Figure 3.18: Evolution of crystallinity as a function of vertical position and time during shearing simulations with color map representing the log of the percent crystalline material for (A) 0 %, (B) 2%, (C) 10%, and (D) 15% Ni doped MoS_2 films. 59
Figure 3.19: Snapshot of the (A) 2% and (B) 10% Ni doped films after 2.4 ns of shearing. Red spheres represent Ni atoms with Mo and S atoms shown translucent green and yellow colors respectively. For both cases the Ni atoms are shown to locate outside of the inner core of the wear particle. 60
Figure 3.20: Abundance plot of the evolution of Ni cluster sizes over time during shearing simulations with color map representing the log of the Ni cluster size (number of Ni atoms) for (A) 2 %, (B) 10%, and (C) 15%. 60
Figure 3.21: (A) Snapshot of the 10% Ni doped film after 2.4 ns of shearing where atoms are colored based on crystallinity. Blue spheres represent atoms in a crystal, translucent spheres are atoms in an amorphous configuration, and Ni atoms are shown as red spheres. The cross-sectional planes in the z-x directions for (B) 10% and (C) 2% Ni concentrations show different simulation frames illustrating the movement of Ni atoms and the formation of the lubricious wear particle during shearing. For both Ni concentrations, the particle shows a crystalline core and an amorphous outer shell with Ni atoms. 61

Figure 4.1: (A) Schematic representations of the aromatic hydrocarbons used as reactants in the simulations. Representative side-view snapshots of the model system with phenyl (B) before and (C) after covalent functionalization. Sphere colors correspond to: gray - carbon, white - hydrogen, tan - silicon in the silanols, purple - silicon in the silica, red - oxygen in the silanols, blue - oxygen in the silica. 65
Figure 4.2: RDFs for Si-O, O-O, and Si-Si distances for (top) the substrate used in the simulation and (bottom) a reference cristobalite SiO_2. The simulation substrate RDF peaks are broad and with no long-range order, characteristic of an amorphous materials. The bottom RDF for the cristobalite SiO_2 has the sharp well-defined peaks associated with a crystal structure. 66
Figure 4.3: Extended simulations for select molecules and temperatures showing surface density steady state is achieved within the simulation times of 0.2 ns. 67
Figure 4.4: Schematic representations of theoretical surface density for (A) phenyl, (B) naphthyl, and (C) anthracenyl aromatic hydrocarbons 69

Figure 4.5: Time evolution of the surface density for phenyl, naphthyl, and anthracenyl chemisorbed on an amorphous silica surface from simulations at (A) 300, (B) 400, and (C) 500 K. For each data set, the dark line is the mean and the shaded region is the standard deviation of three independent simulations. (D) The steady-state surface density for each case is averaged over the last 0.1 ns of the simulations, where error bars reflect the standard deviation. 71
Figure 4.6: Close up snapshots of the three possible bonding configurations between a silanol and the silica substrate that differ based on the number of $Si_{silanol}$–O_{silica} bonds, shown using naphthyl as reference: (A) one bond (1-O), (B) two bonds (2-O), and (C) three bonds (3-O). Spheres representing atoms other than those in the representative silanols of interest are faded. (D) Distribution of the number of bonds between Si in the substrate and O in the silanol averaged over the three simulations at three temperatures for each silanol as a percentage of the total number of silanols in the system. The error bars represent the standard deviation. 72
Figure 4.7: (A) Representative snapshot of phenyl showing the definition of the angle used to quantify the tilt of the silanol with respect to the surface-normal direction. Spheres representing atoms other than those in the representative silanol of interest are faded. (B) Distribution of tilt angles from all observed bonds and all temperatures/simulations between 0.1 and 0.2 ns of simulation time. Only slight differences between phenyl, naphthyl, and anthracenyl are observed, but smaller angles are preferred for the smaller silanols. 73
Figure 4.8: Two point vector representations of the silanol in the xy plane from representative simulations of (A) phenyl, (B) naphthyl, and (C) anthracenyl. The two point coordinates are taken from the edge carbons on the long axis of the silanol, as shown in the insets. The x- and y-axes are scaled by the total length of the simulation box in each direction. Radial distribution functions of the distance between Si atoms in (D) phenyl, (E) naphthyl, and (F) anthracenyl for all simulations. 74
Figure 4.9: (A) Representative snapshot of a two-naphthl aggregate. (B) Distributions of aggregate size (quantified by number of bonded silanols) for each silanol calculated from trajectory data between 0.1 and 0.2 ns. . . 75
Figure 4.10: Side-view snapshots of the anthracene deposition simulation, from left to right, at in the initial configuration, after 300 ps of equilibration, and after removing all anthracene molecules not bonded to the surface. 76

Figure 4.11: (A) Time evolution of the area density of anthracene molecules chemisorbed on the SiO_2 surface at 300, 350, and 400 K and (B) corresponding average steady-state density at each temperature, where error bars reflect the standard deviation of the data over the last 60 ps of the simulation. The average area density across all three temperatures as the system nears steady state is 1.20 ± 0.08 mol·nm^2. Error is reported as the standard deviation of the areal density at the three different temperatures. 77
Figure 4.12: Analysis of bonding between anthracene and the SiO_2 substrate. (A) Distribution of number of number of bonds between Si in the anthracene and O on the substrate. The most common coIormation is two oxygen bonds (2-O). Close up snapshots of the three possible bonding configurations: (B) 1-O, (C) 2-O, and (D) 3-O. 77
Figure 4.13: Calculation of molecular spacing for (A) anthracene monolayer and (B) Diels-Alder adduct. 78
Figure 4.14: Calculation of molecular spacing from (A) Molecular Dynamics simulations of 9−anthracenyltrimethoxysilane molecules chemisorbed on to SiO_2 substrate. The pairwise distances for Si atoms was calculated for (B) the closest neighbors within 12 Å cut−off−radius from the reference Si atom and (C) averaged over time once equilibrium had been reached at around 200 ps. 79
Figure 4.15: Snapshots of simulations of compression-driven bonding between maleimide and anthracene monolayers, (A) before applying pressure, (B) at 1.7 GPa, and (C) at 3.0 GPa. 79
Figure 4.16: (A) Distribution of bending angle in response to applied pressure in the simulations and representative snapshots of the molecule with the bending angle defined at (B) low and (C) high pressures. Compression causes the molecule to bend towards the surface. Error bars are reported as one standard deviation from the mean of three independent calculations. 80
Figure 4.17: (A) Distribution of force acting in the direction normal to the anthracene rings at equilibrium and in the low- and high-pressure cases. Error bars are reported as one standard deviation from the mean of three independent calculations. (B) Only part of the applied force, F_z, acts in the direction normal to the plane of the rings, F_N, and is approximated from the angle of the molecule with respect to the direction normal to the SiO_2 surface as $F_N = F_z \cos\theta$. 81
Figure 4.18: (A) Distribution of CCH angles for all molecules during the simulations. The average angle (dashed vertical lines) shift slightly left (away from the equilibrium, uncompressed value) with pressure, but the fraction of molecules with far-from-equilibrium angles increases with pressure. Representative snapshots of the anthracene during the compression simulations at (A) low and (B) high pressure with the CCH angle identified. 82

LIST OF TABLES

Table 2.1: Experimental parameters used in the ball-on-disk tests. High pressures are matched with low speed, and vice versa, to mimic the operating conditions of a gearing system. 16

Table 3.1: Composition of sputtered films by Ni-dopant from previous experimental measurements [118] used to define the model systems. 38
Table 3.2: Density and crystallinity averaged over the last 0.5 ns of the post-deposition equilibration stage. The "bulk" density and crystallinity correspond to the material at vertical positions between 2.0 and 4.0 nm. 44

Table 4.1: Summary of surface density values estimated based on molecule geometry, reactive MD simulations, and previous QCM measurements [134] . 70
Table 4.2: Bending angle, θ, and percentage of applied force, Fn/Fz, for different pressures and oxygen bond configurations. 81

ACKNOWLEDGEMENTS

I would like to express my deepest gratitude to my advisor, Professor Ashlie Martini, whose guidance and mentorship have been invaluable throughout this dissertation process. Her patience, dedication to research, and constant support made this PhD possible.

I also extend my sincerest appreciation to my committee members, Professors Andresen Eguiluz, Baykara, and Strubbe, for their thoughtful comments and suggestions that significantly enriched the final product.

Additionally, I would like to thank the members of the Center for Mechanical Control of Chemistry, including Dr. Zholdassov, Professor Braunschweig, and Professor Marianski, as well as other members who have contributed to my understanding of mechanochemistry's importance.

Lastly, I want to acknowledge the camaraderie and support I received from my peers at the Martini Research Group: Dr. Azhar Vellore, Dr. Arash Khajeh, Dr. Mohammad R. Vazirisereshk, Dr. Karen Mohammadtabar, Dr. Pawan Panwar, Daniel Sanchez Garrido, Dr. Quanpeng Yang, Fakhrul Hasan Bhuiyan, Andrew Velasquez, Dr. Ting Liu, Dr. Ingrid Padilla Espinosa. Their wisdom and unique personalities made this journey more enjoyable and meaningful.

The text of this dissertation includes reprints of the following previously published material:

1. Romero Garcia, Sergio, Faiyad, Abrar, and Martini, Ashlie. 2024. "Modeling Sputtering Deposition of MoS_2: Effect of Ni Doping on Nanostructure and Tribological Properties." *Computational Materials Science* (Submitted).

2. Romero Garcia, Sergio, Zholdassov, Yerzhan S., Braunschweig, Adam B., and Martini, Ashlie. 2023. "Reactive Simulations of Silica Functionalization with Aromatic Hydrocarbons." *Langmuir* 40 (1): 561–67. Copyright 2023 American Chemical Society.

3. Mohammadtabar, Karen, Guerrero, Enrique, Romero Garcia, Sergio, Shin, Yun Kyung, van Duin, Adri C. T., Strubbe, David A., and Martini, Ashlie. 2023. "Development and Application of a ReaxFF Reactive Force Field for Ni-Doped MoS_2." *Journal of Physical Chemistry C* 127 (25): 12171–83. Copyright 2023 American Chemical Society.

4. Zholdassov, Yerzhan S., Yuan, Li, Romero Garcia, Sergio, Kwok, Ryan W., Boscoboinik, Alejandro, Valles, Daniel J., Marianski, Mateusz, Martini, Ashlie, Carpick, Robert W., and Braunschweig, Adam B. 2023. "Acceleration of Diels-Alder Reactions by Mechanical Distortion." *Science* 380 (6649): 1053–58.

5. Vellore, Azhar, Romero Garcia, Sergio, Walters, Nicholas, Johnson, Duval A., Kennett, Andrew, Heverly, Matthew, and Martini, Ashlie. 2020. "Ni-Doped MoS_2 Dry Film Lubricant Life." *Advanced Materials Interfaces* 7 (22): 2001109. Copyright 2020 Wiley-VCH GmbH

The co-authors listed in these publications directed and supervised research which forms the basis for the dissertation.

EDUCATION

2019-2024	Ph. D. in Materials and Biomaterials Science and Engineering, University of California, Merced, CA, USA
2019-2023	M. S. in Materials and Biomaterials Science and Engineering, University of California, Merced, CA, USA
2011-2013	M. S in Mechanical Engineering, University of St Thomas, St Paul, MN, USA
2007-2011	B. S. in Physics, Augsburg University, Minneapolis, MN, USA

PUBLICATIONS

1. Romero Garcia, Sergio, Faiyad, Abrar, and Martini, Ashlie. 2024. "Modeling Sputtering Deposition of MoS2: Effect of Ni Doping on Nanostructure and Tribological Properties." *Computational Materials Science* (Submitted).

2. Romero Garcia, Sergio, Zholdassov, Yerzhan S., Braunschweig, Adam B., and Martini, Ashlie. 2023. "Reactive Simulations of Silica Functionalization with Aromatic Hydrocarbons." *Langmuir* 40 (1): 561–67.

3. Mohammadtabar, Karen, Guerrero, Enrique, Romero Garcia, Sergio, Shin, Yun Kyung, van Duin, Adri C. T., Strubbe, David A., and Martini, Ashlie. 2023. "Development and Application of a ReaxFF Reactive Force Field for Ni-Doped MoS_2." *Journal of Physical Chemistry C* 127 (25): 12171–83.

4. Zholdassov, Yerzhan S., Yuan, Li, Romero Garcia, Sergio, Kwok, Ryan W., Boscoboinik, Alejandro, Valles, Daniel J., Marianski, Mateusz, Martini, Ashlie, Carpick, Robert W., and Braunschweig, Adam B. 2023. "Acceleration of Diels-Alder Reactions by Mechanical Distortion." *Science* 380 (6649): 1053–58.

5. Vellore, Azhar, Romero Garcia, Sergio, Johnson, Duval A., and Martini, Ashlie. 2021. "Ambient and Nitrogen Environment Friction Data for Various Materials & Surface Treatments for Space Applications." *Tribology Letters* 69 (1): 10.

6. Vellore, Azhar, Romero Garcia, Sergio, Walters, Nicholas, Johnson, Duval A., Kennett, Andrew, Heverly, Matthew, and Martini, Ashlie. 2020. "Ni-Doped MoS_2 Dry Film Lubricant Life." *Advanced Materials Interfaces* 7 (22): 2001109.

7. Stark, John R., Romero Garcia, Sergio, Gorman, John M., Abraham, John P., and Sparrow, Ephraim M. 2016. "Modulated-Power Implantable Neuromodulation Devices and Their Impact on Surrounding Tissue Temperatures." *Journal of Biomedical Science and Engineering* 09 (12): 545–62.

WORK EXPERIENCE

Aug 2019-Present	Graduate Research Assistant, University of California Merced, Merced, CA
Jun 2022-Aug 2023	Summer Graduate Intern, Lawrence Livermore National Laboratory, Livermore, CA
Jun 2020-Aug 2020	Summer Graduate Intern, NASA Jet Propulsion Lab, Pasadena, CA
Jan 2017-Aug 2019	Mechanical Engineer II, Starkey Hearing Technologies, Eden Prairie, MN
Apr 2016-Dec 2016	Mechanical Engineer, Nonin Medical, Plymouth, MN
Oct 2012-Mar 2016	Mechanical Engineer, Banner Engineering, Plymouth, MN

PRESENTATIONS & AWARDS

Poster Presentation accepted for 2024 ACS Annual Meeting (March 2024).

Materials and Biomaterials Science and Engineering seminar speaker presentation on "Acceleration of Diels-Alder Reactions by Mechanical Distortion" (September 2023).

Presentation on "Modeling Sputtering Deposition of MoS_2: Effect of Sputtering Deposition on the Microstructure" at the STLE Annual Meeting (May 2022).

Gold award at 2022 STLE Annual Meeting student poster contest (May 2022).

Poster presentation accepted for 2021 STLE Annual Meeting (May 2021).

Poster presentation accepted for 2020 STLE Annual Meeting (May 2020-cancelled).

Online poster presentation on "Wear life of Ni-doped and undoped MoS_2" in Web Seminar Series in Tribology (WeSST 2020).

Presentation on "Ni-doped MoS_2 Dry Film Lubricant Life" in MACES Energy Efficiency Thrust Meeting (Fall 2020).

Recipient of MACES Fellowship (2019-2021).

Recipient of Travel fellowship for 2020 STLE conference.

Recipient of Augsburg College Presidential Scholarship (2007-2011).

ABSTRACT OF THE DISSERTATION

MODELING OF SURFACE CHEMICAL REACTIONS AT THE ATOMISTIC LEVEL

by

Sergio Romero Garcia

Doctor of Philosophy in Materials and Biomaterials Science and Engineering

University of California Merced, 2024

Professor Roberto Andresen Eguiluz, Chair

This dissertation investigates the chemical processes on surfaces, focusing on the growth of surface layers for applications in friction reduction using solid coatings and surface functionalization for investigations of mechanically driven chemical reactions.

First, we investigated how Ni doping affects the wear life of MoS_2 by conducting experimental studies on sputtered undoped and 7% Ni-doped dry film lubricants. The results showed that Ni-doping improves wear life at low contact pressures, attributed to larger MoS_2 debris in the wear track. Our findings suggest that wear life correlates more with the size of lubricious wear particles than with wear depth. A model was proposed to explain the differences between Ni-doped and undoped MoS_2 wear processes, emphasizing the need for atomic-level insights into the sputtering process and resulting DFL microstructure.

To address this, we used a recently developed reactive molecular dynamics potential parameterized for Mo/S/Ni to simulated sputtering deposition and annealing simulations. Then, deposition of MoS_2 with different Ni concentrations was simulated and the resulting films were analyzed for density, crystallinity, radial distribution function, and Ni-cluster formation. The highest density and crystallinity were observed just above the MoS_2 substrate, and larger Ni clusters were observed at higher Ni concentrations. Shearing simulations revealed that films with 2% and 10% Ni had lower shear stress at steady state compared to those with 0% and 15% Ni, due to the formation of lubricious wear particles with a crystalline core and amorphous, Ni-containing surfaces. This non-monotonic

dependence of tribological properties on Ni concentration provides insights for optimizing doped MoS_2 dry film lubricants.

To study surface functionalization, we simulated the covalent attachment of aromatic hydrocarbons to amorphous silica. Surface densities of silanol-terminated phenyl, naphthyl, and anthracenyl molecules were lower than geometrically predicted, decreasing faster with more aromatic rings. Analysis of bonding configurations, tilt angles, and local conformational ordering showed that surface density is influenced by the size and symmetry of the hydrocarbons. Compression simulations further provided insights into the deformation of immobilized aromatic hydrocarbons during mechanochemical processes.

This research offers valuable insights into the effect of deposition or functionalization processes and parameters on the properties of functional surfaces. By integrating theory and experimentation, the results advance our understanding of surface chemistry, guiding the design and optimization of materials for tribological and mechanochemical applications.

Chapter 1

Introduction

1.1 Surface Science

Surface science is the study of chemical and physical processes that occur at the interface of two material phases. From lubricants reducing wear in car engines to silicon transistors in computers, the role of surface science and engineering is critical in the development of new technologies. With engineering and scientific applications continuing to push the boundaries of what current materials are able to achieve, the development and implementation of experimental and computational material design tools is crucial to accelerating the discovery and implementation of new materials with tailored chemical and physical properties.

On-surface technological applications can be found in many fields, e.g., electronics [1], pharmaceutics [2], tribology [3], and catalytics [4]. This fertile ground of useful applications capable of tackling fabrication challenges related to energy and chemical waste can only be fully leveraged by understanding of the interplay between chemical reactions, material microstructure and surfaces. This understanding can be pursued via advanced experimental methods, e.g., atomic force microscopy, transmission electron microscopy, and tribometry. Such techniques have enabled characterization of material properties and the response of materials to dynamic conditions.

Experiments can also be complemented by computer simulations. It has been proposed that, by integrating the classical equations of motion produced by Newton and Hamilton, it is possible to model the dynamics of molecules. With the aid of high performance computing (HPC) techniques to solve classical and quantum dynamic equations within

accessible time frames, it is now possible to study the thermodynamics and kinetics of on-surface chemical and physical processes. Unlike experimental methods, which have limitations in characterizing materials at the nanoscale, nanoscale simulations do not face these constraints. The implementation of computational technologies such as molecular dynamics (MD) simulation and quantum mechanical methods (e.g., Ab-initio, Density Functional Theory) have allowed scientists to understand how microscopic processes, such as sputtering deposition, catalysis and lubrication, affect the surface properties of material systems.

This dissertation focuses on use of experiments and simulations to study three aspects of physical and chemical processes in surface science: surface coatings, i.e., solid lubricants, that interact with and protect sliding surfaces in tribological applications, sputtering deposition and shear of surface coatings, and surface functionalization for on-surface mechanochemistry.

1.2 Surface Coatings as Solid Lubricants

Solid lubricants are coating materials that reduce friction and wear between two surfaces in relative motion while being in a solid state themselves. Solid lubricants can be found as carbon-based (e.g., graphite and diamond like carbons (DLC)), transition metal dichacogenide compounds (e.g., MoS_2, WS_2), polymers (e.g.,PTFE), and soft metals (e.g., silver, tin, gold). These lubricants work by forming a thin, protective layer between the surfaces, which helps to minimize direct contact and frictional forces. Solid lubricants can operate effectively in extreme conditions, such as high temperatures, vacuum environments, or where traditional liquid lubricants may not be practical or feasible.

Among solid lubricants, transition metal dichalcogenides (TMDs) stand out for their exceptional lubricating properties. TMDs possess a unique layered structure consisting of sheets of transition metal atoms sandwiched between layers of chalcogen atoms. This layered arrangement allows for easy shear deformation within the material, resulting in low-friction behavior.

Furthermore, TMDs exhibit high shear strength, enabling them to withstand mechanical forces and maintain their lubricating properties over extended periods of use [3]. Their atomically smooth and relatively inert surfaces minimize adhesion between con-

tacting surfaces, further reducing frictional forces and preventing surface damage [5, 6]. Additionally, TMDs are chemically stable and resistant to oxidation and corrosion, making them suitable for use in a wide range of operating conditions.

The temperature stability of TMDs ensures their effectiveness over varying thermal environments, making them indispensable in applications where traditional lubricants may fail [7]. These exceptional properties make TMDs highly desirable solid lubricants in industries such as aerospace, automotive, manufacturing, and machinery, where reducing friction and wear are paramount for improving efficiency, reliability, and longevity of mechanical systems.

One of the most widely used TMDs for tribology is molybdenum disulfide (MoS_2). MoS_2 has a long history as a lubricant [8] and is currently used both in space and terrestrial applications as an additive in greases and lubricating oils, and as a dry film lubricant [3]. Dry film lubricants (DFLs), or solid lubricants, are preferred over liquid lubricants when operating conditions are extreme, e.g., very high or low temperature, vacuum or corrosive environments, or to prevent contamination of sensitive equipment [9–11].

Co-depositing or doping certain metals with MoS_2 is known to affect the coating microstructure and can alleviate the detrimental effects of humidity and oxygen on the tribological behavior of sputtered coatings. Dopants are believed to improve the tribological properties of sputtered MoS_2 films through different mechanisms, including increased oxidation resistance [12–14] and increased hardness, [15–21] depending on the dopant material used. Particularly for space applications, Ni is a preferred dopant [22] due to its ability to mitigate the increase of friction at low temperatures [23] and its low cost and availability [24]. However, how these changes in morphology due to Ni doping affect coating life is not fully understood.

1.3 Sputtering Deposition of Surface Coatings

There are different fabrication methods for growing MoS_2 dry films, with sputtering deposition being common for outer space lubrication applications where tight part tolerances, extreme environmental conditions and cost make the use of micron-thick dry film coatings ideal for instrumentation. The sputtering deposition process commonly involves a noble gas being excited to bombard a bulk target material. This highly energetic

interaction is strong enough to break the bonds in the material and release atoms and molecules with high energetic values in the direction of the substrate. It is at the surface of the substrate that the depositing atoms start forming bonds and layers of accumulated materials that can grow as far as a micron in height.

Since sputtering deposition is a complex process, when employing computational methods it is usually simulated in stages. The process can be divided in three sub-phases, each providing a partial picture of the total deposition process. Figure 1.1 shows the three phases within a sputtering deposition process: 1) ion bombardment, 2) sputtering, and 3) deposited film formation.

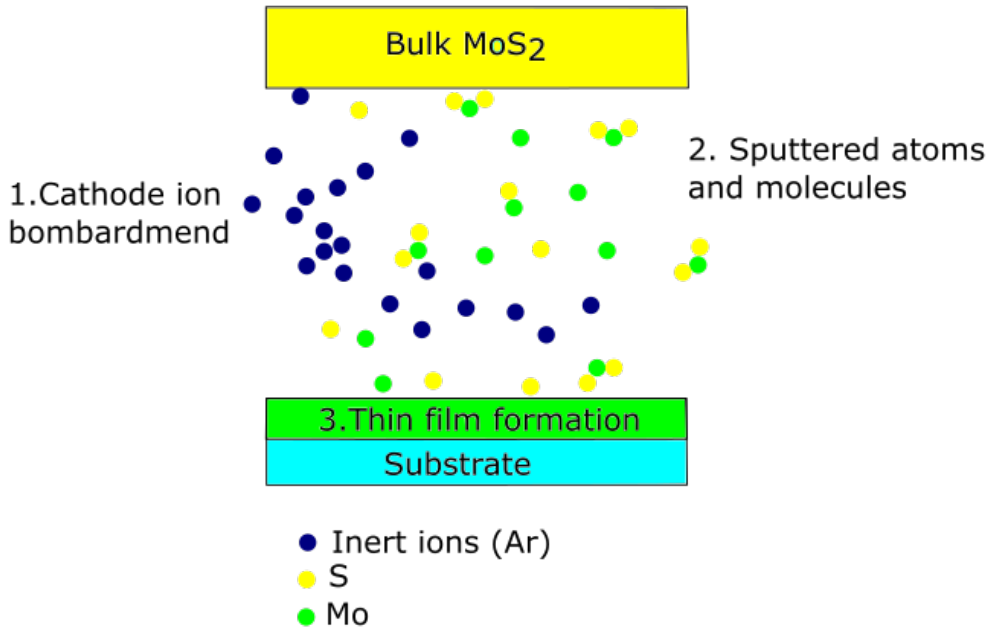


Figure 1.1: Schematic of the sputtering deposition sub-processes. There is an initial cathode bombardment with ions that allows for bond breaking of atoms/molecules from the bulk material. The sputtered elements travel towards the substrate at high energies that are reduced due to gas phase collisions with inert ions and other sputtered atoms/molecules. Finally, sputtered atoms are deposited on the substrate forming a thin film.

Aside from its tribological applications, sputtered deposited MoS_2 dry films are of great interest for catalytic and electronic applications in which the final microstructure of the deposited material is understood to affect its physical properties.

Sputtered MoS_2 can be found in three distinct polytypes such us 1T (1 layer-trigonal),

2H (2 layer-hexagonal) and 3R (3 layer-rhombohedral) [3] with 2H found naturally occurring as the most stable configuration. The different allotropies and morphologies of MoS_2 have different physical and chemical properties that are ideal for various applications. For instance, high crystallinity of a controlled number of monolayers with a low defect density is needed in a large deposition area to make sputtering a feasible method for electronic applications such as field effect transistor (FET) biosensors [25]. In catalytic applications, it has been proposed that edge termination (Type I) and controlled layer spacing makes MoS_2 a desirable material to study hydrogen evolution reactions in electrochemical water splitting [26].

It is clear that, to fully realize the potential of sputtered MoS_2 thin films, deposition processes need to be controllable and scalable. Experimental work has been performed to explore how the morphological, structural and electronic properties of MoS_2 thin films are affected by sputtering deposition. Kaindl and collaborators in 2017 [27] performed a comprehensive investigation of scalable physical vapour deposition (PVD) of MoS_2 films by magneto sputtering. Employing different characterization techniques (e.g., X-ray diffraction (XRD), electron scanning and spectroscopy) they found that room temperature (RT) deposited MoS_2 thin films are amorphous in nature and easily degrade in moderate laser annealing conditions. Alternatively, films deposited at 400 $^{\circ}C$ showed nano-crystalline grained surface morphology with better resistance to laser degradation. Another important finding was that the mass densities calculated for RT and 400 $^{\circ}C$ films were smaller than those previously reported for bulk MoS_2. This difference was attributed to structural imperfections in the MoS_2 layer evidenced by shifts in the peak positions in specular XRD. Despite the high process control of layer preparation, it is still an open question whether these imperfections are caused by the high kinetic energy of depositing ions bombarding the surface of the film or another process variable. However, this is at the limit of experimental characterization. This is where molecular dynamics simulation can play an important role in understanding the effect of sputtering deposition on structural imperfections and how experimental observations can be explained.

1.4 Simulation Techniques for Modeling Sputtering Deposition

In the study of film growth, there is greater emphasis on studying the deposition process (Fig. 1.1) and how atomic interactions and kinetics affect the formation of equilibrated film crystalites. For studies concerning the effect of sputtering on film formation, the processes at the cathode (bulk material) can be reduced to a constant flux of atoms randomly introduced into the simulation box and traveling in the direction of the substrate at a given velocity. This simplifies the model tremendously and enables simulations of sputtering and film growth using atomistic models.

In the case of sputtering deposition, an accurate description of bond breaking and bond formation is needed to understand how parameters such as temperature, pressure, incident kinetic energy among others can affect the atomic structure of the sputtered films. For such applications, the ReaxFF reactive force field has found success in accurately describing the geometry, stability and chemical bonds (e.g., bond dissociation, bond formation) of conjugate, non-conjugate and radical-containing compounds by calculating different partial energy contributions to the system energy as shown in equation 1.1:

$$E_{\mathbf{system}} = E_{\mathbf{bond}} + E_{\mathbf{over}} + E_{\mathbf{under}} + E_{\mathbf{val}} + E_{\mathbf{pen}} + E_{\mathbf{tors}} + E_{\mathbf{conj}} + E_{\mathbf{vdWaals}} + E_{\mathbf{Coulomb}} \quad (1.1)$$

Here $E_{\mathbf{bond}}$ deals with the bond order and bond energy, $E_{\mathbf{over}}$ & $E_{\mathbf{under}}$ over- and under-coordination energy components, $E_{\mathbf{val}}$ & $E_{\mathbf{tors}}$ & $E_{\mathbf{conj}}$ account for valence angles, torsion angles, and conjugate systems, respectively, and $E_{\mathbf{vdWaals}}$ & $E_{\mathbf{Coulomb}}$ represent the non-bonded van der Waals and Coulomb interactions. ReaxFF potentials have been developed for MoS_2 [28–30] and used to simulate processes including the crystallization of MoS_2 from amorphous precursors [31, 32], demonstrating the robustness of reactive MD simulations in investigating MoS_2 at an atomic scale.

Previous studies have attempted to address these challenges. For example, molecular dynamics (MD) simulations of SiO_2 thin films have been combined with Monte Carlo (MC) simulations to evaluate the kinetics of deposition on film properties [33]. This approach involved utilizing stepped deposition algorithms in conjunction with MC simulations to study sputtering, highlighting challenges related to high energetic bombardment, slow thermal relaxation, and system size limitations. With advancements in computational

techniques, equilibration can now be achieved in classical MD simulations by modeling atom deposition as a continuous flux of material traveling in the direction of the film [34].

To simulate sputtering deposition using MD, methods have been developed to model the process as a constant flux of atoms introduced randomly into the simulation box, with depositing atoms traveling toward the substrate at a defined velocity [33]. This strategy has proven successful in modeling the deposition of various materials, including silicon dioxide [35–37] and gold clusters [34].

Despite the progress made in developing classical MD sputtering deposition simulations for single component systems and SiO_2 systems, there is still a need to expand these simulation methods to sputtered MoS_2 thin films. Sputtered thin film MD simulations are critical to understand the effect of sputtering deposition on the microstructure and physical properties of MoS_2.

1.5 Surface Functionalization for On-Surface Mechanochemistry

Modification of silica surfaces with organic molecules is important for the development of medical, electronic, and pharmaceutical applications. Chemical bonds that form between a silica substrate and organic molecules modify the chemical and physical properties of the surface [38]. This opens the possibility to control or tailor properties such as friction [39], biocompatibility [40], and polarity [41] to a specific application. Examples include functionalization of atomic force microscope tips to improve their useful life [42], design of biocompatible amorphous silica [43] in drug delivery systems and implant applications [44] to treat osteoporotic fractures [45] and bone tumours or infections [46], development of sensors for detecting biological analytes [47], and creation of stimuli-responsive surfaces [48].

Many different organic molecules have been immobilized on silica through the formation of new covalent bonds with the surface [49]. Among these, aromatic hydrocarbons (AH) have been used in solution-based and mechanochemically driven perycyclic reactions [50] and proposed for applications in organic electronic devices [51]. AH are composed of aromatic carbon rings, with those in the acene group made up of linearly bonded rings. In solution-based chemistry, functionalizing silica with AHs is possible at room

temperature [49]. However, to further the development of AH silica functionalization as a predictable method to control surface properties, the mechanisms underlying chemical bond formation between the AH molecules and silica surface must be understood.

Importantly, chemical bonding affects the density of organic molecules on the surface which, in turn, determines the properties of the functionalized surface [52]. Observations of the change in contact angle of aromatic-modified substrates suggested surface density is affected by the orientation and size of the deposited molecules [53]. Studies of the surface properties of heterogenous polycyclic AH clusters [54] in soot showed that the surface densities of carbon atoms in solid-like configurations was affected by the structure of the surface-bound molecules, with smaller molecules, such as pyrene, contributing significantly to the surface density. Further, previous experiments showed that the adsorption of organic molecules with different functional groups on silica can be favored by molecular flexibility and good steric access of the adsorption active groups to the silica surface. [55].

Surface density can be estimated based on the geometry of a given molecule or measured using a quartz crystal microbalance (QCM) [56, 57]. Specific to the QCM method, by estimating the monolayer mass of the deposited molecules is possible to measure surface density. However, this method does not provide insight into the underlying chemical and physical processes and, particularly, the effect of the structure of the deposited molecules.

Among different use cases for surface immobilized molecules, in the field of mechanically driven chemistry, the study of Diels-Alder reactions has provide an interesting engine to uncover the effect of force on the bond formation. Diels-Alder reactions involve the use of two reactants (e.g., Diene and Dienophile) to create a single product via cycloaddition. These reactions have been well studied [58] thermochemically. However, Diels-Alder reactions offer an interesting engine to study mechanically driven reactions since they can be forward or backward driven without the need for catalytics or added reagents. Mechanochemically constrained Diels-Alder reactions have been evaluated to explore the role of mechanical energy on reaction rates [59] and its connection to thermally derived solution reactions.

Diels-Alder reactions can be found in different industrial applications and are primarily facilitating a process in which reversible covalent bonds are needed. An example of a Diels-Alder reaction in action is the development of vitamin b6. Here, for the preparation of pyrodioxide, a Diels-Alder reaction is incorporated into the process of synthesizing

pyridine-base actructure [60]. There is a large number of diene and dienophile chemistries capable of achieving Diels-Alder reactions of the [4+2] cycloaddition type. For the initial exploration of the variables that affect mechanochemical reactions, the system design requires selection of diene and dienophile chemistries that are 1) accessible both experimentally and computationally and 2) have high reactivity to speed throughput. Furthermore, when evaluating a dienophile, the reactivity is increased by electron-withdrawing substituent, weak $\pi-$bond and release of ring strain. Similarly, the reactivity of a diene increases by e-donating groups, planarity of the system and ability to adopt an s-cis conformation [61].

1.6 Modeling Surface Functionalization for Mechanochemistry

Computational methods can provide complementary information about molecule and surface interactions at the atomic level. Some studies have used *ab initio* methods [44, 62] for this purpose. However, the scaling of quantum calculations (i.e., $O(N^3_{electrons})$) makes such calculations unsuitable for modeling systems larger than a thousand atoms. In contrast, classical MD simulations based on empirical potentials are more efficient as they scale with the number of atoms in the system (i.e., $O(N_{atoms})$).

Like previously mentioned, the development of empirical potentials that model chemical reactions, such as ReaxFF [63], has made it possible to observe bond formation in a dynamic simulation. The ReaxFF potential has been shown to accurately describe the geometry, stability, and chemical bonding of conjugate, non-conjugate, and radical-containing compounds [64]. Relevant to our current investigation, ReaxFF simulations have been used to study the formation of alkysilane self-assembled monolayers on silica [65] and shear-activated oxidative chemisorption and oligomerization of cyclic hydrocarbons on amorphous silica [66, 67]. Simulations of the functionalization of crystalline silicon surfaces with alkyl radicals were able to accurately reproduce surface densities measured experimentally [68].

Among the different surface processes that can benefit from covalently adapted networks as a means of controlling chemical structures, an interests has sparked in the development of simulations for thermoreversible Diel-Alder reactions. Proponents of covalent

adapted network polymers developed simulations in which the welding and shape memory behaviour of Diels-Alder reactions was studied in a system where diene and dienophile terminations were observed to form bonds, therefore altering the flexibility and shape memory of the polymers [69]. This study showed the ability of MD simulations to capture bond formation in Diels-Alder reactions from Ab-initio designed force fields [70]. It is important to mention that a large portion of the body of work on Diels-Alder reactions has been focused on employing quantum mechanical calculations to parameterize force fields capable of describing atomic interactions as well as bond breaking and bond formation.

1.7 Dissertation Outline

Guided by experiments and advanced modeling techniques, this work focuses on the interplay between chemical and physical processes on surfaces and at interfaces. From tribological investigations in the Ni-MoS_2 system to dynamic processes in Ni-doped MoS_2 thin film formation, each facet of our exploration offers a view into the intricate world of surface science, paving the way for a more in-depth understanding of surface interactions and their implications in various applications.

Chapter 2 reports experimental work on characterizing the wear life of Ni-doped MoS_2 includes new methods and the results of tribological tests that elucidate the impact of Ni doping on the wear resistance and durability of MoS_2 films. This investigation provides an understanding of how Ni concentration influences the microstructure and performance of these films under tribological conditions.

Next, in Chapter 3, we evaluate a newly created ReaxFF potential to simulate Mo/S/Ni interactions. This includes the validation of the force field, followed by simulations of sputtering deposition processes for both Ni-doped and undoped MoS_2 thin films. The chapter culminates with shearing simulations, offering insights into the origins of Ni-doping's effects on tribological properties and the mechanisms behind these enhancements.

Shifting focus, the research reported in Chapter 4 explores the functionalization of amorphous silica surfaces with aromatic hydrocarbons. Simulations of the condensation reactions between silica and silanols with different numbers of aromatic rings at various temperatures are discussed. The impact of molecular structure on covalent functionaliza-

tion and surface density is analyzed, revealing correlations between surface density and the local conformational ordering of the silanols. Additionally, these functionalized surfaces are used in mechanically driven deformation studies, demonstrating their potential applications.

Lastly, the concluding Chapter 5 synthesizes the findings from the previous chapters, emphasizing the implications of this research for the development of advanced materials in tribological and mechanochemical applications. It outlines potential future directions for expanding this work, including further exploration of surface interactions and the development of new materials with tailored properties.

Chapter 2

Ni-doped MoS_2 Dry Film Lubricant Life

2.1 Introduction

Dry film lubricants (DFL) or solid lubricant coatings are preferred over liquid lubricants when operating conditions are extreme, e.g., very high or low temperature, vacuum or corrosive environments, or to prevent contamination of sensitive equipment [9–11]. Such conditions are present in various applications, but the prototypical example is space, where mechanical components must function in extreme environments, including cryogenic temperature and vacuum. Liquid lubricants in space applications suffer from many issues, including volatility, condensation, degradation due to radiation and increase in viscosity at low temperatures [71, 72], resulting in reduced operating life, which is especially important for long duration missions. The alternative is DFLs, which are non-volatile and stable in extreme conditions. Perhaps the most widely used DFL for space applications is molybdenum disulfide (MoS_2). MoS_2 has a long history as a lubricant [8] and is currently used both in space and terrestrial applications as an additive in greases and lubricating oils, and as a DFL [3]. The lubricity of MoS_2 is provided by its crystal structure where stacked layers of MoS_2 basal planes (002) are held together by weak inter-planar van der Waals attraction which is easily overcome when the layers experience shear [73].

There are various techniques of fabricating MoS_2 dry films, including burnishing, sputtering, resin bonding and impingement. However, sputtered MoS_2 coatings are preferred for space applications [9] due to their tribologically superior performance in the absence of

oxygen and humidity [74], good adhesion to substrates [75, 76] and absence of any binding agent that can outgas in vacuum conditions [77]. In a lab environment, the vacuum of space is often approximated by testing in dry nitrogen [12, 78–84]. Dry nitrogen simulates space vacuum conditions that are devoid of oxygen, water vapor and other elements that might affect the tribo-chemical processes occurring at the sliding interface [85]. Sputtered MoS_2 films exhibit excellent tribological performance in dry nitrogen with very low coefficient of friction (CoF) [86] and long wear life [12].

Despite the outstanding properties of sputtered MoS_2 coatings in environmental conditions devoid of oxygen and humidity, its tribological performance degrades significantly in ambient conditions [83, 87–92]. This degradation is often attributed to oxidation resulting in MoO_3 and MoO_2 byproducts which impede the smooth sliding of MoS_2 basal planes. However, the topic is still a subject of debate and other mechanisms have been proposed, including water-restricted-growth of shear-induced highly ordered tribofilms [83, 93] and viscous friction due to water molecules between basal planes [94, 95]. Further, it was shown that water and oxygen in the atmosphere affected friction differently [79]. At room temperature, atmospheric oxygen had very little impact due to a low rate of oxidation, whereas physisorption and diffusion of water molecules increased friction. However, the opposite was observed at higher temperatures (>100 °C) where the thermal energy-driven oxidation rate exceeded the wear-driven surface oxide depletion rate, resulting in a net increase in oxidation byproducts and higher friction, whereas water molecules desorbed readily and had little role to play [79].

The microstructure of sputtered MoS_2 is understood to play a significant role in its tribological behavior as well as its resistance to environmental conditions. Sputtered MoS_2 is known to have two possible morphologies, referred to as Types I and II, depending on the sputtering technique employed [96]. Type II consists of basal planes oriented parallel to the substrate resulting in dense packing and a low fraction of exposed edge sites. Type I morphology consists of basal planes oriented perpendicular to the substrate surface resulting in high porosity and exposed reactive edge sites. This Type I growth morphology is believed to have three distinct zones: starting from the substrate, there is a ridge structure, followed by a dense equiaxed zone, and finally a region of vertically oriented crystallites or columnar structures [97]. Most commercially produced MoS_2 DFLs are expected to exhibit Type I morphology due to the Direct Current (DC) sputtering

technique used to produce them.

Many previous studies have characterized the friction and wear performance of Type I MoS_2. The Type I microstructure causes an oxidation-driven friction increase, beginning during the run-in period when the columnar crystallites are oriented perpendicular to the substrate, before being forced to reorient in the direction of sliding, trapping the oxidation byproducts between the crystallites and impeding shear [97, 98]. The friction after run-in depends on the rate of thermally driven formation of surface oxides and the rate of depletion of these oxides due to wear from the contact zone [79]. The wear behavior of Type I sputtered MoS_2 coating was studied by Spalvins [99] who showed that, at the onset of sliding, the vertical MoS_2 lamellae are first reoriented in the sliding direction and then later fracture at the base where they are attached to the equiaxed zone. Another study showed that basal plane reorientation occurs early in the sliding process, within 5% of the total wear life of the coating [77]. Based on this, it was proposed that the detached lamellae were depleted from the contact zone and subsequently did not contribute to the operational life of the coating. Lubrication after that point was therefore proposed to be provided by a thin ($\sim$200 nm) lubricating film remaining on substrate after the lamellae detached [99].

Co-depositing or doping certain metals with MoS_2 is known to affect the coating microstructure and can alleviate the detrimental effects of humidity and oxygen on the tribological behavior of sputtered coatings. Dopants are believed to improve the tribological properties of sputtered MoS_2 films through different mechanisms, including increased oxidation resistance [12–14] and increased hardness, [15–21] depending on the dopant material used. In an early study, Stupp [24] evaluated multiple transition metal dopants and found Cr, Co, Ni and Ta to be the best overall performers in terms of friction, wear life, ease of co-deposition and aging-related degradation.

Particularly for space applications, Ni is a preferred dopant [22] due to its ability to mitigate the increase of friction at low temperatures [23] and its low cost and availability [24]. In one study, [12] higher concentrations of Ni dopant (up to 20% by weight) were investigated and it was found that, above 11%, the coating becomes brittle and fails prematurely. For maximum coating life and stable friction, 5-7% Ni was recommended [24]. Co-depositing MoS_2 with Ni has been found to affect the morphology of the film as well. Specifically, pure MoS_2 and MoS_2 with 3% Ni showed Type I morphology, whereas doping

with 9% or more Ni resulted in a "Zone T" microstructure which has a non-porous fibrous interior and flat tops [100]. However, how these changes in morphology due to Ni doping affect coating life is not known.

In summary, sputtered MoS_2 DFLs are preferred for space applications due to their excellent tribological performance in vacuum conditions devoid of oxygen and humidity. Sputtering results in MoS_2 microstructures that are believed to provide long life through processes that occur during run-in. Also, MoS_2 DFL performance, particularly friction at low temperatures, has been shown to improve with Ni doping. Although this improvement is attributed to the microstructure, the effect of Ni dopant on the morphological changes that occur during run-in is not understood. To address this, in the present study, we characterized the friction and wear behavior of sputtered doped and undoped MoS_2 films at different pressure and speed conditions. Long tests were run to determine coating life, as characterized by a drastic friction increase reflecting complete coating failure. Then, short tests were run to characterize and understand the run-in period during which it has been proposed that microstructural evolution occurs that plays a critical role in determining coating life. Results were analyzed in terms of both coating thickness, which is often assumed to correspond to life, and friction, reflecting actual useful life. Finally, findings were interpreted by analysis using microstructural and material characterization tools, including scanning electron microscopy (SEM) and energy dispersive spectroscopy (EDS).

2.2 Methods

Two coatings were investigated in this study: undoped MoS_2 and $\approx 7\%$ wt Ni-doped MoS_2. Both types of coatings were fabricated via DC sputter deposition with electron beam assist. Stainless steel (440C) disks of 0.25" thickness, hardness 45-50 HRC or 58-62 HRC with average surface roughness of 80 nm were used as substrates. The coating thickness varied slightly from disk to disk, but was in the range of 0.8 to 2.0 μm for all disks. A burnishing process was applied to the coated disks to obtain a smooth reflective surface finish. This involved sliding a wool-like material against the sputtered disks until coated surface has a uniform appearance and there is no more loose debris coming off the surface onto the wool.

Tribological testing to measure friction and wear was performed using an Rtec Instruments tribometer and white light interferometer. Unidirectional sliding tests using a ball-on-disk set-up as described by ASTM G-99 standard were performed to measure CoF. 440C stainless steel balls of 3/8" diameter with Rockwell C60 hardness were used as the counterbody. The radius of the circular sliding path on the disks was between 15 and 30 mm All test were carried out at room temperature and ambient air conditions with relative humidity ranging between 30–50%.

Table 2.1 shows the load and speeds used in the testing and the calculated maximum Hertz contact pressures. Note that the sliding speed was also varied to simulate the inverse stress (analogous to torque) and speed relationship typical in a gear-driven system. Two types of sliding tests were performed in this work, end-of-life and run-in. End-of-life tests were used to determine the wear life in terms of number of revolutions/cycles to failure. This test involved sliding on the coated disk until the CoF increased above ≈ 0.4, became characteristically noisy and did not drop back to lower values. Run-in tests were short duration sliding tests (between 5 and 250 cycles) used to study the evolution of wear and wear mechanisms. Only 300 MPa and 1100 MPa contact pressures were studied for run-in. Another distinction between the end-of-life and run-in tests is that, in the former, the disk was already rotating before the ball was pressed against it whereas in the latter, the disk was rotated after loading. Three repeat end-of-life tests and four repeat run-in tests were performed per case.

Normal Load (N)	Contact Pressure (MPa)	Sliding Speed (m/s)
0.27	300	1
2.5	500	0.77
5.1	800	0.44
13.3	1100	0.1

Table 2.1: Experimental parameters used in the ball-on-disk tests. High pressures are matched with low speed, and vice versa, to mimic the operating conditions of a gearing system.

3D surface images of the wear tracks were obtained using the white light interferometer. The interferometer was calibrated to be within 1% of reference values. Wear depth was measured from 2D profiles taken at different positions on the wear track using the image

processing software Gwyddion. The mean wear depth at four angular positions on each wear track was calculated and reported with error bars representing the standard deviation from the mean. Energy Dispersive Spectroscopy (EDS) using EDAX Genesis spectrometer attached to a FEI Quanta 200 Environmental scanning electron microscope (SEM) was used to obtain elemental composition in wear tracks. The microstructure of the coating before and after sliding was characterized using a Zeiss Gemini 500 SEM.

2.3 Results and Discussion

The microstructures of undoped and Ni-doped MoS_2 coating surfaces were characterized before tribological testing. The burnishing process applied after sputtering flattened the tops of the coatings, so images were taken at scratches on the burnished layer to reveal the microstructure of the material. The SEM micrographs in Figure 2.1 show that the undoped and Ni-doped coatings have similar microstructures, with highly columnar crystallites consistent with Type I coatings. The microstructures shown here are representative of images taken on multiple samples imaged at several different locations on the surface.

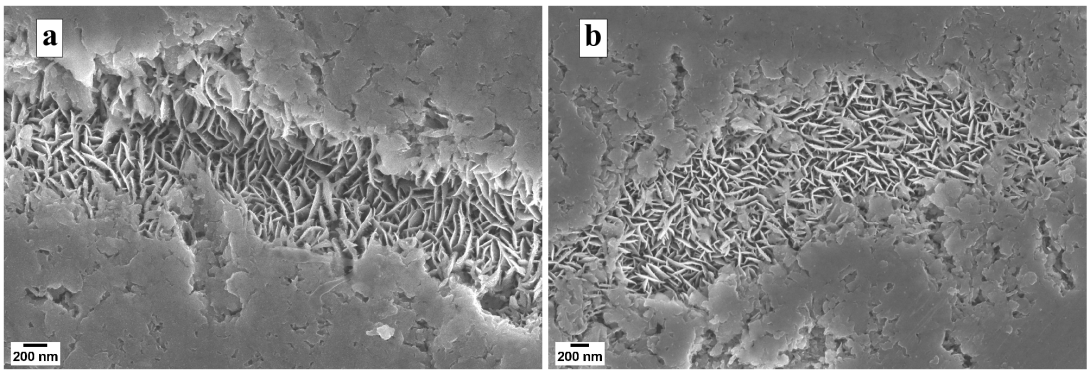


Figure 2.1: SEM micrographs of (a) undoped and (b) Ni-doped MoS_2 coating morphologies showing columnar structures consistent with Type I coatings and flat tops resulting from burnishing.

The performance of the undoped and doped MoS_2 coatings was measured at four different pressure/speed conditions. In the end-of-life tests, the CoF during sliding was tracked until the coating failed completely. Representative traces of the CoF as a function of number of cycles of rotation of the disk for undoped and Ni-doped coatings are shown

in Figure 2.2. For these cases, the number of cycles until failure, i.e. wear life, is greater for the lower contact pressure / higher speed conditions. Also, the results indicate that Ni-doped coatings have longer life than the undoped coatings and that difference appears to be most significant at the lower contact pressures.

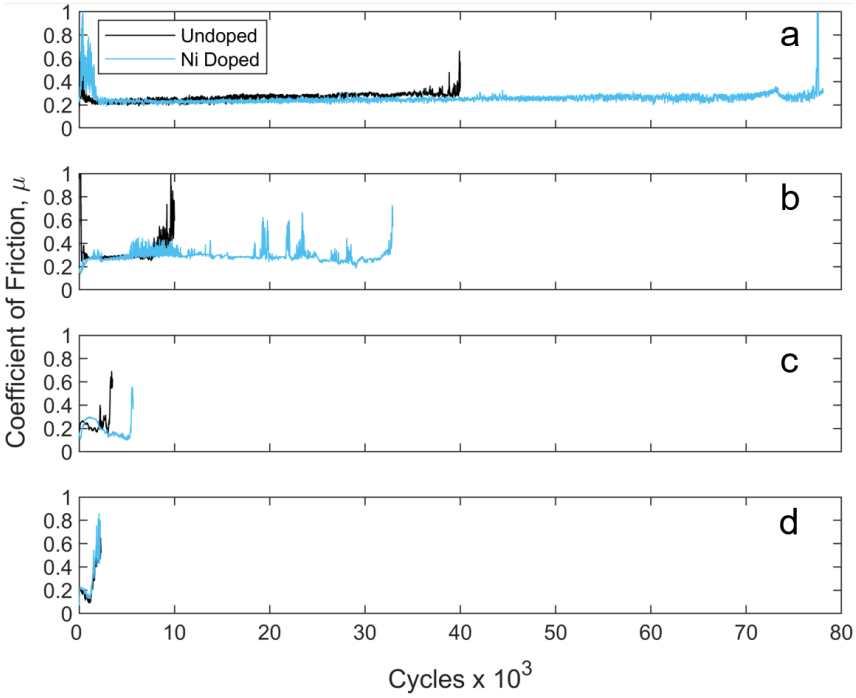


Figure 2.2: Representative CoF traces at (a) 300 MPa and 1 m/s (b) 500 MPa and 0.77 m/s (c) 800 MPa and 0.44 m/s, and (d) 1100 MPa at 0.1 m/s for undoped and Ni-doped MoS_2 coatings run until coating failure.

Coating failure was identified as the CoF exceeding and remaining above ≈ 0.4. We confirmed that the coating life identified using this criterion was reasonable by analysis of the elemental composition of unworn, partially worn and fully worn regions on the surfaces using EDS. The results for an undoped coating are shown in Figure 2.3. In this case there are two wear tracks shown: the track on the left corresponds to midway through a test (prior to failure) and the one on the right was taken at the end of a test (after failure). It is clear from the compositional maps of Molybdenum (Mo) and Sulfur (S) that the MoS_2 coating is fully worn on the right wear track with negligible Mo and S signal, while both Mo and S are observed on the left wear track obtained prior to failure. This is confirmed by observation of prominent Iron (Fe) and Chromium (Cr) signals from the steel substrate on the right wear track, after failure.

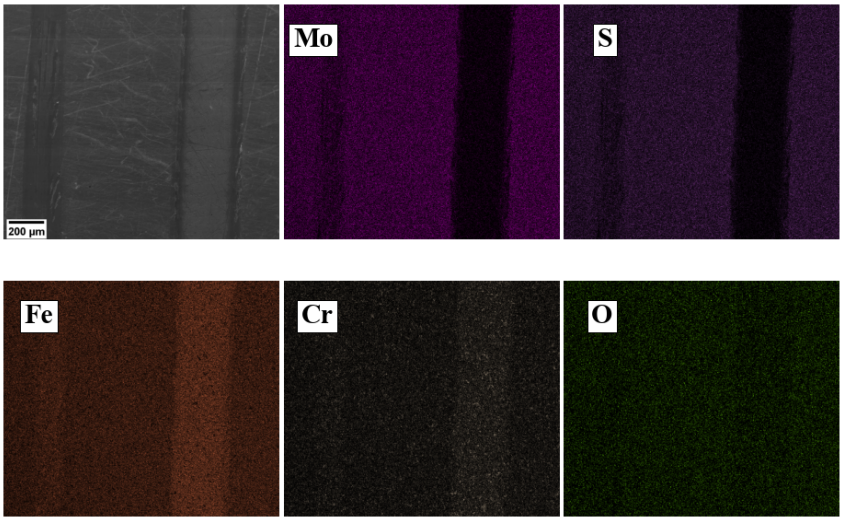


Figure 2.3: EDS compositional maps showing partially worn (left wear track), unworn (center region) and fully worn (right wear track) regions of undoped MoS_2 coating. The partial and fully worn tracks were generated in sliding tests at 300 MPa contact pressure after 18,000 and 80,000 cycles, respectively.

A similar EDS compositional map of unworn and full worn (after coating failure) regions of Ni-doped coating is shown in Figure 2.4. As expected, both fully worn tracks show negligible Mo and S signals, indicating the coating has been removed and prominent Fe and Cr signals from the steel substrate.

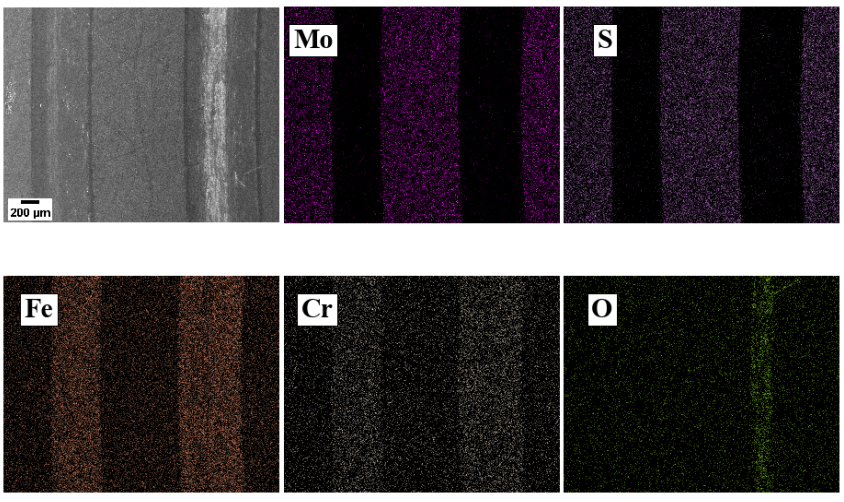


Figure 2.4: EDS compositional maps showing two fully worn wear tracks and unworn regions on a Ni-doped MoS_2 coating. The left and right tracks were generated in sliding tests at 500 MPa contact pressure after 34,000 and 43,000 cycles, respectively.

Wear life was measured from long duration tests at each pressure/speed condition for undoped and Ni-doped MoS_2 coatings. The results are shown in Figure 2.5, where the symbols represent the mean of three tests and the error bars reflect the standard deviation. The results indicate that Ni dopant improves the life of the MoS_2 coating at the lower contact pressures of 300 and 500 MPa, but the difference between doped and undoped coating life is not statistically significant at the higher contact pressures of at 800 and 1100 MPa. Also, the life of the Ni-doped coatings exhibits higher variability than the undoped coatings, particularly at the lower pressures. This may be attributed to non-uniformity in the distribution of Ni dopant in the coating on individual samples or from sample-to-sample, or greater variability in coating thickness for the doped samples.

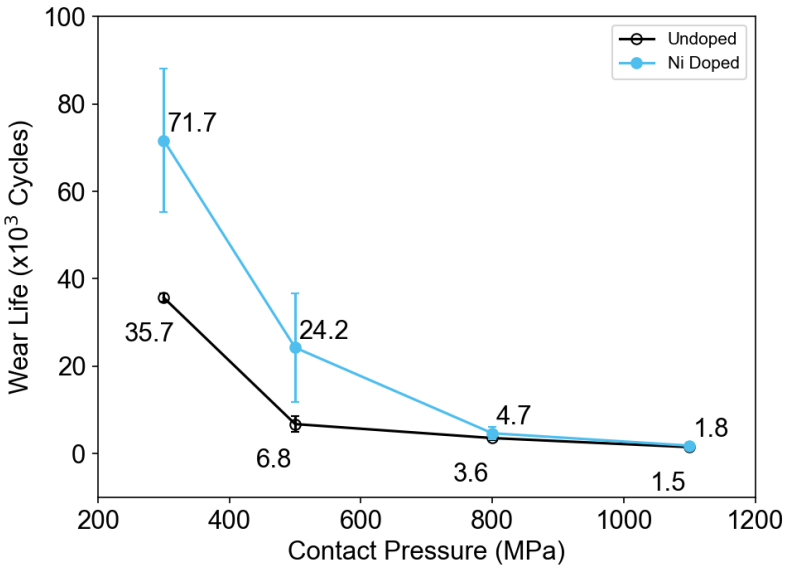


Figure 2.5: Wear life of undoped and Ni-doped MoS_2 at different contact pressure / sliding speed conditions. The results are plotted against pressure on the abscissa, but the speed is also different for each case. Ni dopant improves wear life compared to the undoped samples at low pressures.

Short duration tests were performed to study coating wear during run-in as a means of understanding wear mechanisms and how they are affected by the Ni dopant. For this, the rotating disk was stopped at different intervals of sliding and the 3D surface topography of the wear track at a fixed angular position was measured using an interferometer. Then, the sliding was restarted from the location at which it was stopped. This technique enabled

tracking of the evolution of the coatings during the wear process. In these tests, the coatings did not fail, as determined by the friction coefficient criterion used in the end-of-life tests. Representative cross-sections of the wear track obtained from the interferometer images at different number of cycles during run-in at the highest and lowest pressure are shown in Figure 2.6. These results indicate that wear depth generally increases with number of cycles and is greater for the higher pressure.

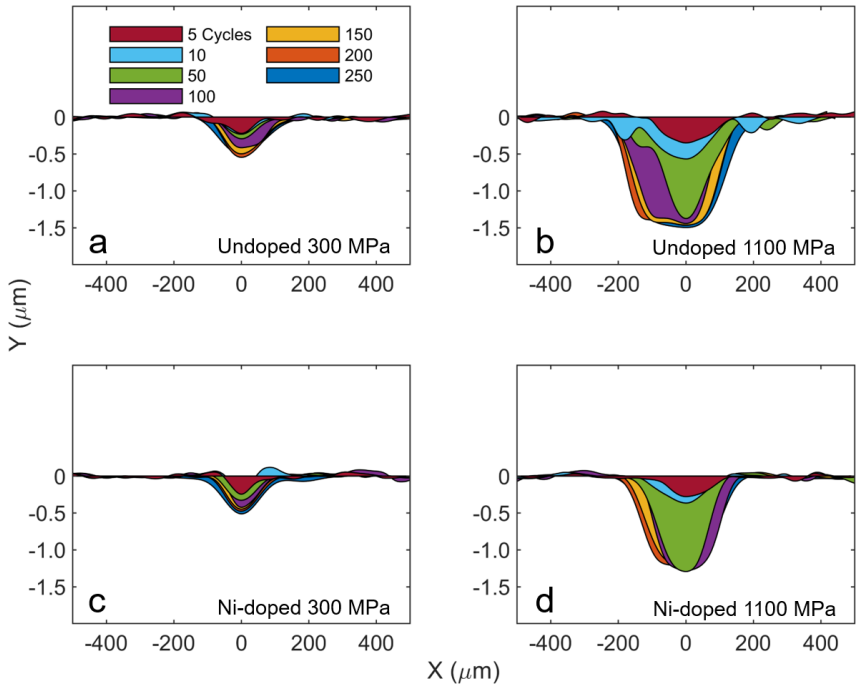


Figure 2.6: Wear profiles for (a) undoped MoS_2 at 300 MPa and 1 m/s, (b) undoped MoS_2 at 1100 MPa and 0.1 m/s, (c) Ni-doped MoS_2 at 300 MPa and 1 m/s, and (d) Ni-doped MoS_2 at 1100 MPa and 0.1 m/s showing the evolution of the wear tracks during the run-in tests.

The wear depth was measured as the maximum depth of wear profiles such as those in Figure 2.6 from four tests on two different samples. The wear depth was then normalized by the coating thickness for each disk such that a normalized wear depth of 1 indicates that the coating has been completely removed. The average normalized wear depth is plotted as a function of number of cycles in Figure 2.7, where error bars represent the standard deviation. As expected, in all cases, the wear depth increases with number of cycles and is larger at the higher pressure. Also, notably, at either pressure, the wear tracks on the Ni-doped MoS_2 are shallower than those on the undoped MoS_2. This agrees

qualitatively with the longer life of the Ni-doped coatings observed in the end-of-life tests at low pressure.

Figure 2.7 also reveals different run-in behavior at low and high pressures. Specifically, the wear rate, i.e. rate of change of depth with cycles, is nearly constant throughout run-in at the low contact pressure. In contrast, at high pressure, the wear rate is initially very rapid but then decreases after about 100-150 cycles to a value similar to that observed at the low pressure. For the undoped coating at 1100 MPa, the normalized wear depth is unity (depth = coating thickness) after only 180 cycles. For the other cases, we used the rate of decrease of normalized wear depth with cycles after 150 cycles to estimate the number of cycles at which the normalized wear depth would reach unity. It was found that the wear depth would be equal to the coating thickness after 940±374 cycles for the undoped coating at low pressure and 1226±787 and 725±274 cycles for the Ni-doped coating at low and high pressure, respectively. This approximation assumes a linear wear rate, but we confirmed that the trend remained linear with additional tests to 1000 cycles on undoped coatings at high stress. Further, even if the rate becomes slightly sub-linear, these results predict that the wear depth would still exceed the coating thickness after hundreds of cycles, whereas the wear life was on the order of tens of thousands of cycles in Figure 2.5. This means that, for most of the life of the coating, very little of the "bulk" material is present in the wear track.

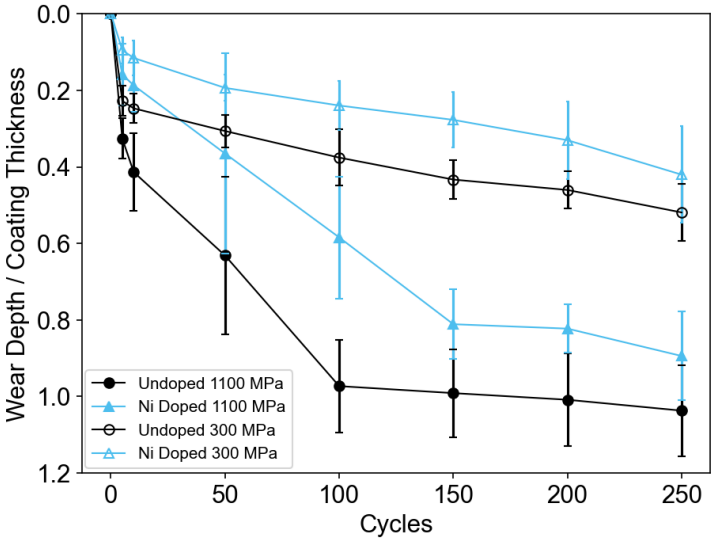


Figure 2.7: Wear depth as a function of cycle during run-in tests at 300 and 1100 MPa contact pressures on undoped and Ni-doped MoS_2. Wear tracks are shallower (less wear) on the Ni-doped sample at both pressures.

The implication of the above analysis is that the sliding contact is lubricated by local MoS_2 flakes or debris that form as the coating is worn. This was supported by the observation of MoS_2 on the ball observed via optical microscopy (not shown) after tens of thousands of cycles. We also characterized the coatings using SEM at the initial stages of run-in. Representative SEM micrographs of the wear tracks on the undoped and Ni-doped MoS_2 films after 10 cycles at 1100 MPa and 0.1 m/s are shown in Figure 2.8. On both the doped and undoped samples, we observe significant wear, even after only 10 cycles. However, the wear mechanism appears to differ between doped and undoped. Specifically, while both coatings exhibit cracking, there is also delamination in the case of the Ni-doped sample (Figure 2.8b) that is not observed on the undoped sample (Figure 2.8a). Based on the microstructure of these Type I coatings, it is presumed that the columnar zone is cracking and/or delaminating. This difference in failure mode has also been reported in a previous study where sputtered MoS_2 with 9% Ni exhibited more delamination in indentation tests than pure or low Ni concentration MoS_2 [101].

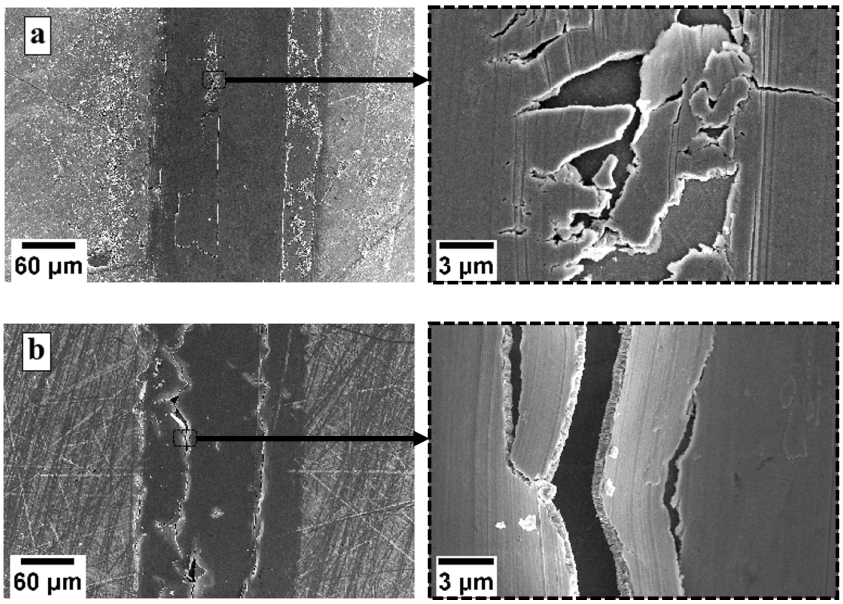


Figure 2.8: SEM micrographs of (a) undoped and (b) doped MoS_2 coatings after 10 cycles at 1100 MPa and 0.1 m/s. The images on the right show close-up views of the partially worn material. These images show representative features where the undoped coatings exhibit cracking while the doped coatings exhibit cracking and delamination.

It has been suggested that the columnar zone of Type I MoS_2 sits on a lower layer of material, called the equiaxed zone [97]. SEM images of the regions between the cracks on the doped and undoped coatings after 10 cycles are shown in Figure 2.9. These examples, that are representative of images taken at various locations on the worn surfaces, exhibit clear differences between the coatings. Notably, the material under the cracked or delaminated columnar zone for the undoped coating is smooth while that for the Ni-doped coating is rough. This may be attributable to differences in the microstructure of the doped coating that arise during sputtering. Alternatively, it could be related to the delamination that was observed only for Ni-doped coatings and may have occurred through breaking of columnar structure, leaving partial columns on the surface.

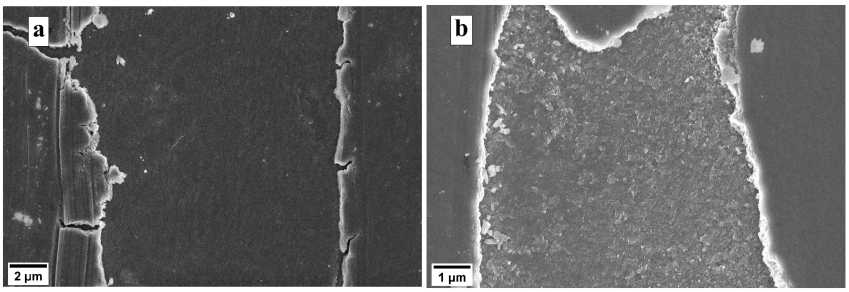


Figure 2.9: SEM micrographs of the regions between the cracked or delaminated columnar zone for (a) undoped and (b) Ni-doped MoS_2 coating after 10 cycles at 1100 MPa and 0.1 m/s. The material underneath the failed columnar zone is distinctly rougher for the Ni-doped coating.

The fact that the wear depth appeared to exceed the coating thickness after very few cycles (compared to the wear life) suggested the contact was lubricated by localized MoS_2 flakes or debris. Based on the images in Figure 2.8 these flakes could have formed through cracking or delamination of the columnar zone. Representative images of some of flakes from tests run to 10 or 250 cycles are shown in Figure 2.10. First, in all cases, the thickness of the flakes (as approximated from these images) is on the order of a few hundred nanometers. This is less than the expected coating thickness, suggesting that the columnar zone gets denser due to the contact pressure. Also, the flakes at 10 cycles (Figures 2.10a and b) appear to retain more of the original columnar structure (Figure 2.1) than the flakes imaged at 250 cycles (Figures 2.10c and 2.10d). This difference may be attributable to crystalline reorientation suggested in previous studies [77, 97, 98]. However, there is no obvious difference between the cross-sections of the flakes from the undoped (Figure 2.10c) and Ni-doped (Figure 2.10d) coatings.

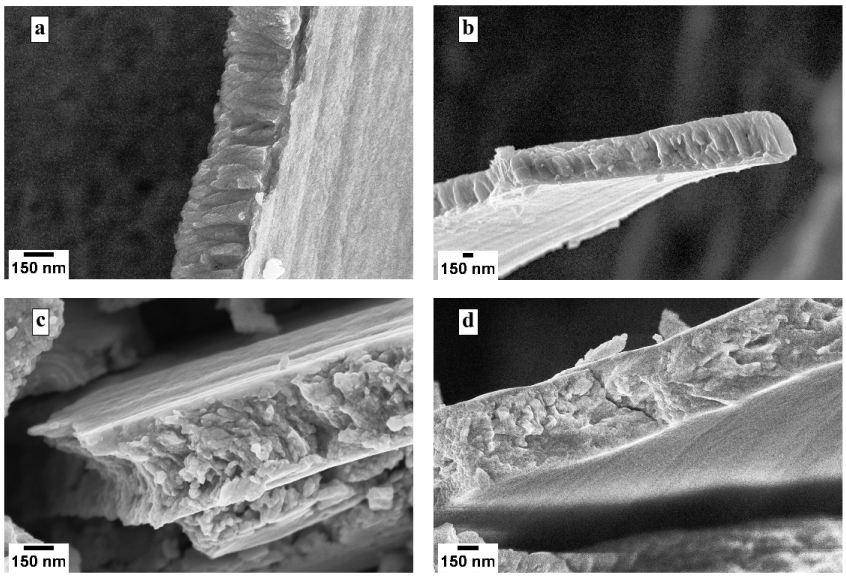


Figure 2.10: SEM micrographs of dense flakes of MoS_2 within or near the wear track from run-in tests of (a and b) Ni-doped coatings after 10 cycles, (c) an undoped coating after 250 cycles, and (d) a Ni-doped coating after 250 cycles. All images from tests at 1100 MPa and 0.1 m/s.

The SEM evidence supports the hypothesis that most of the life of the coating is provided by flakes of material. However, these flakes must be supplied continuously throughout the life of the coating. Since the depth of the wear track exceeds the coating thickness at the high pressure, the flakes cannot be coming from the bottom of the wear track. Rather, it is likely that they are replenished from the sides of the wear track, i.e. as the width of the worn region increases, additional cracking and/or delamination provides newly available lubricious material. We tested this hypothesis by measuring the wear track width (full width at half maximum) during the run-in tests. The results shown in Figure 2.11 indicate that wear width increases with cycles, but at a much slower rate than the wear depth in Figure 2.7. Note that, although the wear width appears to plateau after a few hundred cycles at 300 MPa, in fact the width continues to increase throughout the test (e.g. the widths of the wear tracks in the EDS images in Figure 2.3 are several times larger than the apparent plateau in Figure 2.11). Generally, the observation of increasing wear width is consistent with the hypothesis that worn material is gradually removed from the sides of the wear track to lubricate the contact.

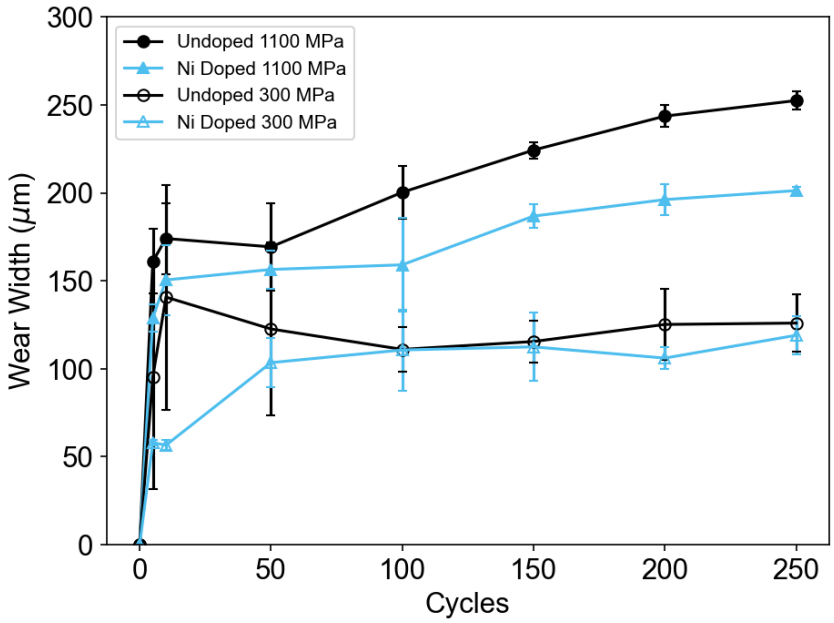


Figure 2.11: Wear width as a function of cycle during run-in tests at 300 and 1100 MPa contact pressures on undoped and Ni-doped MoS_2. Wear tracks widths are larger at the higher pressures. In all cases, the width increases gradually with sliding cycles.

All of the above suggests a mechanism by which MoS_2 coatings provide low friction and wear by generating flakes of lubricious material at the edges of the wear track. The remaining question is why Ni-doped coatings wear more slowly during run-in and have longer wear life at low pressures. One explanation is the Ni-doped coatings are harder, since increased hardness is one mechanism by which dopants have been proposed to improve the tribological performance of MoS_2 [12, 24]. However, the different failures modes observed in Figure 2.8 as well as the differences in the material underneath the cracked/delaminated columnar zone in Figure 2.9 suggest there may be another contributing factor. The observation that coating performance is enabled by flakes of worn material suggests that the Ni-doped coating generates more lubricious and/or longer-lasting flakes. Specifically, it is likely that delamination yields more and potentially larger and denser flakes of columnar material than cracking.

To investigate this hypothesis, we performed progressive load scratch testing following the ASTM C1624-05 standard. This test involves scratching the surface using a spheroconical diamond indenter of radius 200 μm at normal load progressively increased from 5 to 80 N at a sliding speed of 10 mm/min. The lateral force on the indenter was recorded

and plotted against time as shown in Figure 2.12(a). There is no abrupt change in the lateral force during any of these tests, indicating that either there was no 'damage event' due to coating failure or the coating failed at the onset of sliding. Also, the lateral force on the Ni-doped coating is slightly (although statistically significantly) lower than that on the undoped coating.

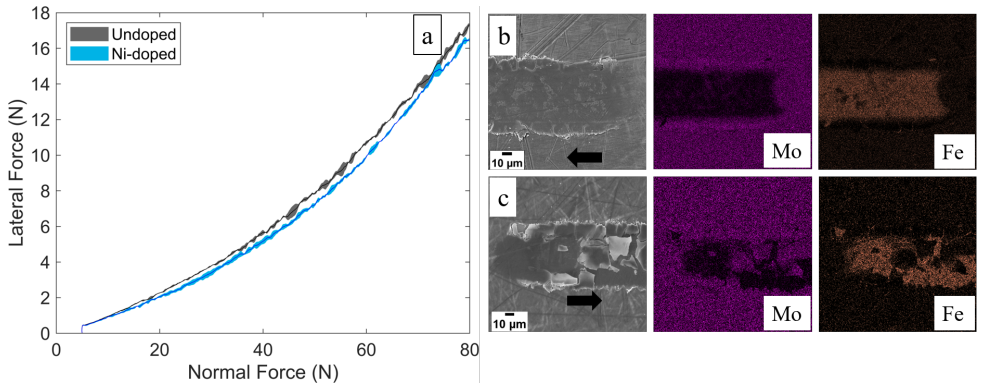


Figure 2.12: (a) Average lateral force during progressive load scratch tests on doped and undoped samples. Lines represent the average of three tests and the band represents standard deviation. SEM images and Mo/Fe signals from EDS taken at the start of the test on (b) undoped and (c) Ni-doped coatings.

This difference was investigated using SEM and EDS of the scratched region . Representative images taken from the beginning of the scratch (around 5 N load) are shown in Figure 2.12(b) and (c). From the SEM images, the difference in the wear modes of these coatings is apparent: the undoped coating is almost fully worn in the contact zone, whereas Ni-doped coating is still partly intact with some signs of delamination. This was confirmed by the elemental composition maps that show Mo remains in the scratched region only in the case of the Ni-doped coating; similarly, the Fe signal is much stronger for the undoped coating.

SEM images take later in the test at higher loads (about 62 N) are shown in Figure 2.13. These results confirm both the coatings are fully worn. In the middle of the wear track, both surfaces have semi-circular features oriented in the sliding direction that are the result of conformal accumulation of plastically-deformed substrate material. However, the two surfaces differ at the edge of the wear track where there is more spallation and delamination for the Ni-doped coating. This corroborates the hypothesis that the Ni-doped coating generates more material from the sides of the wear track.

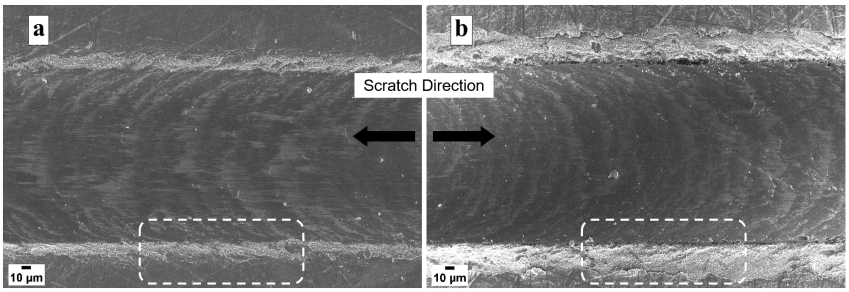


Figure 2.13: SEM micrographs of (a) undoped and (b) Ni-doped MoS_2 coatings during a representative progressive load scratch test (at approximately 62 N load). The doped and undoped coatings are distinctly different at the edges of the wear tracks (for example, the regions identified by the dashed lines).

The evidence presented strongly suggests that the Ni-doped MoS_2 coatings have longer wear life because of their ability to generate more lubricious material from the sides of wear track. This mechanism is likely complemented by increased hardness, as observed for doped MoS_2 coatings in previous studies. The complete proposed mechanism is illustrated in Figure 2.14. The columnar zone is compressed in the first few cycles and then begins cracking (undoped) or delaminating (Ni-doped), leading to the formation of lubricious flakes. Although the coating is worn through in the center of the wear track, the track width gradually increases with cycles, resupplying lubricating flakes to the contact over the remaining life of the coating.

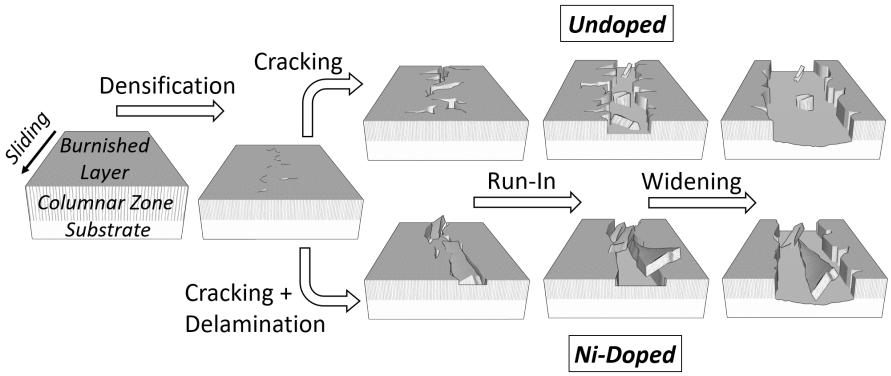


Figure 2.14: Schematic illustration of the proposed wear process that occurs through densification followed by cracking and, for Ni-doped MoS_2, delamination. The flakes generated during the cracking and/or delamination process lubricate the contact subsequently as they are continuously supplied as the wear track widens and more flakes are made available to facilitate sliding.

2.4 Conclusions

In this study, the effect of Ni dopant on wear life and morphological evolution of sputtered MoS_2 coatings was investigated. Tribological experiments at different pressure and speed conditions were performed to measure and compare the wear life of Ni-doped and undoped MoS_2 coatings. The results showed that Ni dopant at $\approx 7\%$ by wt. concentration improved wear life of MoS_2 coatings significantly at low contact pressures. However, Ni-doped coatings exhibited higher variability in wear life than undoped coatings, possibly due to non-uniformity in Ni distribution or coating thickness in doped samples.

Similar tests were performed for short duration (5 to 250 cycles) at low and high pressure conditions to study the evolution of wear during run-in. This process was characterized in terms of wear depth, wear width and coating microstructure. At both low and high pressure conditions, the wear depth either exceeded or was expected to exceed (based on extrapolation of the wear rate) the coating thickness early in the run-in process, suggesting that very little of the "bulk" material was left in the wear track for most of the life of the coating. This result implied that the contact was being lubricated by detached MoS_2 debris or flakes, which was supported by SEM micrographs showing cracked and/or delaminated coating in the wear track after the first 10 cycles. The gradual increase of

wear width of the coating suggested that lubricious flakes of MoS_2 were supplied to the contact from the sides of the wear track as the width of the worn region increased.

SEM imaging suggested that the undoped and Ni-doped coatings exhibited different wear mechanisms, with the former wearing by cracking while the latter demonstrated cracking and delamination. Analysis of progressive load scratch tests confirmed that wear behavior differed between the doped and undoped coatings, particularly at the edges of the worn regions. The delamination exhibited by the Ni-doped coatings may explain its longer wear life since delamination yields more and possibly larger and denser flakes than those generated by cracking of undoped coatings.

More generally, the findings of this study illustrate that the wear life of MoS_2 coatings cannot be correlated to wear track depth, in contrast to the usual concept of wear for traditional engineering materials. Further, the results suggest a new mechanism by which dopants can extend MoS_2 dry film lubricant life, i.e. facilitating delamination, that might be leveraged to further understand and then improve the performance of these materials.

Chapter 3

Molecular Dynamics Simulations of Undoped and Ni-doped MoS_2 Dry Film Lubricants

3.1 Introduction

As mentioned in Chapter 1, transition metal dichalcogens (TMDs) are an emerging class of materials with distinctive physical, chemical, and electronic properties. TMDs are two-dimensional materials comprising lamellae of strongly covalent bonded transition metals (e.g., Cr, Mo, W) and chalcogens (e.g., S, Se, Te) atoms stacked and held together by weak van der Waals forces [3, 102]. Molybdenum disulfide (MoS_2) is the most prominent TMD and its abundance on earth and cost effective production methods help position MoS_2 as a promising material for many different applications. [103]. These applications include catalysis [26], electronics [104], and tribology [3, 77].

In tribology, MoS_2 is used as a dry film lubricant (DFL) where liquid lubrication is not ideal. A common example of this is aerospace/space machinery which must function in conditions ranging from extreme heat to cryogenic in the vacuum of space. In such environments, the viscosity of liquid lubricants either becomes too low or too high and outgassing is a concern [3]. These issues are overcome by MoS_2 DFLs that have proven effective in providing low friction and long life in harsh environments [83, 105]. However, the effectiveness of MoS_2 DFLs has been reported to be dependent on the method and

conditions of synthesis [106].

Methods for synthesizing MoS_2 vary based on the intended use and desired material properties. Techniques such as chemical vapor deposition, molecular beam epitaxy, and metal-organic chemical vapor deposition are favored for electronic applications where crystal quality is paramount [102, 104]. In contrast, sputtering deposition methods are employed for applications where crystal quality is secondary and an amorphous microstructure is acceptable. For tribological applications, sputtering deposition of MoS_2 is the most common method used [107].

The sputtering deposition process involves bombarding a target material with high-energy ions, causing atoms to condense on a substrate, forming a thin film [108]. Physical characterization of sputtered thin films has led to better understanding of growth morphology [21, 109], substrate effects [110], and correlations between process conditions and microstructure-dependent physical or electronic properties [27]. For example, a comparison of MoS_2 thin films deposited at room temperature and 670 K showed that the room temperature films had an amorphous smooth structure while the films deposited at 670 K were nano-crystalline with a grained surface morphology [27]. The microstructure of a sputter deposited MoS_2 directly affects its properties and performance as a DFL [16, 109]. Consequently, various methods have been proposed to enhance the final film structure, including laser annealing, vacuum heat treatment, and co-sputtering with other elements.

Co-sputtering MoS_2, also referred to as doping, has been shown to enhance MoS_2 DFL tribological properties in both vacuum and ambient conditions. Dopants can substitute the Mo or S atoms in the MoS_2 lamella or remain intercalated between layers [3]. The mechanisms by which dopants enhance the tribological properties of MoS_2 is a topic of active research. Increased density [12, 22, 111] and increased hardness [15–19, 21] are two widely cited mechanisms. However, the increase of hardness is not a universal. Some dopants reduce the hardness of the DFL and still improve its tribological properties by facilitating transfer film formation [13, 18, 112]. DFT studies of the effect of Ni dopants on the layer dissociation energy have provided some insight in the role of dopants in increasing inter-layer binding in doped MoS_2 in comparison to pristine MoS_2 and how the additional binding between layers can increase atomistic roughness as dopants intercalate between layers to help reduce the work of adhesion and contact area [113, 114] . Various dopants have previously been evaluated including titanium [115], gold [112],

and nickel [116]. Particularly, nickel (Ni) has been considered for doping MoS_2 due to its relative abundance, ionic radius similar to Mo, and electron configuration [117]. Ni-doped MoS_2 DFLs typically have Ni concentrations ranging from 2% to 15% by weight [107, 118]. It has been reported that the concentration of Ni can influence the wear resistance and electrical conductivity of the material [24, 116, 119, 120]. However, the effect of Ni concentration on structural variations in sputtered films and the resultant DFL performance is not fully understood.

This limited understanding is partially due to the challenges associated with using experimental methods to monitor film growth during sputtering or film evolution during use as a DFL. However, experiments can be complemented by computational methods such as molecular dynamics (MD) simulations to identify the atomistic origins of correlations between processing parameters and material properties. For MoS_2 films specifically, MD simulations have previously been instrumental in explaining the effects of parameters such as temperature [121], oxidation, and shear stress [6, 93, 105], on the mechanical properties and nano-structure of MoS_2. For processes that involve the formation and breaking of chemical bonds, ReaxFF potentials have been developed for MoS_2 [28–30]. These potentials have been used to simulate processes including the crystallization of MoS_2 from amorphous precursors [31, 32], demonstrating the robustness of reactive MD simulations in investigating MoS_2 at an atomic scale.

To simulate sputtering deposition, methods have been developed to model the process as a constant flux of atoms introduced randomly into the simulation box, with depositing atoms traveling toward the substrate at a defined velocity [33]. This simulation strategy has proven successful in modeling deposition of various materials, including silicon dioxide [35–37] and gold clusters [34]. The recent development of a new ReaxFF potential that includes parameters for interactions between Ni, Mo, and S enabled simulations of sputtering deposition of Ni-doped MoS_2 [30]. The results showed the formation of a thin, primarily amorphous film formed by sputtering [30]. However, no analysis of the Ni distribution in the material and its effect on the film nano-structure was performed. Similarly, the effects of Ni concentration on nano-structure and the tribological properties of the deposited material were not explored.

In this study, we evaluate the effect of Ni on DFL nanostructure and tribological properties using reactive MD simulations. The study included three parts. First, we modeled

deposition and annealing of MoS_2 to evaluate the ability of the Ni-MoS_2 force field to capture the crystallinity of the material. Second, we modeled deposition without annealing but with varying temperature and Ni concentration to investigate how processing variables influence the nano-structure. Lastly, we conducted simulations of sliding using the deposited films at different Ni concentrations to evaluate frictional behavior and the evolution of the material in response to shear.

3.2 Methods

3.2.1 Deposition and Annealing to Evaluate the Potential

To demonstrate the applicability of the newly developed ReaxFF force field [30] for Mo/S/Ni, the process of sputter deposition and annealing to grow Ni-doped MoS_2 films [122] was simulated.

Methods

The simulations were performed using LAMMPS in the NVT ensemble with the Langevin thermostat, a damping parameter of 10.0 fs, and a time step of 0.1 fs. The simulation box was $2.5 \times 2.4 \times 10.0$ nm in the x-, y-, and z-directions, respectively, with periodic boundary conditions in the x- and y-directions. The boundary condition in the z-direction was fixed to mimic deposition in this direction. The initial configuration was a substrate consisting of bilayer 2H-MoS_2, with the bottommost layer held fixed during the simulation.

Atoms were deposited from 7.0 nm above the substrate surface, and a reflective virtual wall (which reflects downward only) was placed parallel to the surface at a distance of 4.8 nm to ensure deposited atoms remain near the substrate. The deposition process followed a simulation protocol used previously for SiO_2 thin film formation. [33] While the timescales accessible in atomistic simulations are much shorter than in real experiments, this kind of simulation has been found to be useful in generating realistic atomistic structures. First, energy minimization was performed to obtain the relaxed atomic positions, followed by thermal equilibration for 50 ps at room temperature. Next, Mo, S, and Ni atoms were continuously deposited onto the MoS_2 substrate at a 1:2 Mo to S ratio with Ni atoms replacing Mo atoms at 7% by weight, expected to promote Ni substitution for

Mo. [116] The deposition rates for Mo and Ni were one atom every 40 fs with a deposition energy of 230 kcal/mol; for S atoms the deposition rate was one atoms every 20 fs with a deposition energy of 1.5 kcal/mol. Under typical experimental conditions, an inert gas such as argon is used to modulate the incident kinetics of the deposited Mo, S, and Ni radicals. Following previous simulations of Si-O deposition [123], a lower deposition energy was used to slow the sulfur atoms such that they act not only as radicals but as kinetic energy modulators, without the need to explicitly model argon. The total number of deposited S, Mo, and Ni atoms after 50 ps was 1000, 405, and 95, respectively. At the end of the deposition process, the system was equilibrated at 300 K for 50 ps.

The second stage was annealing the deposited Ni-doped MoS_2 film, following a simulation process similar to that used previously for the crystallization of un-doped MoS_2. [29] At this stage, the constraints on the lowermost atoms were removed and the simulation cell height was set to the height of the reflective wall at 4.8 nm with the boundary condition in the z-direction changed to periodic to model bulk material. The annealing process was carried out by heating the model at the end of the deposition stage to 5000 K over 50 ps at a ramping rate of 100 K/ps. The structure was equilibrated at high temperature for 50 ps. Then, the structure was cooled to 2000 K at a rate of 30 K/ps followed by equilibration for 300 ps to trigger nucleation. Finally, the model was cooled to 300 K over 170 ps (10 K/ps).

3.2.2 Sputtering Deposition at Different Temperatures and Ni Concentrations

Reactive MD simulations were performed using the ReaxFF potential with parameters developed for Ni-doped MoS_2 [30] with a time step of 0.25 fs. All simulations were run using LAMMPS, atom configurations were visualized with OVITO, and post-processing was done with custom Python scripts. Fig 3.1 shows representative snapshots at different stages of the simulation process including deposition, equilibration of the deposited material, followed by compression and shear to mimic a DFL in use.

Sputtering deposition simulations were performed using the NVE ensemble with the Berendsen thermostat [124] with a damping parameter of 10 fs. The simulation box was $8.2 \times 4.5 \times 10.0$ nm in the x-, y-, and z-directions, respectively, with periodic boundary conditions in the x- and y-directions. Atoms with vertical positions between 0 and 0.2 nm

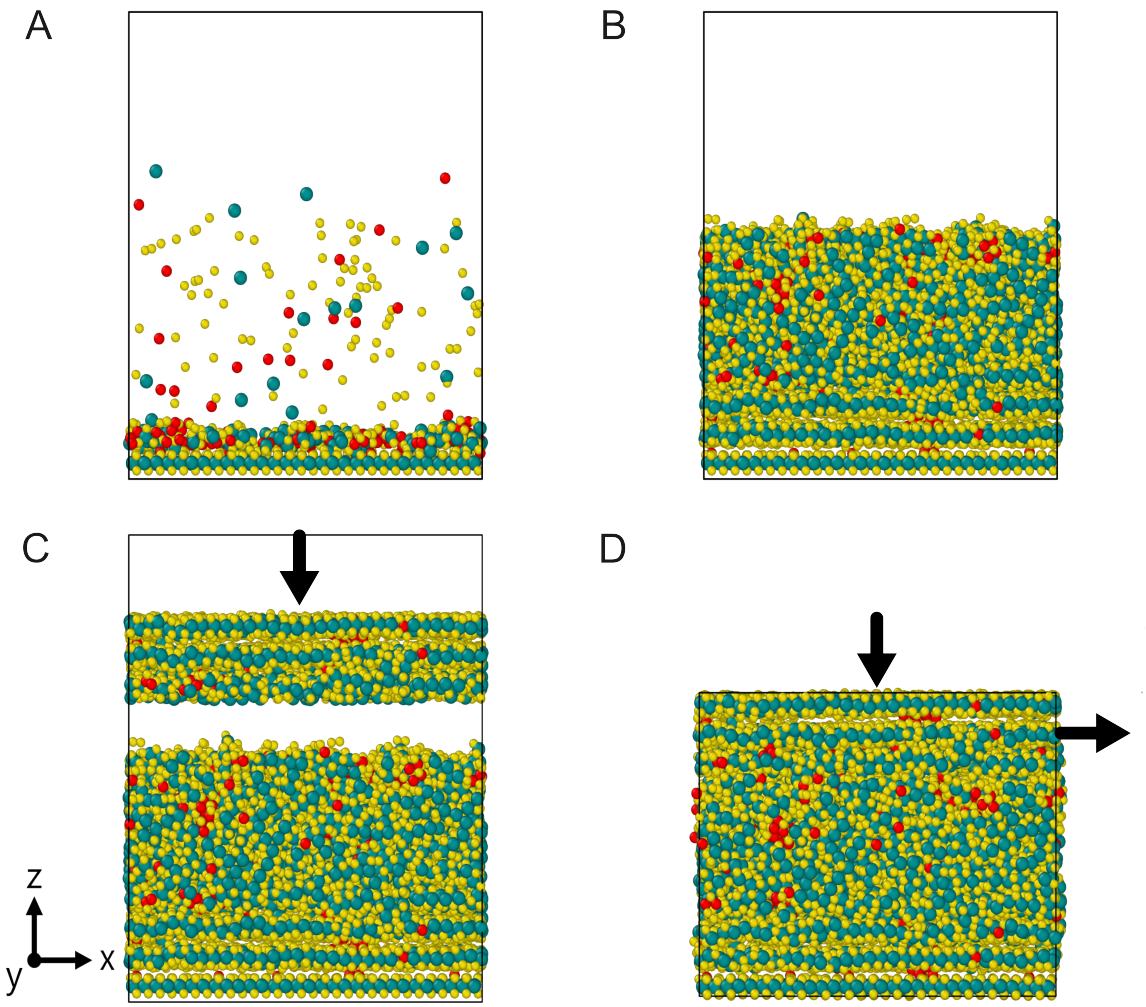


Figure 3.1: Snapshot representations of the simulations steps: (A) sputtering deposition, (B) equilibration, (C) compression, and (D) shearing of the 300 K, 10% Ni doped MoS_2 thin film. Red, yellow, and green spheres represent Ni, S, and Mo atoms respectively

were fixed throughout the simulation. A Lennard-Jonnes virtual walls was used to prevent atoms from crossing the boundary area at the top edge of the simulation box.

Ni-dopant (% by wt)	Composition (%)			Number of atoms		
	Mo	S	Ni	Mo	S	Ni
0	33.5	66.5	0.0	2714	5386	0
2	33.0	66.1	0.9	2673	5354	73
10	32.2	64.4	3.4	2608	5216	275
15	32.4	62.2	5.4	2624	5038	437

Table 3.1: Composition of sputtered films by Ni-dopant from previous experimental measurements [118] used to define the model systems.

The initial configuration was a substrate of one MoS_2 sheet built using VESTA [125]. The atoms above 0.2 nm were subject to energy minimization and equilibration at the deposition temperature. Next, Mo, S, and Ni atoms were continuously deposited into the simulation box from a height of 7.0 nm above the substrate surface. The deposition ratios used, shown in Table 3.1, were based on concentrations reported from X-ray photoemission spectroscopy (XPS) data of MoS_2 Ni-doped at 0, 2, 10, and 15 % by weight [118]. Deposition rates for Mo or Ni were one atom every 40 fs with deposition energies of 10 eV; for S atoms, the deposition rate was one atom every 20 fs with a deposition energy of 0.5 eV. The deposition temperatures were 300 K and 670 K. Following previous simulations of deposition [36], a reflective virtual wall was placed above the substrate to reflect S atoms (deposited at lower energy) that initially did not remain in the film back downward. The reflective wall started at a z-position of 4.8 nm and then moved upward at a velocity of 2.5 nm/ns as the film grew to a final z-position of 5.5 nm. A snapshot of the 300 K, 10% Ni system after 0.01 ns of deposition is shown in Fig.3.1(A). Deposition continued until 8,100 atoms were deposited.

After deposition, the reflective virtual wall was removed and deposited films were equilibrated for 0.75 ns at the simulation temperature for a total simulation time of 1 ns. This duration was determined to be long enough based on the mean density of the film which was found to reach a steady-state value at around 0.25 ns after deposition. A snapshot of the 300 K deposition with 10% Ni after the equilibration process is shown in

Fig.3.1(B). After equilibration, any unbonded S atoms were removed from the system in preparation for compression and shearing simulations.

3.2.3 Effect of Ni Concentration on DFL Shear Behavior

To study the tribological properties of the sputter deposited MoS_2 thin films, a shearing protocol was implemented for the four different Ni percentage cases sputtered at 300 K. First, a counter surface was constructed from the bottom the previously sputter deposited film (the bottommost 2.1 nm of the model, approximately three layers of MoS_2). This counter surface was rotated by 180°and then placed 1 nm above the deposited film, as shown in Fig.3.1(C). The new model, containing both the deposited film and counter surface, was minimized using conjugate gradient method. In the newly created simulation cell, the atoms in the top 0.31 nm were treated as a rigid body and the atoms in the bottom 0.31 nm were fixed. The system was equilibrated in an NVT ensemble at 300 K temperature for 100 ps.

Next, a 5 GPa pressure was applied to the top rigid layer, moving it downward in the z-direction towards the deposited material. The system was compressed for for 200 ps until the height of the center of mass of the top rigid body reached steady state. Finally, while maintaining a pressure of 5 GPa, a velocity of 50 m/s was applied to the top rigid body in the x-direction, as shown in Fig.3.1(D). The total simulation time for the sliding step was 2.5 ns. During sliding simulation, the shear force in the x-direction on upper rigid wall was calculated and averaged every 5 ps. Shear stress was then calculated from the average shear force divided by the x-y cross-sectional area of the simulation cell.

3.3 Results and Discussion

3.3.1 Deposition and Annealing to Evaluate the Potential

Snapshots of the model system before deposition, after deposition, and after annealing are shown in the top panel of Figure 3.2(I), (II), and (III), respectively. Visually, the model system appears amorphous at the end of deposition, consistent with experimental observations for magnetron-sputtered MoS_2, [122, 126] but then is mostly crystalline after annealing, as observed after annealing in experiments. [122, 126] Note that the middle

region of the material (Figure 3.2(III)) does not appear crystalline from this view, but is in fact crystalline at an angle relative to the perspective shown here. An alternate angle from which the crystallinity of the entire model is visible is shown in Fig. S16. The crystallization process can be quantified using radial distribution functions (RDFs) of S–S, S–Mo, and Mo–Mo atom distances at the end of each stage of the simulation. The RDF of the initial crystal substrate after equilibration, shown in Figure 3.2(bottom panel (I)), exhibits clear peaks indicative of a perfect crystal. At the end of the deposition, Figure 3.2(bottom panel (II)) shows broad close-distance peaks and only weak further-distance (second neighbor) peaks, indicating an amorphous structure. Then, the RDF after annealing, shown in Figure 3.2(bottom panel (III)), has the regular peaks again, only slightly broadened from the before-deposition peaks, confirming that the material is in fact crystalline.

Visual analysis of the simulation after annealing suggested that most of the Ni atoms positioned themselves at Mo sites, resulting in a Mo-substituted Ni-doped MoS_2 structure. To confirm this, the distribution of Ni–S and Ni–Mo distances at the end of annealing are shown in Figure 3.3(b). The heights of the first Ni–S (red) peaks after annealing are at similar distances to those observed in Figure 3.3(a) for the Mo–S (red) peak. We can conclude that Ni atoms are bonded to S more than to Mo, consistent with the Mo-substituted Ni-doped MoS_2 structure. Previous DFT calculations have shown that, under S-rich conditions, Mo-substituted is the most favorable doping location for Ni. [127] Visual analysis of the post-annealing simulations also indicated that the Ni atoms were not randomly distributed throughout the crystal, but rather formed few-atom clusters. This observation is consistent with phase separation predicted for Mo substitution according to convex hull analysis of DFT calculations.[127] Similar behavior has been previously observed for gold atoms co-sputtered with MoS_2, [112] which is further support for the physical realism of these simulations and the new force field.

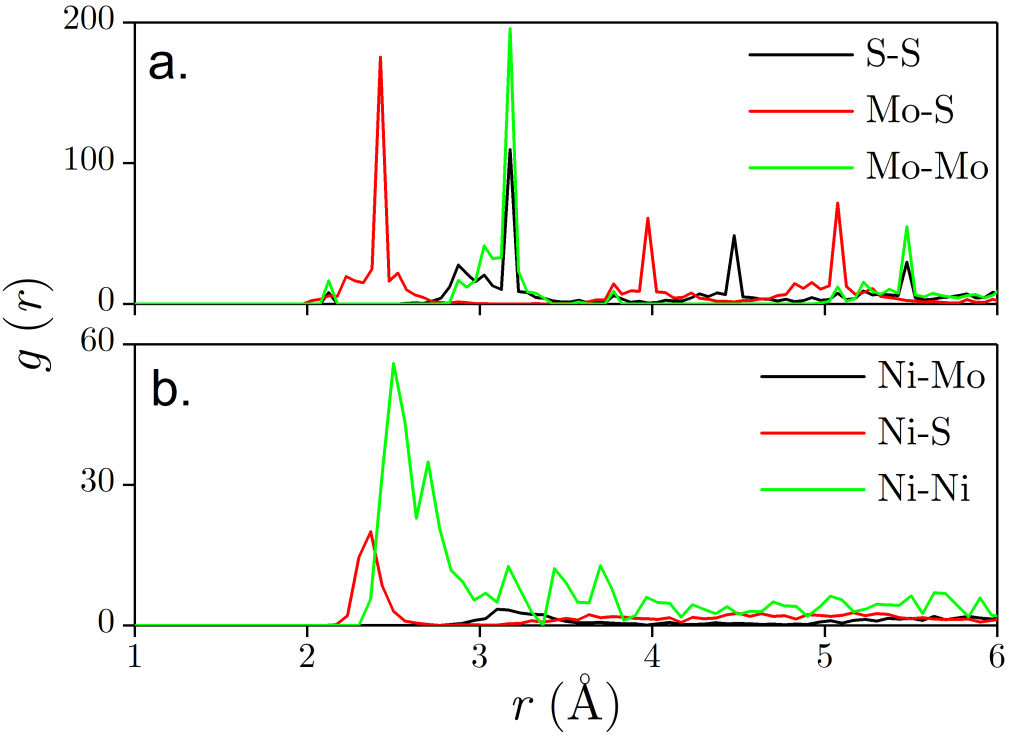


Figure 3.3: Radial distribution functions for (a) 2H MoS_2 substrate before deposition and (b) system after annealing. Similar peak locations for Ni–S and Mo–S, and for Ni–Mo and Mo–Mo, indicate occupation of Mo sites by Ni after annealing.

3.3.2 Sputtering Deposition at Different Temperatures and Ni Concentrations

Snapshots of the model systems after 300 K deposition and equilibration are shown in Fig. 3.4. In all four cases, there was visual evidence that the degree of crystallinity of the material decreased with increasing distance from the bottom MoS_2 layer onto which the atoms were deposited. Also, comparing the three doped films, there appeared to be clustering of Ni atoms in the higher Ni concentration cases.

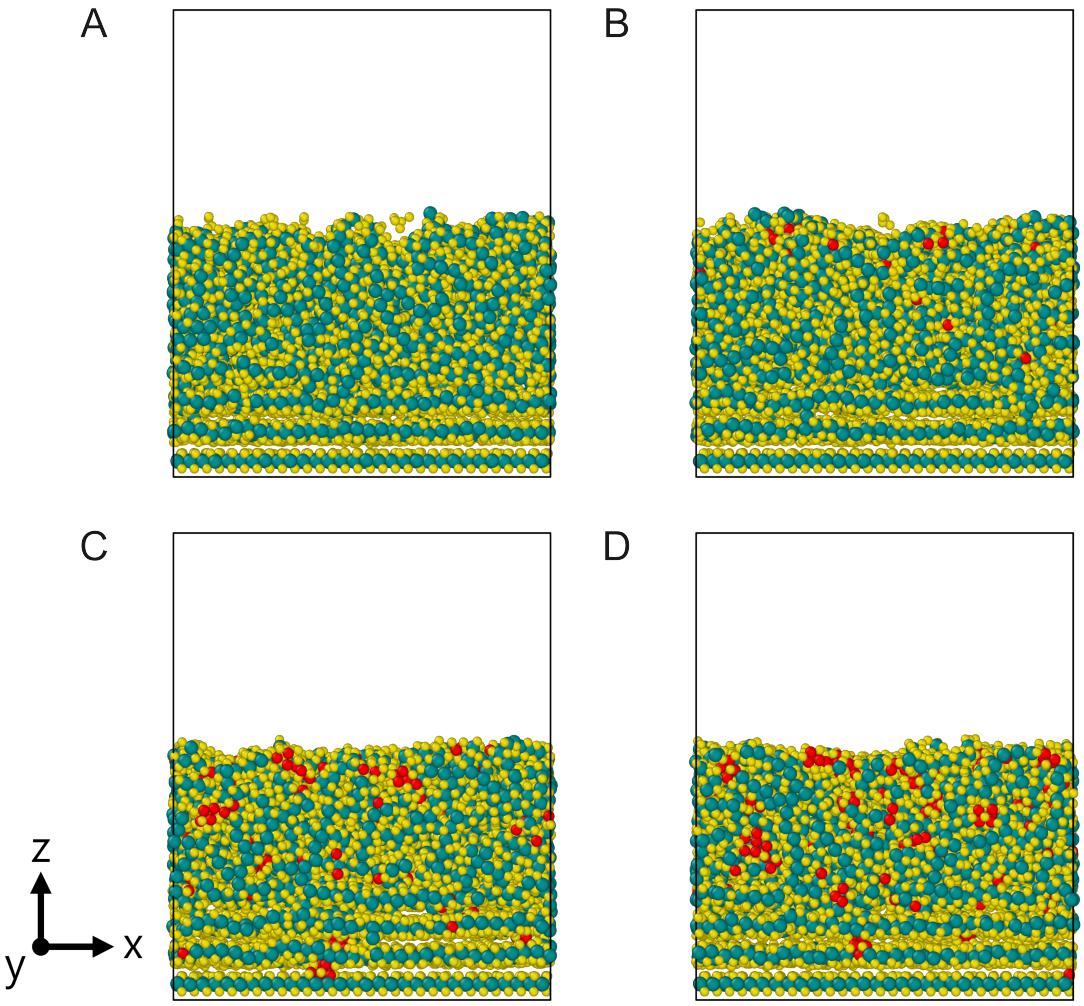


Figure 3.5: Snapshot representations of (A) undoped, (B) 2 % Ni, (C) 10 % Ni, and (D) 15 % Ni doped MoS_2 depositions at 670 K after equilibration. Colors are same as those defined in Fig. 1 of the main paper.

Similar visual trends were observed from the 670 K deposition simulations, shown in Fig. 3.5. The density, crystallinity, and Ni clustering in the films were quantified and compared across the different temperature and Ni concentration cases.

First, the density of the films was evaluated. Density was calculated as a function of vertical position by dividing the simulation cell into 0.6 nm thick bins, as shown in Fig. 3.6(A). Steady state density was calculated from the mass of the atoms in each bin divided by the bin volume, averaged over the last 0.5 ns of the deposition simulations. The results in Fig. 3.7 show the highest density near the substrate for all temperatures

and Ni percentage cases.

The density decreases farther from the substrate, consistent with observations in a previous experimental study of MoS_2 films [97].

In the bulk of the film (between 2.0 and 4.0 nm), there was no statistically significant difference between the average densities at the various temperature and Ni percentage cases, with an average density across all cases of 3.98 ± 0.07 g/cm^3. Previous experimental studies reported a density of 4.3 g/cm^3 [27] which is slightly larger than that calculated in the bulk of the simulated film. The difference in density is likely due to the short time scale of the simulations which does not allow for complete densification of the film. Regardless, the analysis of film density suggested that subsequent characterization of the deposited films should focus on the region between 2.0 and 4.0 nm.

Visual analysis of the material evolution with time (shown for the 300K, 10 % Ni doped case in Fig 3.9 (A)) indicated that the deposited material contained both amorphous and crystalline regions. The binning approach described above for calculating density was implemented to quantify the crystallinity of the material based on Mo and S bond distances and angles [31]. Briefly, Mo atoms with six bonded neighbors (S in the undoped system and S or Ni in the doped systems) were identified. Then, the angle between each of those Mo atoms and its neighbor atoms (Neighbor-Mo-Neighbor) was calculated. The angles were compared to ranges provided in literature [31] to identify atoms in an MoS_2 crystal structure. Finally, the crystallinity percentages were calculated from the number of Mo in a crystal configuration divided by the total number of Mo atoms in the bin.

Crystallinity as a function of vertical position averaged over the last 0.5 ns of equilibration is shown in Fig. 3.8(A) and (B).

Similar to the density trend, the highest crystallinity occurred in the material deposited directly on the substrate and then crystallinity decreased with increasing distance. It has been reported that the microstructure of sputtered deposited materials is influenced by the substrate lattice structure [128]. In our case, the ideal crystal lattice of the substrate acted as a template that facilitated the formation of highly crystalline material at the deposition-substrate interface. The difference between the average crystallinity of the bulk film between 2.0 and 4.0 nm was not statistically significant for the different temperature or Ni concentration cases (Table 3.2 and Fig. 3.9(B)) and the mean bulk crystallinity for all cases was $35\% \pm 3\%$.

Ni (%)	Temperature (K)	Density (g/cm^3)	Bulk Density (g/cm^3)	Crystallinity (%)	Bulk Crystallinity (%)
0	300	4.08 ± 0.62	3.91 ± 0.20	46.72 ± 0.27	38.49 ± 4.97
2	300	4.10 ± 0.58	3.94 ± 0.13	47.62 ± 0.33	35.31 ± 7.45
10	300	4.13 ± 0.55	4.04 ± 0.12	45.52 ± 0.32	32.07 ± 17.00
15	300	4.19 ± 0.49	4.10 ± 0.11	45.87 ± 0.26	30.13 ± 2.44
0	670	4.05 ± 0.64	3.93 ± 0.17	46.91 ± 0.42	38.12 ± 2.23
2	670	4.05 ± 0.58	3.90 ± 0.07	45.66 ± 0.50	35.25 ± 4.27
10	670	4.11 ± 0.52	3.97 ± 0.03	46.91 ± 0.40	35.61 ± 15.44
15	670	4.18 ± 0.42	4.04 ± 0.07	45.60 ± 0.45	32.60 ± 2.90

Table 3.2: Density and crystallinity averaged over the last 0.5 ns of the post-deposition equilibration stage. The "bulk" density and crystallinity correspond to the material at vertical positions between 2.0 and 4.0 nm.

To further analyze the influence of temperature and Ni on crystal formation and nanostructure, we calculated radial distribution functions (RDFs) of the Ni-S, Mo-S, and Mo-Ni atom distances after 0.5 1 ns of equilibration, as shown in Fig. 3.10. The positions of the peaks for Mo-S and Ni-S atom distances were the same at both temperatures and, for Ni-S, the same at all three Ni percentages. However, for Mo-Ni atom distances, there was some difference between the cases for the second peak, which appeared around 0.55 nm (at the same position as the second peak in the Mo-S RDFs). This peak was more prominent at 670 K compared to 300 K and for the higher Ni concentration cases (10 % and 15 %). This observation indicated a more ordered arrangement of Mo-Ni atoms in films deposited at higher temperatures which may be explained by more sulfur vacancies in the higher energy conditions [129] that could then be occupied by Ni atoms.

It has been reported that, during co-sputtering of MoS_2 Ni films, Ni is dispersed in small disordered clusters that influence the film growth [100].

Fig. 3.12 shows snapshot representations of the Ni atoms at the end of equilibration where some clustering is observed, particularly at the higher Ni percentage cases. To quantify this, Ni cluster size was defined based on number of Ni atoms bonded to one another and tracked over time for each temperature and Ni percentage case. Analysis of

Ni clustering as a function of time showed that the cluster sizes were relatively constant after about 0.5 nm (Fig. 3.11).

The distributions of steady-state cluster sizes (quantified by number of Ni atoms per cluster) are shown in Fig. 3.13(A) and (B). The histograms were fitted to skewed probability density functions to better visual the differences between the different cases. The mean cluster sizes at temperatures 300 K and 670 K were 2.26 and 2.15 for 2% Ni, 3.37 and 3.94 for 10% Ni, and 4.83 and 5.30 for 15% Ni, respectively.

Although the mean cluster size was slightly larger at the higher temperature for the 10 and 15% cases, the effect of temperature was minimal compared to that of Ni concentration. At either temperature, the size of Ni clusters increased with Ni concentration.

3.3.3 Effect of Ni Concentration on DFL Shear Behavior

The equilibrated MoS_2 coatings from the 300 K deposition simulations were confined, compressed, and sheared. The shear stress on the top layer during the shearing stage is shown in Fig. 3.14. During the run-in period, all films show and initial steep increase in the shear stress followed by a gradual decrease before converging towards a steady state value. This run-in behavior can be explained by the evolution of density, crystallinity, Ni distribution, and wear particle formation, as discussed later. The shear stress in all four cases fluctuated about a steady-state value after approximately 1.25 ns of sliding.

The average shear stress in steady-state was 5.0 GPa for 0%, 1.9 GPa for 2%, 2.0 GPa for 10%, and 4.3 GPa for 15%. The shear stress was highest for the undoped coating, indicating the Ni was beneficial to the material as a DFL. This is consistent with results from previous experimental studies that showed the wear life of 7% Ni doped MoS_2 films was longer than that of undoped MoS_2 at low contact pressures. [116] Interestingly, in Fig. 3.14, the steady-state shear stress does not vary monotonically with Ni concentration. This has been reported experimentally in Ni-doped MoS_2 films where friction was reported to increase when Ni doping exceeded 11% Ni by weight [12].

Visual analysis of the dynamic evolution of the material structure during shearing (Fig. 3.15) indicated different sliding mechanisms for the different cases. Particularly, the 2 % and 10 % Ni doped films exhibited the formation of a wear particle or debris. It has been proposed previously that MoS_2 DFLs function through a mechanism involving the formation of lubricious wear particles [116, 130–132]. These particles are believed to form

during run-in and provide lubrication. Although the simulations cannot capture wear because of the periodic nature of the model, the formation of particles or debris can be seen. Fig. 3.16 shows snapshots of the four model systems with the atoms colored based on their lateral displacement. In the cases that exhibited the lowest shear stress, 2% and 10% Ni, there is visual evidence of a particle that contains atoms with displacement between that of the top wall and the lower half of the coating, indicating this particle is accommodating most of the shear.

To quantify these observations, the distribution of density in the material over time was calculated for each Ni percentage case, as shown in Fig. 3.17. In all four cases, the highest density was just above the substrate (around 2.5 nm) and the density of this region increased after the initial 0.5 ns of sliding in all cases.

Also, for the 2% and 10% Ni doped films (Fig. 3.17(B) and (C)), starting around 1 ns, there was a density drop at vertical positions between 4 and 6 nm which was attributable to the fact that this region contained the wear particle with high mobility, as seen in Fig. 3.16. For these two cases, the density of the top half of the films oscillated over time, which could be linked to the large fluctuations of shear stress observed in Fig 3.14 after 1 ns of shearing.

Complementing the density observations, crystallinity was tracked during shear. Like density, the crystallinity of the material evolved over time and was vertical position dependent, as shown in Fig. 3.18. In all four cases, the initially crystal rich regions became more amorphous after the initial few 100s of ps of sliding. After this run-in stage, the crystallinity distribution of the coatings changed little with subsequent sliding. In the 0% and 15% Ni cases, there were regions of higher crystallinity around 1 nm and then again around 3.5 nm. Above that, there was a region of amorphous material corresponding to the location where most of the shear was accommodated. For the 2 % and 10 % Ni doped cases, the upper half of the coating was more amorphous than the lower half. The top amorphous region corresponded to the position of the lubricious particle.

The crystallinity of the wear particles specifically was analyzed for the 2% and 10% cases. As shown in Fig 3.21, the lubricious particles comprised more crystalline material in the core with primarily amorphous surfaces.

Finally, the Ni-cluster size evolution over time during shear is shown in Fig. 3.20(A), (B), and (C). During the simulation run-in period, some of the larger clusters formed

during the deposition were broken into smaller clusters. Despite the decreased cluster size, the trend observed during deposition, i.e., that higher Ni concentration corresponded to larger clusters, was also observed throughout shearing.

For all three cases, the majority of the clusters present during steady-state consisted of single digit Ni atoms with mean cluster sizes of 2.3, 3.1, and 4.2 for 2%, 10%, and 15% Ni-concentrations, respectively. The distribution of the Ni in the lubricious particles formed in the 2% and 10% cases was analyzed visually and, as shown in Fig 3.19, the Ni atoms were present primarily at near the surface of the particles as opposed to in the core.

The above analysis corroborates previous work that proposed MoS_2 DFLs lubricate, at least in part, through the formation of lubricious wear particles [116, 130–132]. Our simulation shear stress results are also consistent with previous studies that showed there is an optimum concentration of Ni for best tribological performance [12, 24]. Together, these observations suggest that the non-monotonic relationship between Ni concentration and DFL performance is partially due to the effect of the Ni on the formation of lubricious debris (Ni has also been reported to affect hardness [12, 23, 24], although that is not something can be directly quantified in these simulations).

The remaining question is how Ni affects the formation or lubricity of wear particles. The wear particle analysis for the 2% and 10% Ni cases showed that the particles are more crystalline in the center and that the Ni atoms tend to be primarily present in the amorphous particle surface as shown in Fig.3.21. This particle does not form in the 0% case because of the strong bonds between Mo and S which facilitate crystallinity and inhibit the formation of distinct particles, i.e., there is no Ni available to separate the particle from the bulk of the film. Lubricious particles do not form in the 15% case either, but for a different reason. In the over-doped case, the large and more prevalent Ni clusters impede the formation of a crystalline particle core. Although we did not simulated higher Ni concentrations, the results indicate that adding more Ni will be even more detrimental to the formation of lubricious particles and adversely affect shear stress.

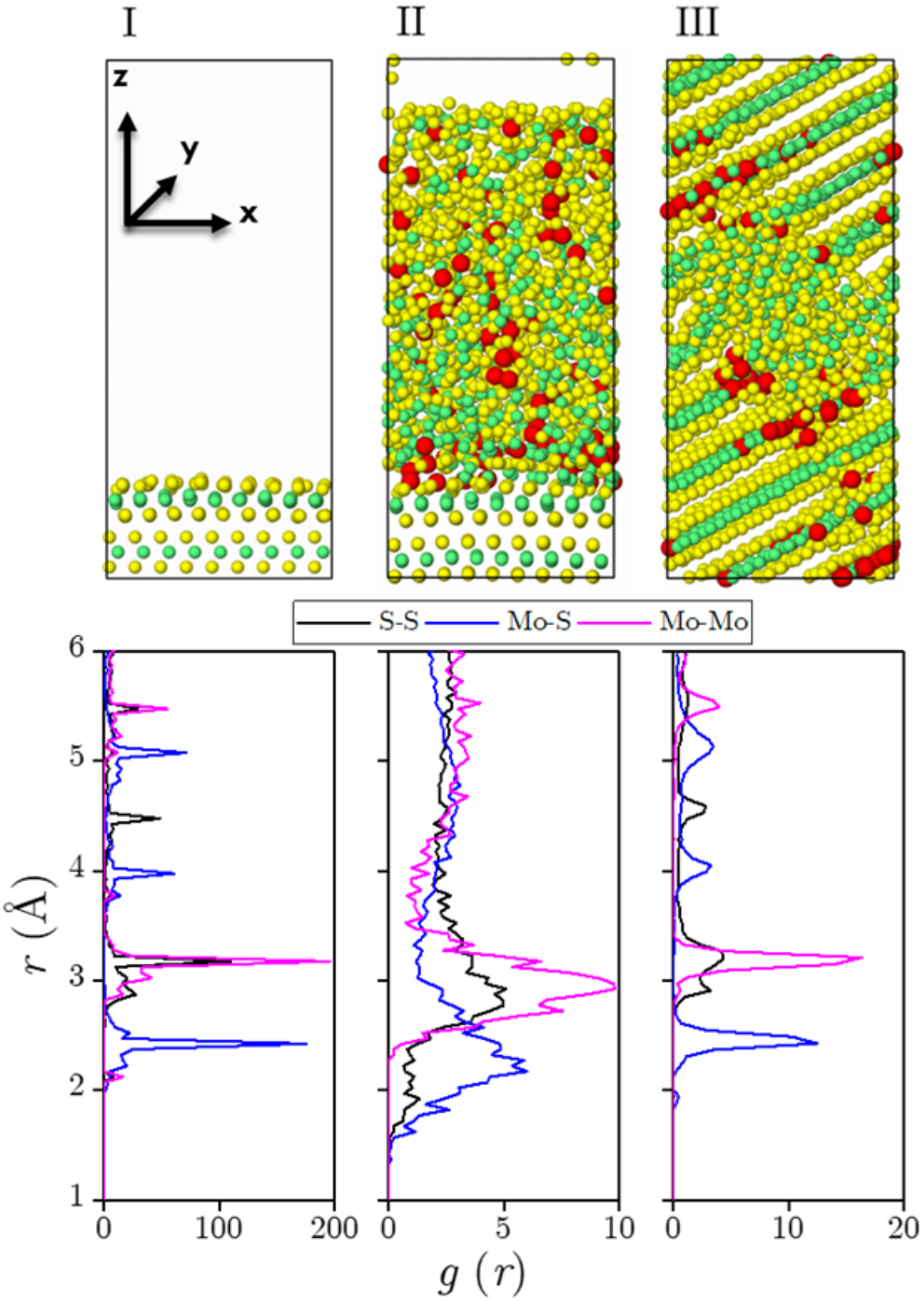


Figure 3.2: Side-view snapshots (top) and radial distribution function (bottom) of the model system, (I) before deposition, (II) at the end of the deposition, and (III) at the end of the annealing stage. A clear transition from amorphous to crystalline is observed (II) $\rightarrow$ (III). Spheres represent S (yellow), Mo (green), and Ni (red) atoms. The black lines in the top snapshots correspond to the periodic boundaries of the cell during the annealing stage.

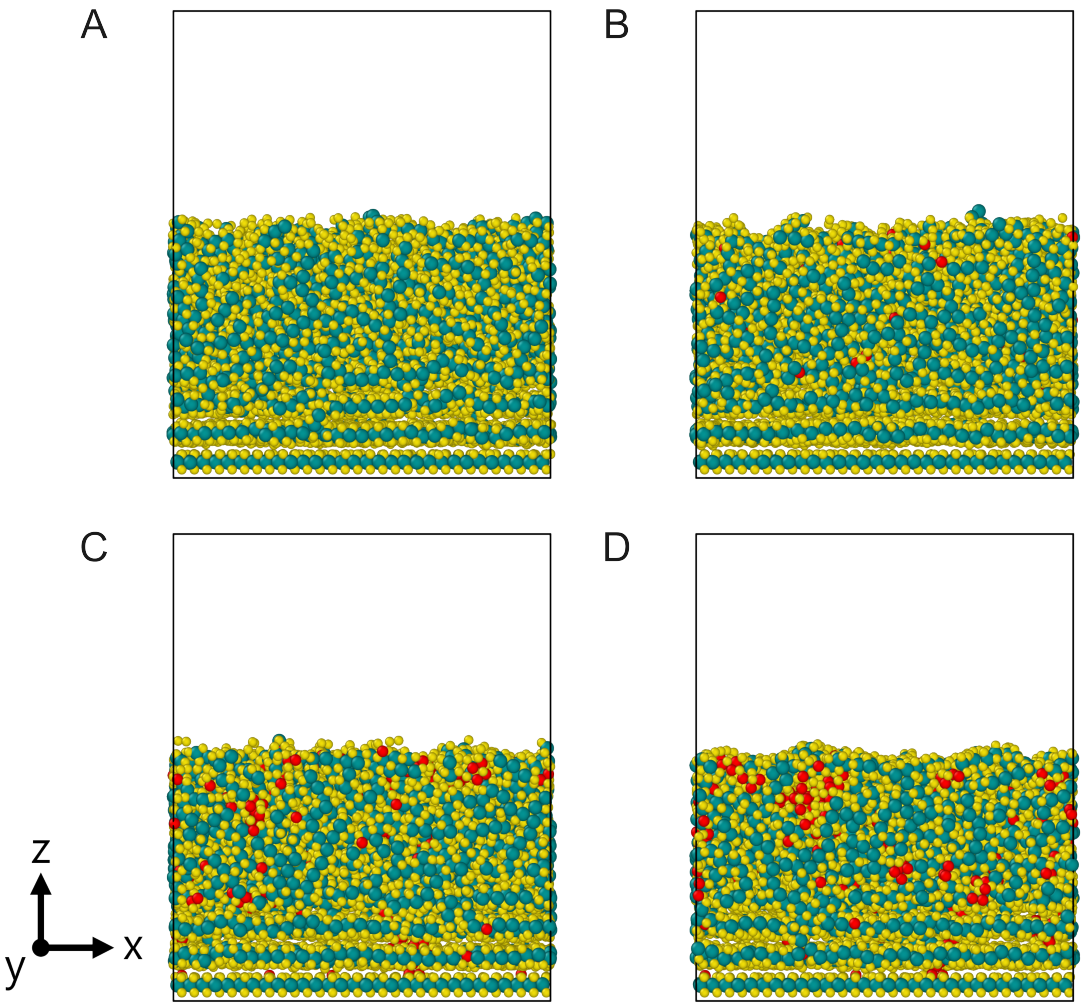


Figure 3.4: Snapshot representations of (A) undoped, (B) 2 % Ni doped, (C) 10 % Ni doped, and (D) 15 % Ni doped MoS_2 depositions at 300 K after equilibration.

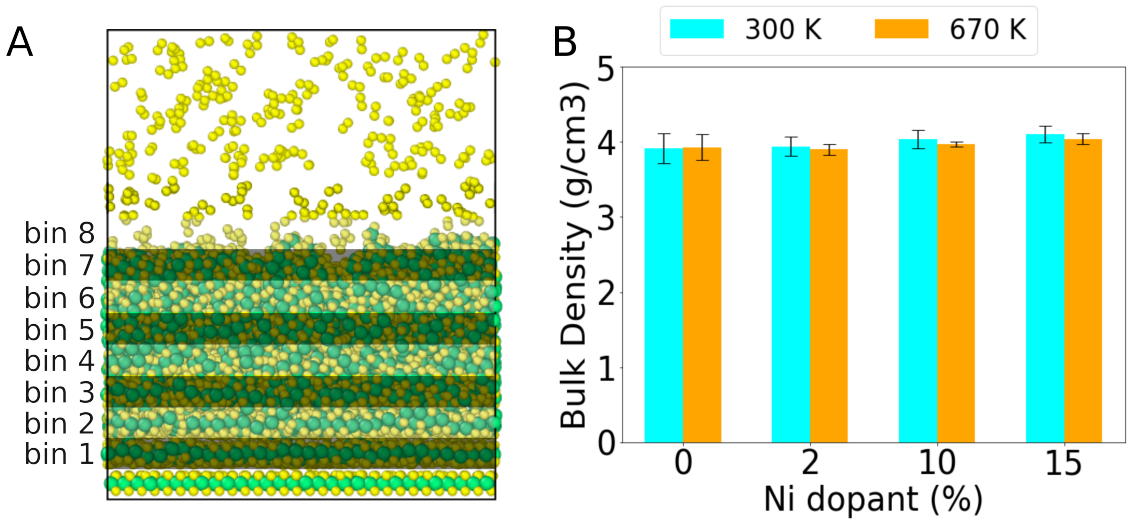


Figure 3.6: (A) Snapshot representation of binned regions used to calculate vertical position dependent density. (B) Average density of all bins where the error bars are the standard deviation for each deposition at 300K and 670K.

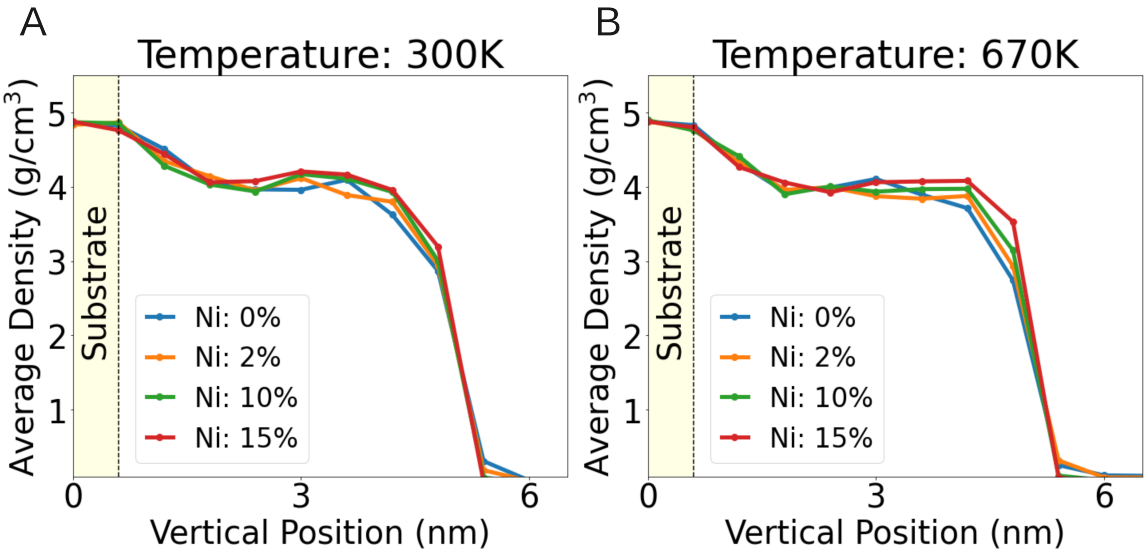


Figure 3.7: Time-averaged density with respect to vertical position for all Ni percentage deposited films at (A) 300 K and (B) 670 K.

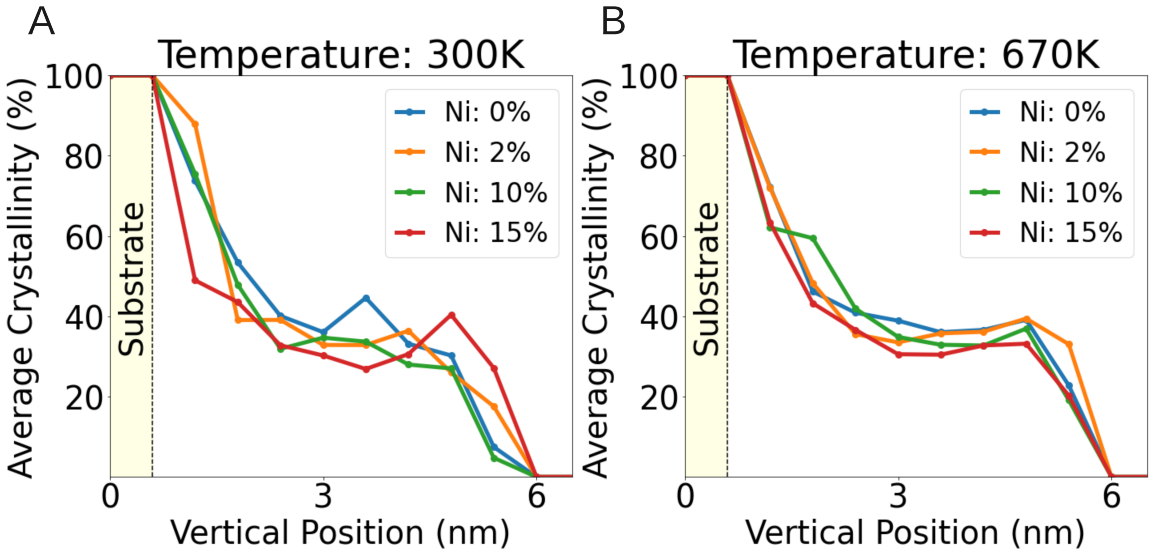


Figure 3.8: Time-averaged crystallinity with respect to vertical position for all Ni percentage deposited films at (A) 300 K and (B) 670 K.

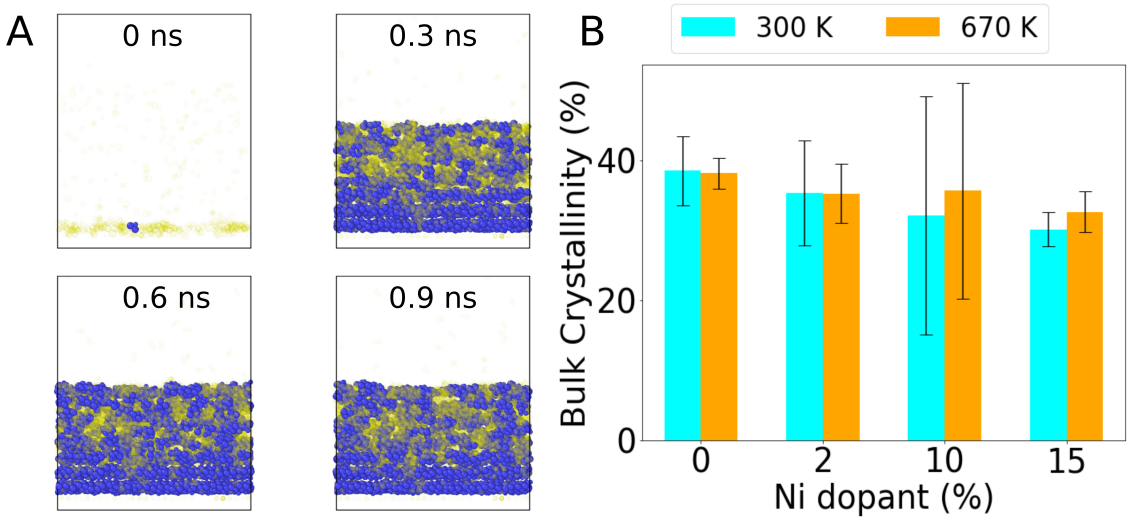


Figure 3.9: (A) Snapshot of the crystal formation during deposition at different times where crystalline atoms are shown in blue and amorphous atoms are shown in partially transparent yellow. (B) Mean crystallinity calculated for the last 0.5 ns of the post-deposition equilibration.

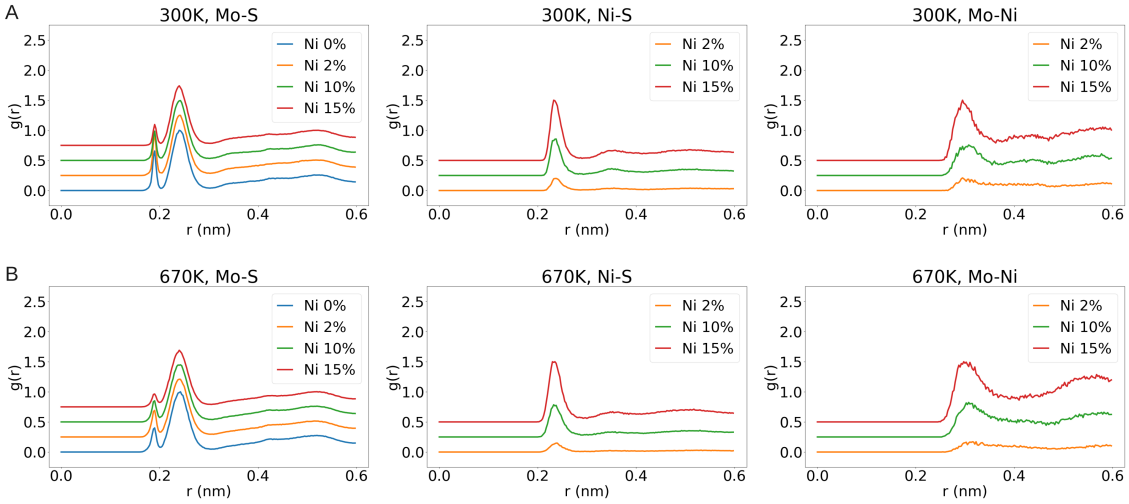


Figure 3.10: Radial distribution function analysis for Mo-S, Ni-S, and Mo-Ni atom pairs at (A) 300 K and (B) 670 K.

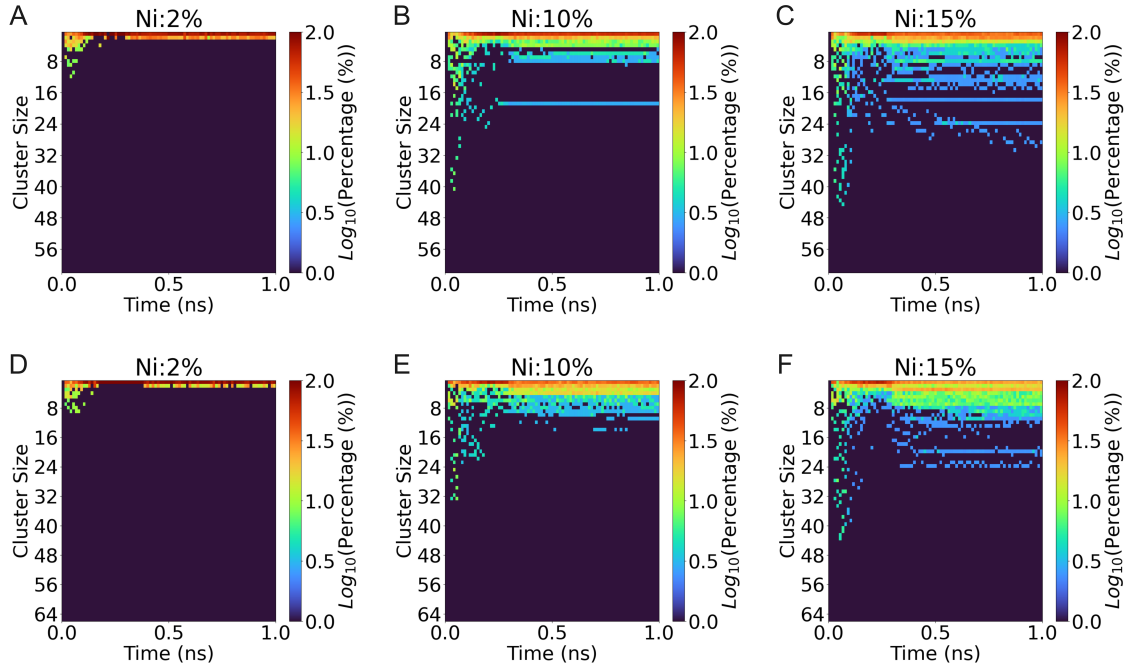


Figure 3.11: Evolution of Ni cluster sizes over time for deposition temperatures 300 and 670 K. Color bars represent the log function of the percentage of a given size.

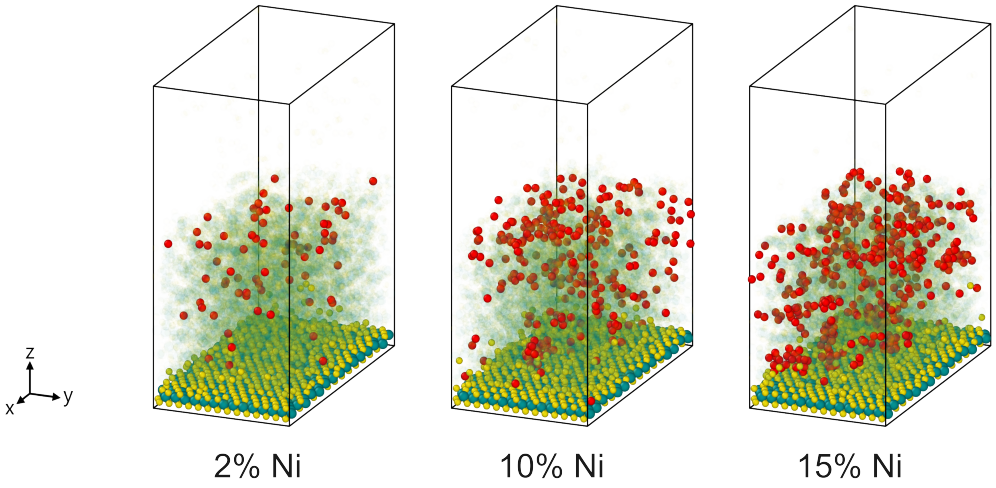


Figure 3.12: Snapshot representations of Ni atoms at time 1 ns for equilibrated depositions at 300 K. Red, yellow and green spheres represent Ni, S, and Mo atoms, respectively, with non-substrate Mo and S atoms shown faded to emphasize the Ni positions and clustering.

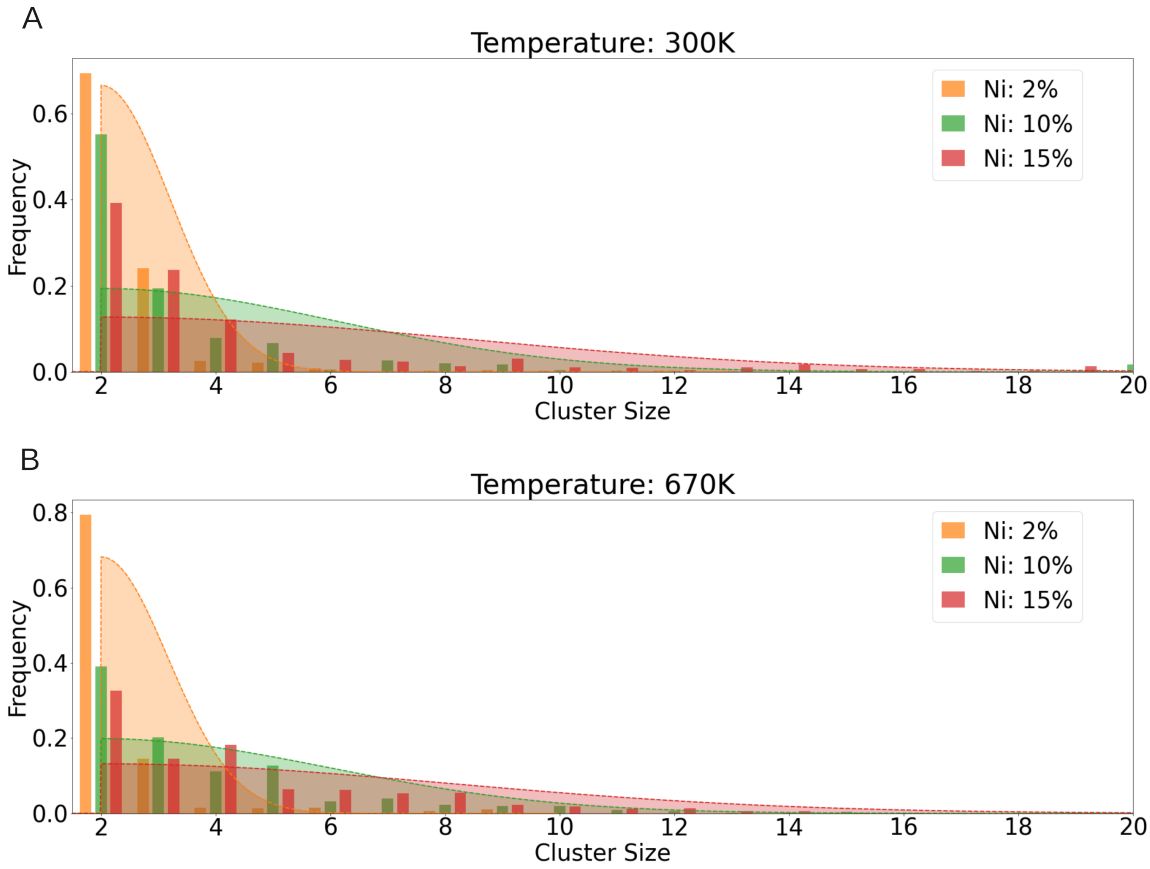


Figure 3.13: Time-averaged Ni cluster sizes distribution for deposition at (A) 300 K and (B) 670 K. Shaded regions correspond to skewed distributions fitted to the cluster size data.

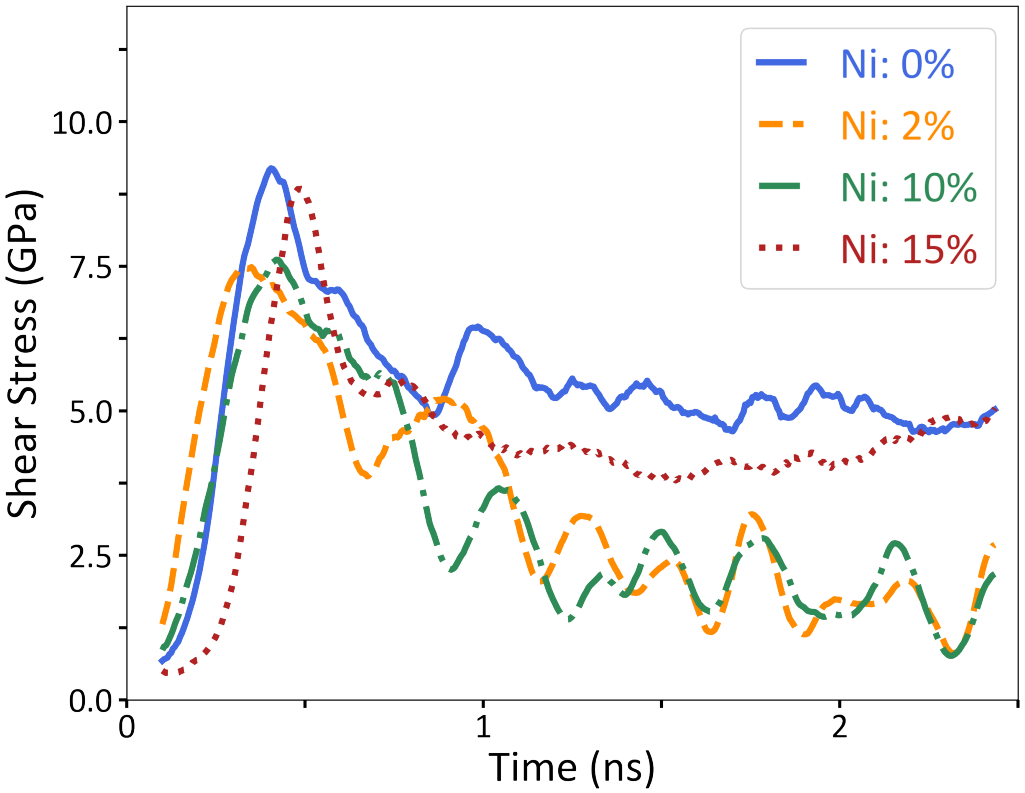


Figure 3.14: Evolution of shear stress during shearing of films sputter deposited at 300 K.

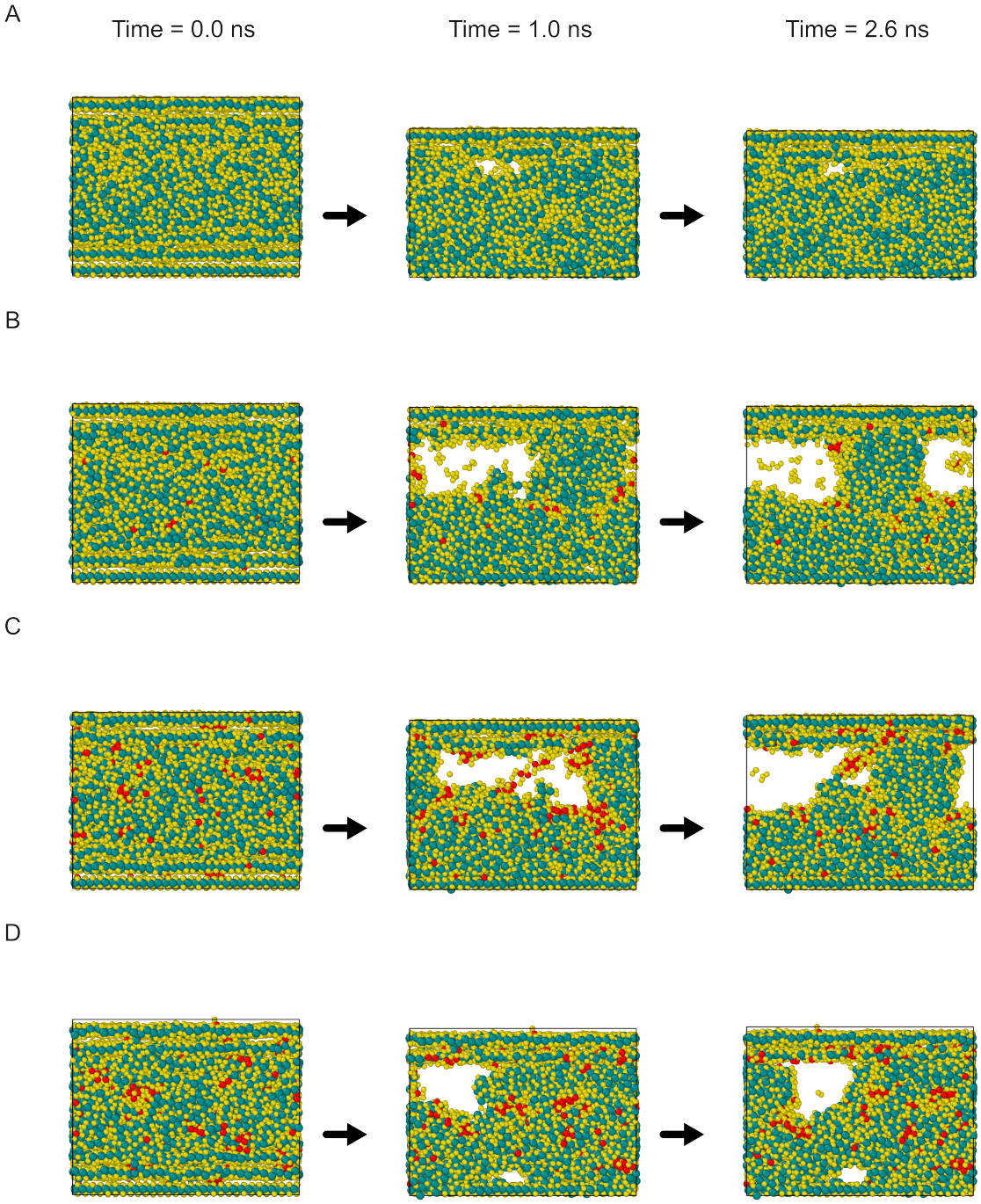


Figure 3.15: Snapshots of the structural evolution at different times (0, 1, and 2.6 ns) for (A) 0%, (B) 2%, (C) 10%, and (D) 15% Ni doped films deposited at 300K during shear.

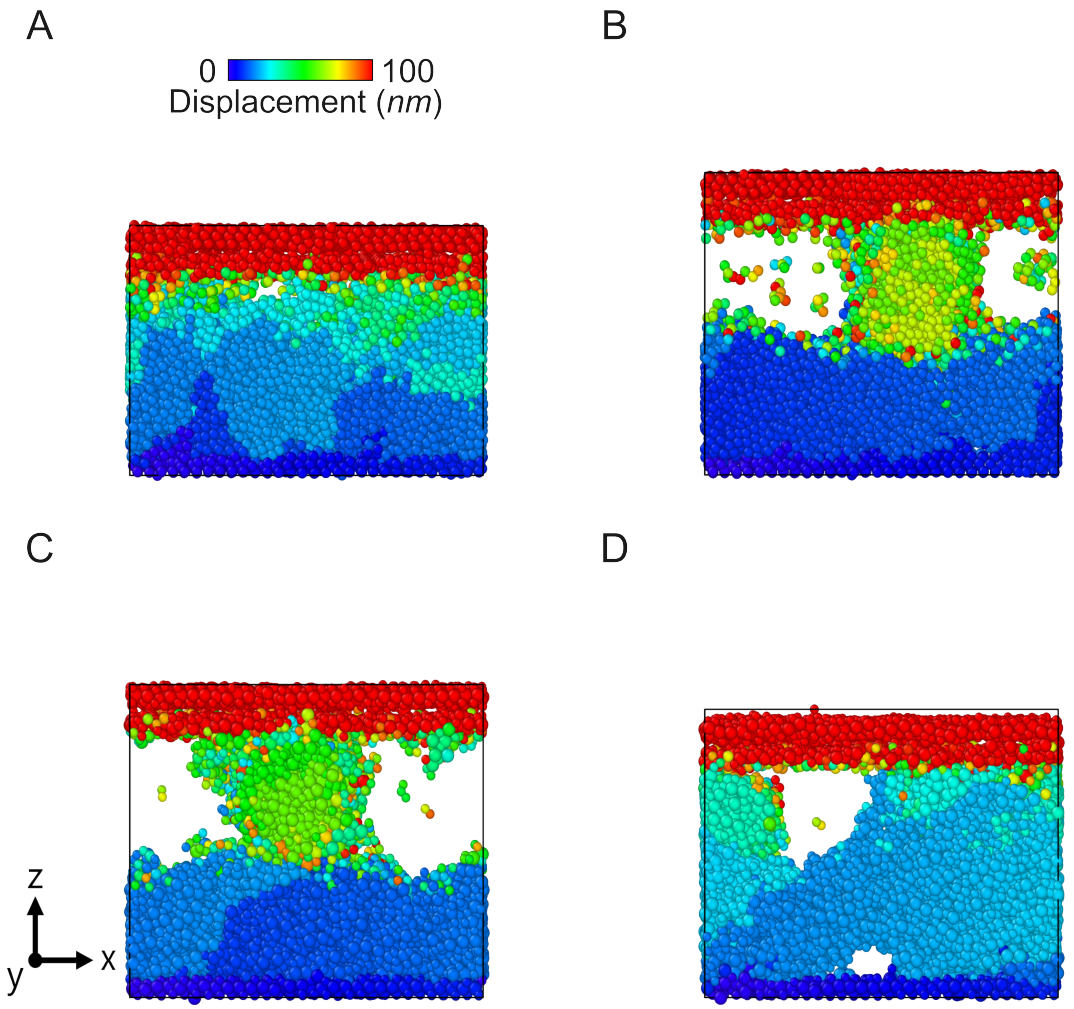


Figure 3.16: Snapshot representation of (A) 0%, (B) 2 %, (C) 10%, and (D) 15% Ni-doped films during shearing at time 2.4 ns. The color represents the x-direction displacement magnitude of the atoms.

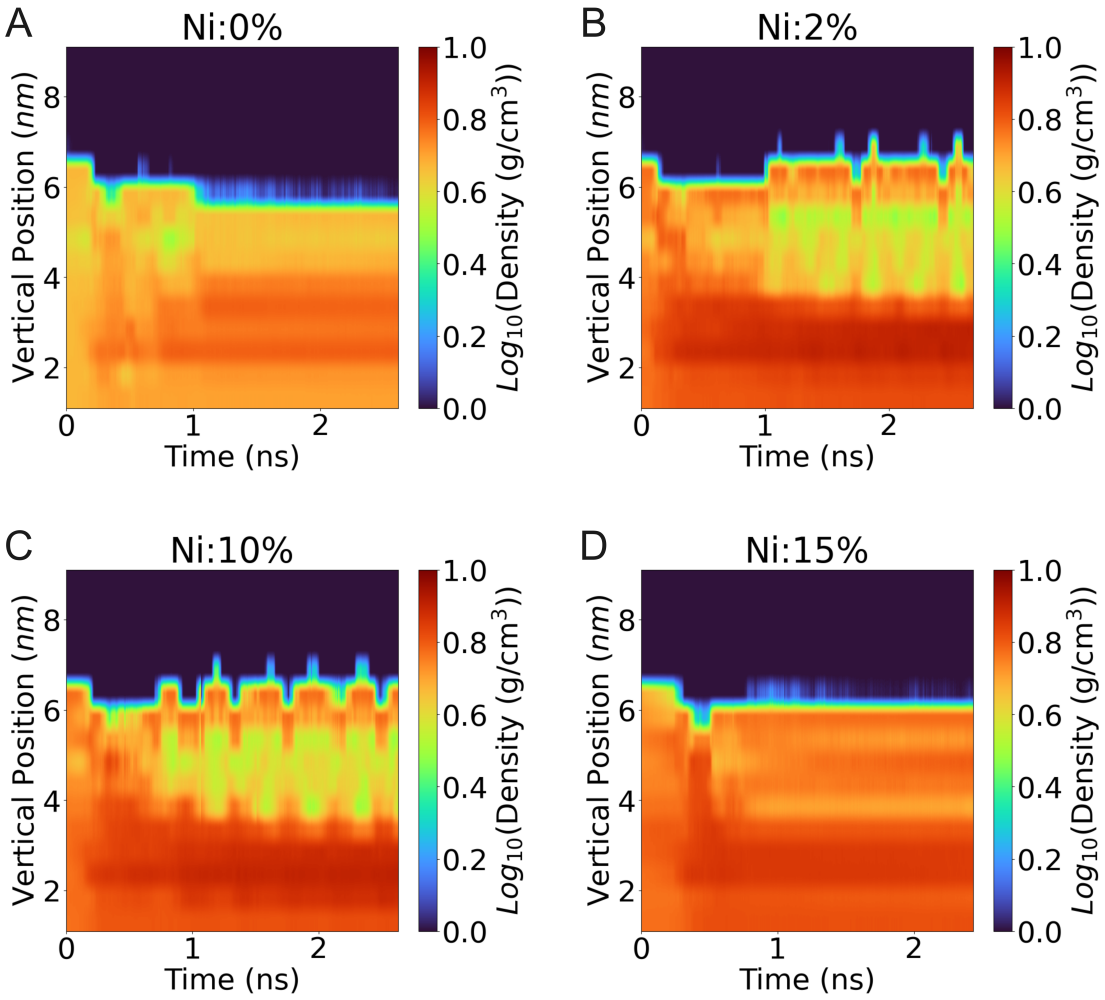


Figure 3.17: Evolution of density as a function of vertical position and time for the shearing simulations (after compression is complete) with color map representing the log of the density for (A) 0 %, (B) 2%, (C) 10%, and (D) 15% Ni doped MoS_2 films.

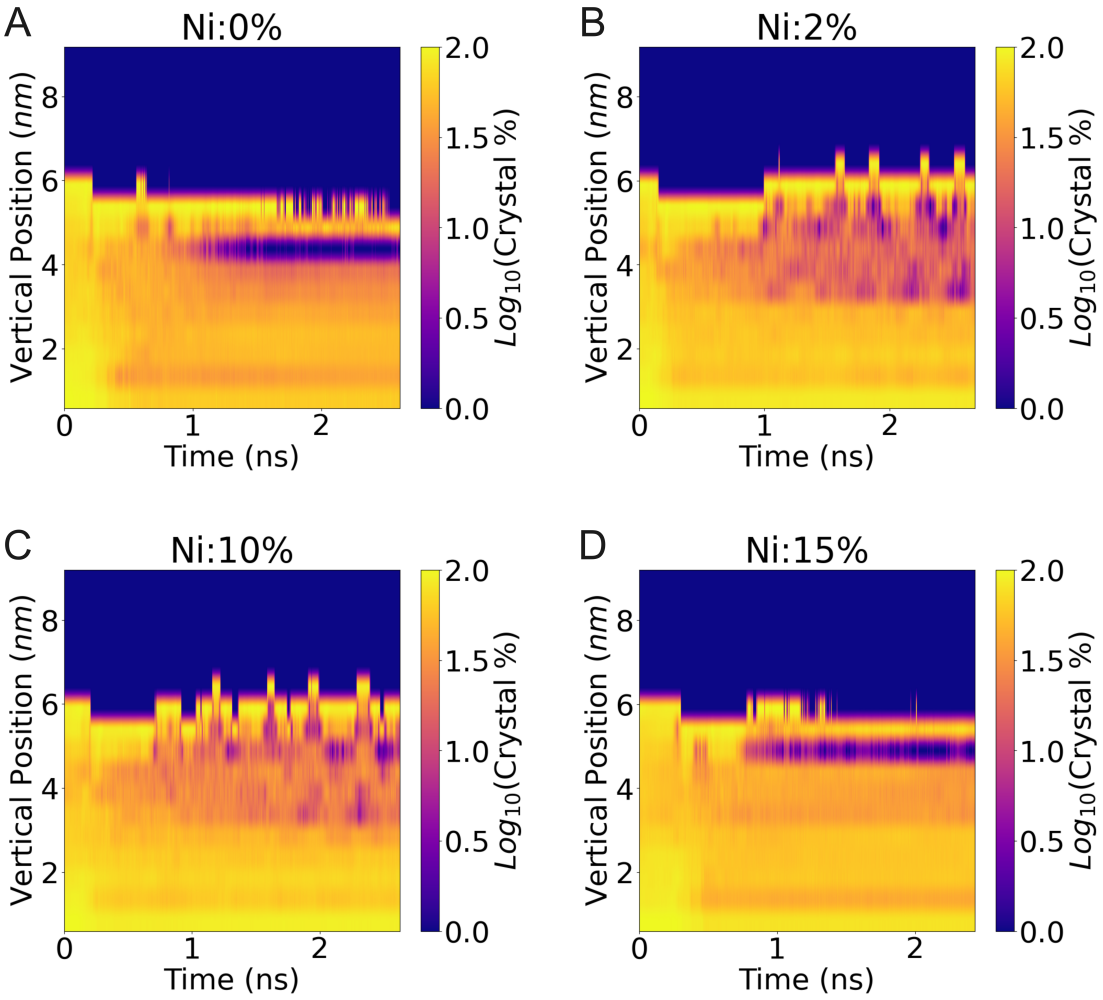


Figure 3.18: Evolution of crystallinity as a function of vertical position and time during shearing simulations with color map representing the log of the percent crystalline material for (A) 0 %, (B) 2%, (C) 10%, and (D) 15% Ni doped MoS_2 films.

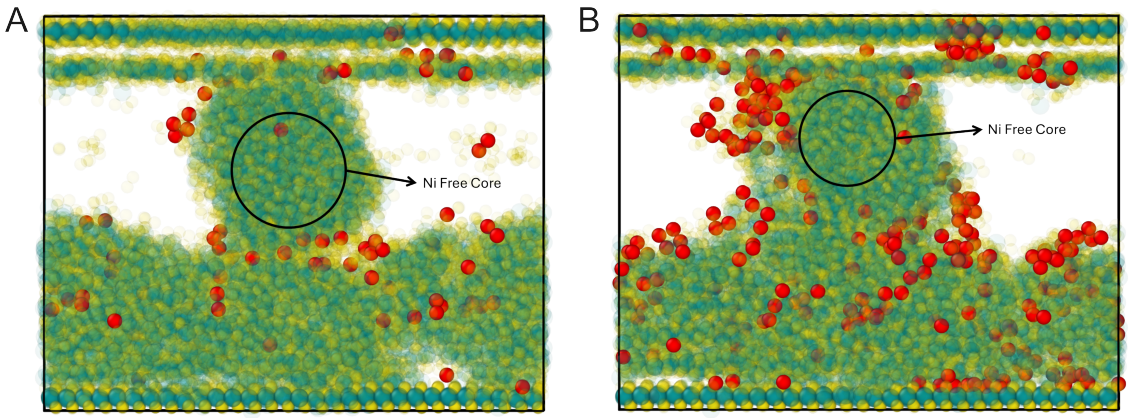


Figure 3.19: Snapshot of the (A) 2% and (B) 10% Ni doped films after 2.4 ns of shearing. Red spheres represent Ni atoms with Mo and S atoms shown translucent green and yellow colors respectively. For both cases the Ni atoms are shown to locate outside of the inner core of the wear particle.

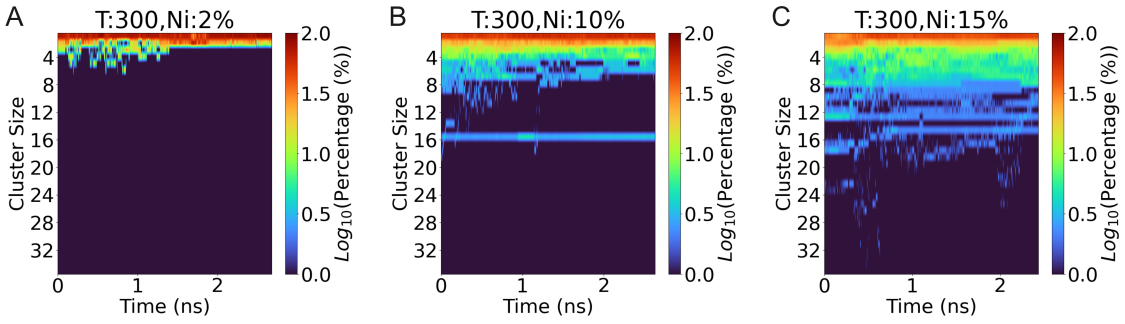


Figure 3.20: Abundance plot of the evolution of Ni cluster sizes over time during shearing simulations with color map representing the log of the Ni cluster size (number of Ni atoms) for (A) 2 %, (B) 10%, and (C) 15%.

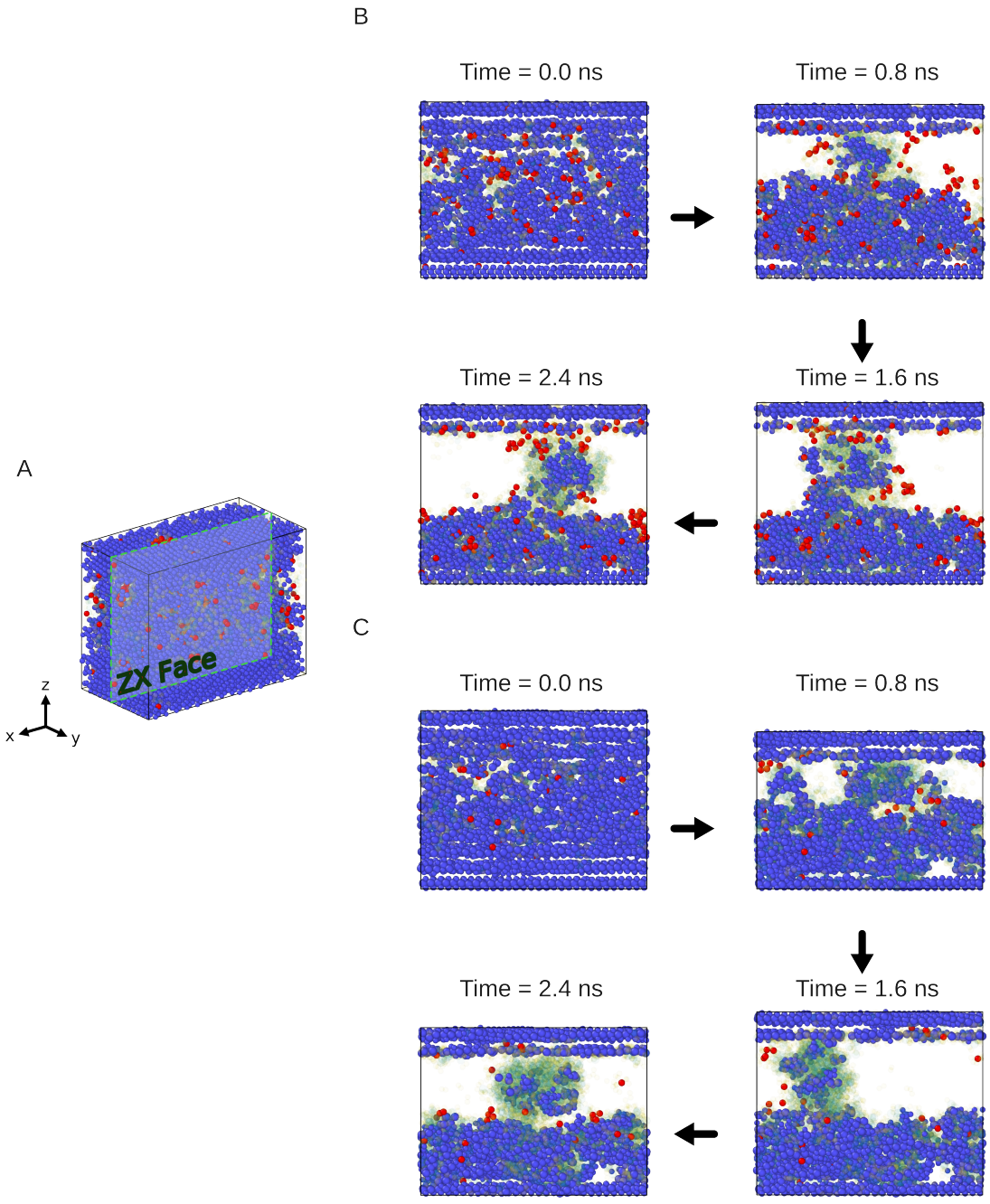


Figure 3.21: (A) Snapshot of the 10% Ni doped film after 2.4 ns of shearing where atoms are colored based on crystallinity. Blue spheres represent atoms in a crystal, translucent spheres are atoms in an amorphous configuration, and Ni atoms are shown as red spheres. The cross-sectional planes in the z-x directions for (B) 10% and (C) 2% Ni concentrations show different simulation frames illustrating the movement of Ni atoms and the formation of the lubricious wear particle during shearing. For both Ni concentrations, the particle shows a crystalline core and an amorphous outer shell with Ni atoms.

3.4 Conclusions

In this study, the effect of Ni dopant percentages on the nanostructure and tribological properties of sputtered deposited MoS_2 was investigated using reactive molecular dynamics simulations.

A sputtering deposition simulation procedure was implemented to form DFLs with different Ni concentration. Simulations of deposition and annealing confirmed that the ReaxFF potential could reproduce the expected crystallinity of Ni-doped MoS_2. Characterization of the films deposited without annealing showed that crystal percentage and density varied across the material vertically, with the highest density and crystallinity observed in the deposited material just above the MoS_2 substrate. Neither temperature nor Ni concentration had a statistically significant effect on density and crystallinity in the bulk of the films. In the cases with Ni dopant, it was found that the Ni formed clusters with a range of sizes and that larger clustered could be formed with higher Ni concentrations. The difference between the nanostructures of the films deposited at 300 and 670 K was minimal and seen only as more long-range ordering of the Mo and Ni atoms in the material.

Shearing simulations for the sputtered DFL deposited at 300 K. The results showed that Ni dopants at 2% and 10% by wt. concentration had a lower shear-stress value at steady state than that for Ni dopants at 0% and 15% by wt. concentration. Further investigation of the density, crystallinity and Ni-clustering during shearing showed the formation of lubricious wear particle for the 2% and 10% films. These particles were found to be more crystalline in the core with amorphous and Ni-containing surface material. This combination of crystallinity and dopant concentration was only possible with the intermediate amounts of Ni in the film.

The findings of this study reveal a mechanism by which Ni dopants can improve the performance of an MoS_2 DFL and provides a possible explanation for the non-monotonic dependence of tribological properties on dopant concentration. Awareness of this mechanism may guide future experiments that directly measure concentration dependence for Ni as well as other dopants.

Finally, the modeling approach developed here might be leveraged to further understand and then improve the performance of these materials.

Chapter 4

Surface Functionalization for Mechanochemical Studies

4.1 Introduction

As stated in Chapter 1, surface functionalization of amorphous silica with aromatic hydrocarbons (AH) involves precise control over molecular packing and covalent bonding. Understanding the mechanisms and outcomes of these processes in a simulated environment is essential for enhancing material properties for specific applications. In experimental settings, AH monolayers are packed using a closed saturated solvent environment, such as PhMe, to facilitate reactions between the hydroxylated substrate and silane-methyl terminated AH molecules [133]. This method opens oxygen reactive sites on the silanol-terminated AH molecules, allowing them to form covalent bonds with the surface.

To focus on the covalent bonding of molecules to the substrate and improve simulation times, the simulations were performed using a model system in which the silica was dehydroxylated and the depositing molecules were AH terminated by a dehydroxylated silanol group, subsequently referred to simply as silanols in this manuscript.

These simulations showed the time evolution of surface density, where the simulated steady-state value was in agreement with density measured using QCM. [134] However, the study did not provide insight into the effect of silanol structure in surface density, which is key for the selection of chemical species for surface functionalization for a specific application.

To understand the effect of molecular structure on the covalent functionalization of amorphous silica with silanols and, specifically, on surface density. We model the condensation reactions between silica and three silanols with different numbers of aromatic rings at three different temperatures. We compare simulation calculated densities with those estimated using simple geometric models based on van der Waals radii. Then, we analyze surface densities in terms of the type and number of covalent bonds formed with the amorphous silica and the orientation and ordering of the silanols, revealing correlations between surface density and local conformational ordering of the silanols on the silica surface. Finally we showed an application on compressive simulations of an inmobilized AH system used to study the molecule distortion of Diels-Alder reactions.

4.2 Methods

The model systems comprised a dehydroxylated silica substrate and aromatic hydrocarbons terminated by a dehydroxylated silanol group (silanols). This simplified model was designed to maximize the number of reactions of interest within the size- and timescale limitation of the reactive MD method, as in our previous study [134].

The amorphous SiO_2 was generated from a cristobalite SiO_2 crystal structure [135] that was heated (5000 K) and fast quenched (300 K) in a simulation box with periodic boundary conditions in all directions and dimensions 5.6 $\times$ 6.0 $\times$ 2.1 nm (x, y, and z). The resulting amorphous structure exhibited Si-O, O-O and S-S peaks and distances characterized by radial distribution functions (SI Fig. 4.2) that showed good agreement with values reported in literature for amorphous SiO_2 thin films [136]. Then, the dimensions of the box were extended to 5.6 $\times$ 6.0 $\times$ 5.5 nm (x, y, and z) to create a surface. The density of accessible dangling bonds on the equilibrated substrate surface before deposition was calculated to be 4.55 nm^{-2} with 153 open sites available for reaction.

Three silanols were modeled – phenyl, naphthyl, and anthracenyl – as shown in Fig. 4.1(A). The silanols were designed with the Avogadro chemical editor [137] and then placed randomly into the simulation box at a distance of at least 0.5 nm from the silica surface using PACKMOL [138]. Characterization of functionalized surface in the corresponding previous experiments suggested complete surface coverage [134]. Based on this, the number of silanols per simulation, 150, was determined as the approximate num-

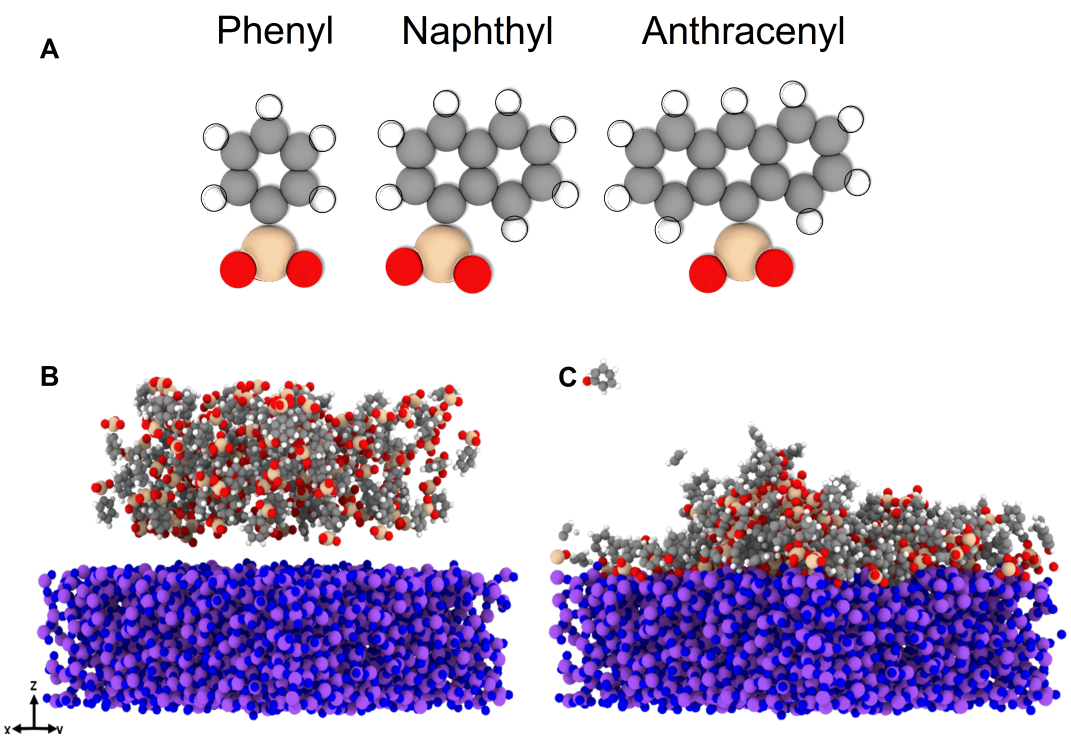


Figure 4.1: (A) Schematic representations of the aromatic hydrocarbons used as reactants in the simulations. Representative side-view snapshots of the model system with phenyl (B) before and (C) after covalent functionalization. Sphere colors correspond to: gray - carbon, white - hydrogen, tan - silicon in the silanols, purple - silicon in the silica, red - oxygen in the silanols, blue - oxygen in the silica.

ber needed to ensure full surface coverage within the short time-scale of the simulations. After this stage, the boundary conditions were periodic in x and y, while the z boundaries were fixed. The bottom most atoms in the silica slab were fixed during the simulation and a repulsive wall was used at the top of the simulation box to prevent silanols from escaping.

Reactive MD simulations were performed using the Large-scale Atomic/Molecular Massively Parallel Simulator (LAMMPS) [139] package. Atomic interactions were modeled with a time step of 0.1 fs using the ReaxFF potential for H/C/O/Si [140] parameterized to maintain thermal stability of C-Si bonds in silicon surfaces functionalized with organic molecules. Initial atom velocities were given by a Gaussian distribution at three different temperatures (300, 400, and 500 K). Simulations were run using the NVT ensem-

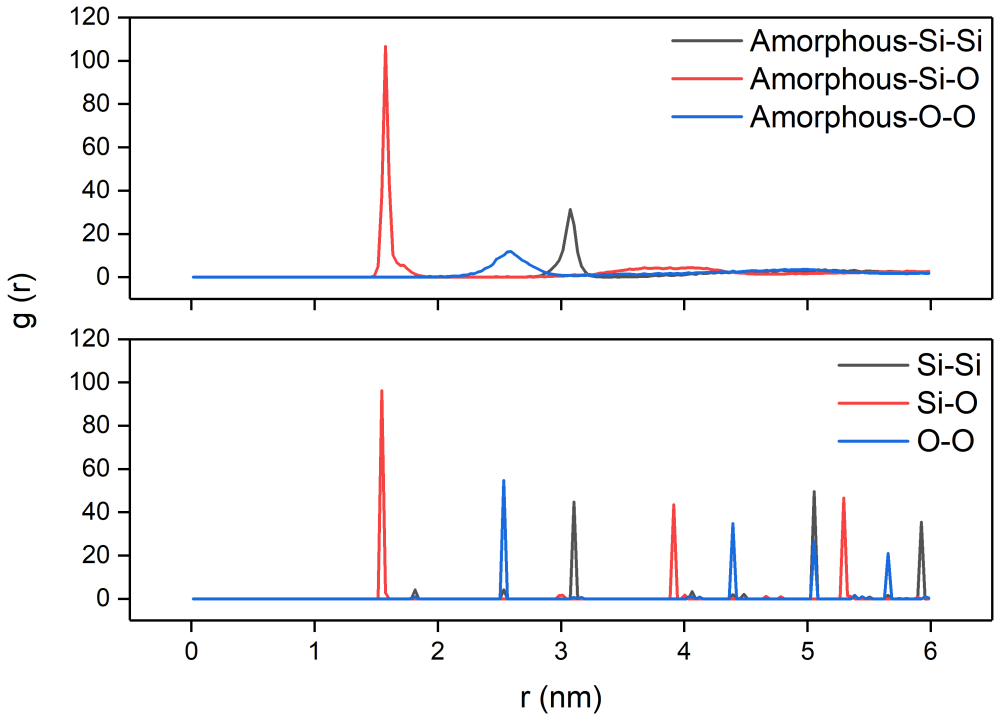


Figure 4.2: RDFs for Si-O, O-O, and Si-Si distances for (top) the substrate used in the simulation and (bottom) a reference cristobalite SiO_2. The simulation substrate RDF peaks are broad and with no long-range order, characteristic of an amorphous materials. The bottom RDF for the cristobalite SiO_2 has the sharp well-defined peaks associated with a crystal structure.

ble (constant number of particles, volume, and temperature) using a Nosé-Hoover [141] thermostat with a damping parameter of 40 fs.

The simulations were run at each of the three temperatures for 0.2 ns, which was determined to be enough time for the surface reactions to reach steady state, as shown in Fig. 4.3. Snapshots of a representative model system before and after the dynamic simulations are shown in Fig. 4.1(B) and (C). Each simulation case was replicated three times using different random seed values for the initial atom velocities such that the repeat simulations were independent. Covalent bonds between the silanols and the substrate were tracked using the bond table available from ReaxFF. Visualization and analysis of atomic chemisorption from simulated data was done in OVITO [142] open-visualization tool and custom scripts written in Python.

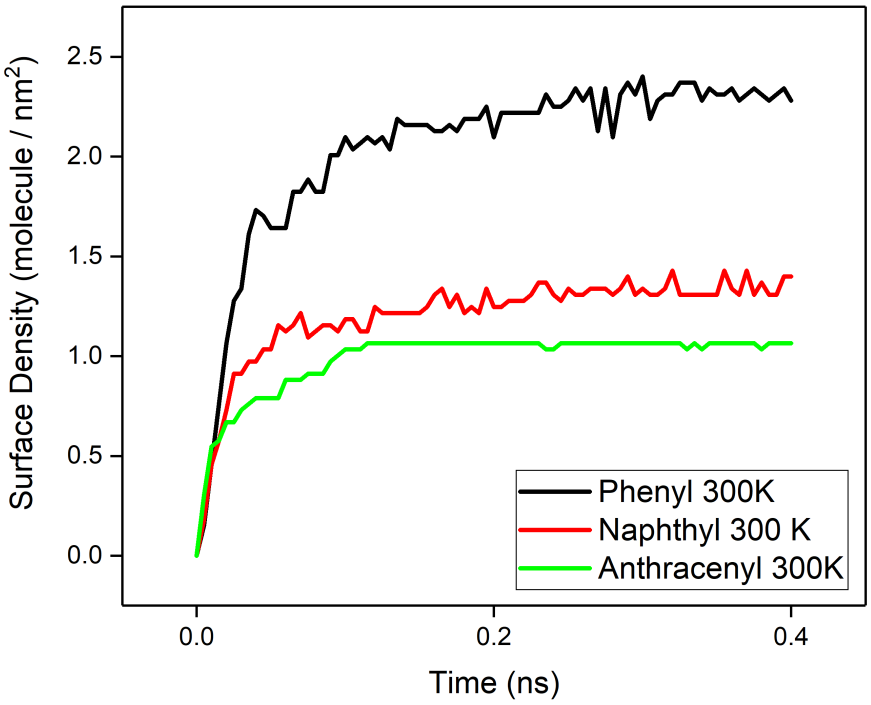


Figure 4.3: Extended simulations for select molecules and temperatures showing surface density steady state is achieved within the simulation times of 0.2 ns.

With the goal of ultimately modeling Diels-Alder reactions, compression simulations were designed with the anthracenyl system described above where 35 maleimide molecules were randomly introduced into the box 4 Å above the uppermost atom in the functionalized substrate. The system was re-equilibrated with the NVE ensemble (constant number of particles, volume and energy) and then the Langevin thermostat [143] applied on the diene and dienophile molecules at 300 K. Compression was performed by moving a repulsive harmonic wall located at the top of the simulation box in the negative z direction. The harmonic wall interacted with the atoms as it moved down, applying compression on pressure to the reactant molecules. The wall was stopped at two positions, corresponding to low and high-pressure cases of 1.7 and 3.0 GPa, and the simulation run longer with the wall position fixed. Although these pressures are far higher than the mean pressures calculated for the tip array experiments, they are used to decrease the time required for molecular processes to occur such that they can be observed within the ns-scale duration

of the MD simulations, which is orders of magnitude shorter than the experiments. Snapshots of the simulation before compression and after compression at these two pressures are shown in Fig. 4.15.

4.3 Results and Discussion

4.3.1 Reactive Simulations of Silica Functionalization with Aromatic Hydrocarbons

During the simulations, chemical bonds formed between silicon in the silanols and oxygen on the silica surface. The number of silanols chemically bound to the surface was tracked (based on the formation of $Si_{silanol}$–O_{silica} bonds) and surface density was calculated from the number of surface-bound silanols divided by the silica surface area (32.9 nm^2). The time evolution of the surface density at each temperature for phenyl, naphthyl, and anthracenyl is shown in Fig. 4.5(A), (B), and (C), respectively. Bond formation occurred as soon as the simulation began and the surface density increased rapidly during the first 0.05 ns in all cases. The density reached a steady-state value after about 0.1 ns. At the end of the simulation, the silica surface was covered by a monolayer of chemically bound silanols, e.g., Fig. 4.1(C).

The steady-state surface density for each silanol and temperature averaged over three independent simulations is reported in Fig. 4.5(D). The results show that temperature did not have a statistically significant effect on surface density but the densities were very different for the three different silanols. Therefore, subsequent analyses focused on the silanols and included data from simulations at all three temperatures. The average steady-state surface density was 2.06 ± 0.12, 1.38 ± 0.15, and 1.15 ± 0.09 nm^{-2} for phenyl, naphthyl, and anthracenyl, respectively. The value for anthracenyl is comparable to surface density previously measured using QCM of 1.12 ± 0.13 nm^{-2} [134]. Further, the trend with respect to the three silanols is consistent with the expectation that the larger silanols should occupy more surface area therefore have lower density.

The maximum possible density for each silanol can be estimated based on the size of the molecules. Specifically, the van der Waals areas of the molecules [144] in the xy plane (visual representations in SI Fig. 4.4) were calculated to be 0.438, 0.582, and 0.720 nm^2, corresponding to maximum surface densities of 2.28, 1.71, and 1.38 nm^{-2} for

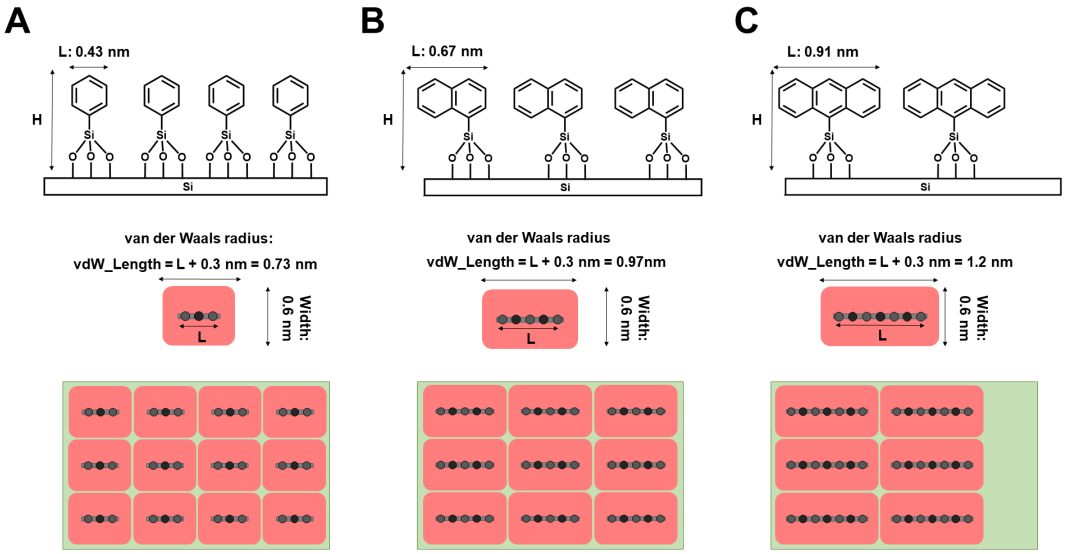


Figure 4.4: Schematic representations of theoretical surface density for (A) phenyl, (B) naphthyl, and (C) anthracenyl aromatic hydrocarbons

phenyl, naphthyl, and anthracenyl, respectively. These values, as well as the densities obtained from simulations and reported from experiments, are given in Table 4.1. The simulation and experimental densities are lower than the maximum based on molecule geometry, which is reasonable since the maximum value assumes the silanols are ideally conformationally ordered, which is not expected to be the case in practice. The biggest difference between simulated and geometric density is for naphthyl. Also, the simulation densities decrease faster with increasing number of aromatic rings than the geometric densities. For example, the ratio of the theoretical densities of anthracenyl and phenyl is 1.65 but was found to be 1.79 in the simulations.

Analysis of anthracenyl chemisorption studied previously [134] showed that there are three types of bonding configurations possible, depending on how many silicon–oxygen bonds are formed, as illustrated in the close-up snapshots in Fig. 4.6(A), (B), and (C). Fig. 4.6(D) shows the distribution of bonding configurations for the surface-bound silanols,

	Surface Density (nm^{-2})		
Method	Phenyl	Naphthyl	Anthracenyl
Geometric Maximum	2.28	1.71	1.38
MD Simulations	2.06 ± 0.12	1.38 ± 0.15	1.15 ± 0.09
QCM Experiments	-	-	1.12 ± 0.13

Table 4.1: Summary of surface density values estimated based on molecule geometry, reactive MD simulations, and previous QCM measurements [134]

including data from all three simulated temperatures. The bond type distribution shows that the likelihood of a given configuration decreased with number of bonds. Specifically, for all silanols, one oxygen bond (1-O) was the most common and the least observed bonding configuration was three-oxygen (3-O) atoms. However, the statistical difference between 1-O and 2-O was smallest for naphthyl and the average percentage of 3-O was the largest for this silanol.

Since the orientation of the surface-bound silanols can play a significant role in the properties of functionalized silica surfaces, the angle of tilt of the silanol with respect to the surface was analyzed. The tilt angle θ was defined as the angle between the plane of the ring(s) in the silanol and the direction normal to the silica surface, as shown in Fig. 4.7(A). The angle was calculated for each silanol bonded to the substrate using data from 0.1 to 0.2 ns of simulation time. The distributions of tilt angles in Figure 4.7(B) are positively skewed where the highest angle probability is 28.4° for all three silanols (distribution modes are 27.9 ± 0.5°, 28.7 ± 0.6°, and 30.3 ± 0.8° for phenyl, naphthyl, and anthracenyl, respectively). This is consistent with the range of angles for self-assembled monolayers (SAM) on amorphous silica which have been reported to be 16° at full coverage [145] and as low as 30° for low coverage [146]. The highest angle probability of 28° for silanols in our study is at the upper end of the range reported for SAMs, consistent with the fact that our surface densities are below the geometric value (Table 4.1). Lastly, although the distributions are very similar for all three silanols, there are more small angles for the phenyl. This is consistent with a previous simulation-based study [147] of alkanethiol SAMs that reported tilt angle increased with chain length.

Another factor that can affect surface density of aromatic hydrocarbons is the orientation of molecules with respect to each other. Fig. 4.8(A), (B) and (C) shows two point

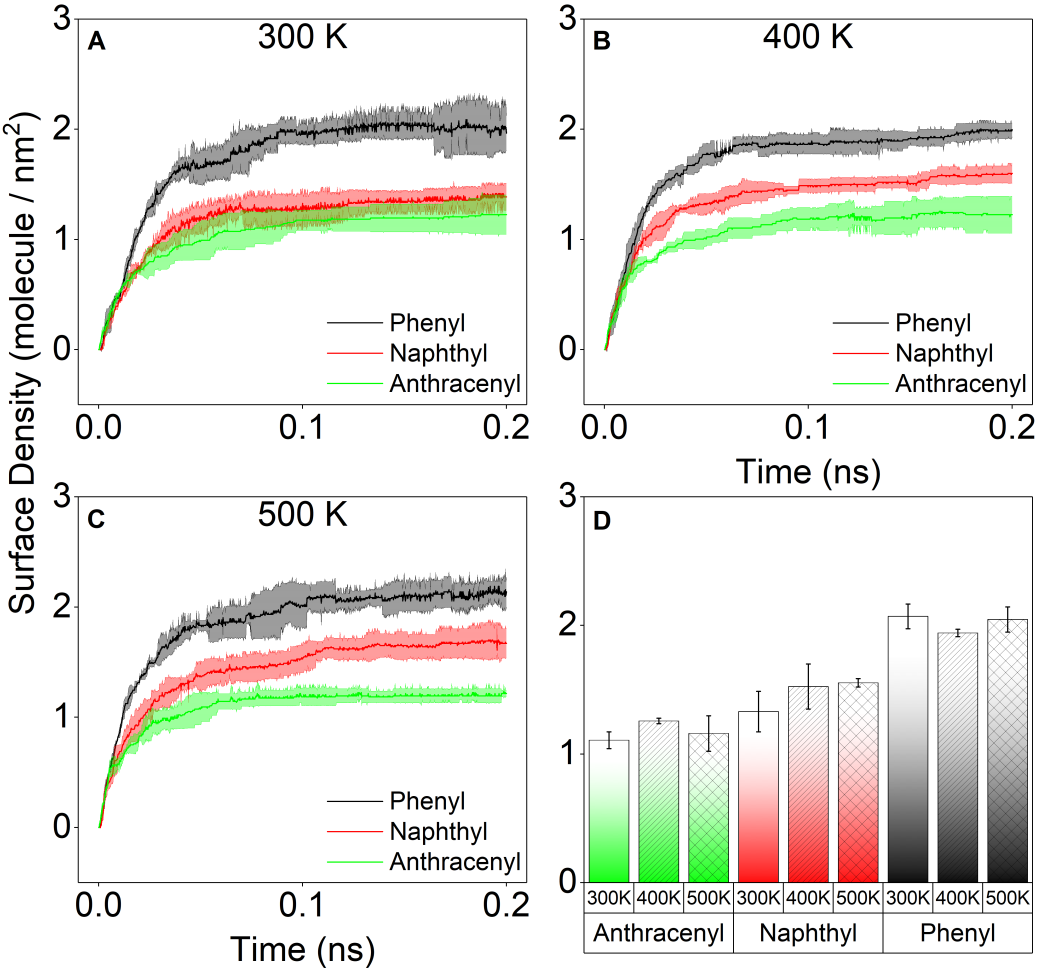


Figure 4.5: Time evolution of the surface density for phenyl, naphthyl, and anthracenyl chemisorbed on an amorphous silica surface from simulations at (A) 300, (B) 400, and (C) 500 K. For each data set, the dark line is the mean and the shaded region is the standard deviation of three independent simulations. (D) The steady-state surface density for each case is averaged over the last 0.1 ns of the simulations, where error bars reflect the standard deviation.

vector representations of the surface-bound silanols in the xy plane for representative simulations. The vector is defined from the positions of the two edge carbon atoms on the long axis of the silanol, as shown in the Fig. 4.8 insets. Note that the arrows point

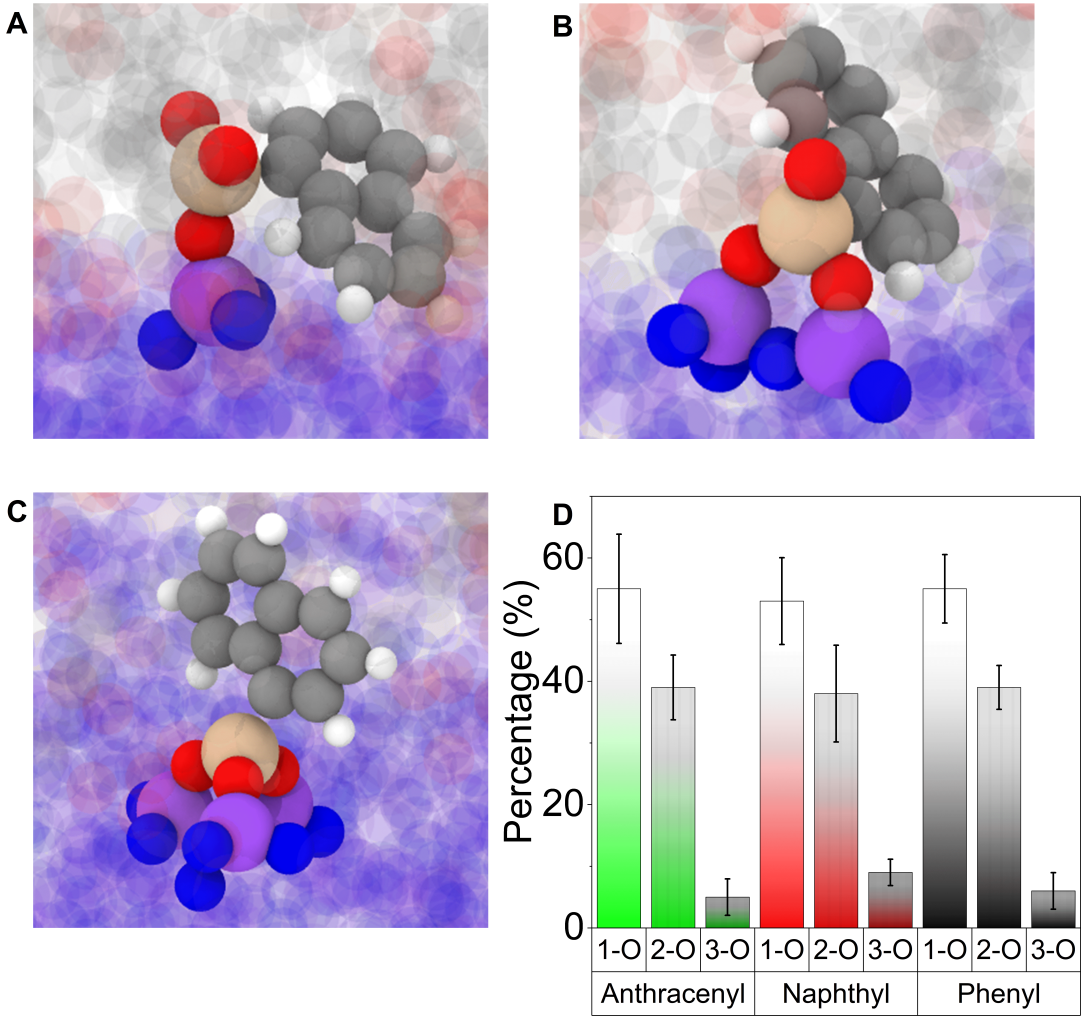


Figure 4.6: Close up snapshots of the three possible bonding configurations between a silanol and the silica substrate that differ based on the number of $Si_{silanol}$–O_{silica} bonds, shown using naphthyl as reference: (A) one bond (1-O), (B) two bonds (2-O), and (C) three bonds (3-O). Spheres representing atoms other than those in the representative silanols of interest are faded. (D) Distribution of the number of bonds between Si in the substrate and O in the silanol averaged over the three simulations at three temperatures for each silanol as a percentage of the total number of silanols in the system. The error bars represent the standard deviation.

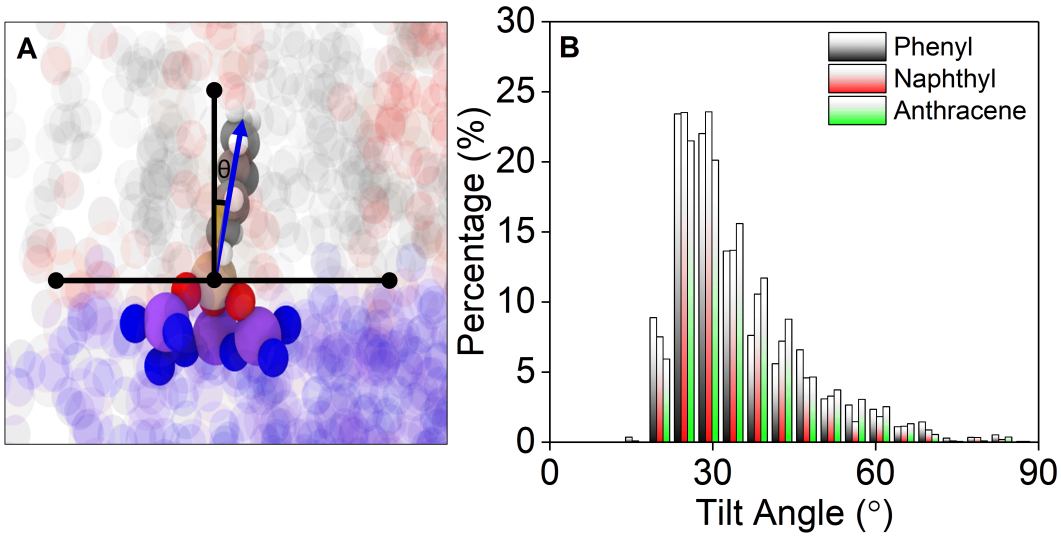


Figure 4.7: (A) Representative snapshot of phenyl showing the definition of the angle used to quantify the tilt of the silanol with respect to the surface-normal direction. Spheres representing atoms other than those in the representative silanol of interest are faded. (B) Distribution of tilt angles from all observed bonds and all temperatures/simulations between 0.1 and 0.2 ns of simulation time. Only slight differences between phenyl, naphthyl, and anthracenyl are observed, but smaller angles are preferred for the smaller silanols.

only one direction for naphthyl to reflect the asymmetry of that silanol. The vectors are colored based on their angle with respect to the x-axis; the x-axis is an arbitrary direction but, if the silanols are conformationally ordered, there will be more arrows in Fig. 4.8(A), (B) and (C) with similar colors. This qualitative analysis shows some evidence of local ordering, but clearly the silanols are not ordered into the closest packed configuration assumed in the geometric density calculations (Fig. 4.4). This may be correlated to the preferential 1-O bonding exhibited by all three silanols in Fig. 4.6(D), since fewer chemical bonds enable more flexibility and rotation ability.

Next, we quantified the local ordering using radial distribution functions (RDFs) [147] of the distance between Si atoms in the surface-bound silanols. The results for all simulations and temperatures are shown in Fig. 4.8(D), (E), and (F). If the silanols were ordered in their closest packed configuration, the smallest distance between silanols would be ≈0.3 nm. This is approximately where the first peak is seen in the RDFs in all three cases. However, there are also differences between the three silanols. Particularly, the

first peak is broadest and shortest for phenyl, indicating these silanols are the least conformationally ordered. Less conformational ordering is associated with larger available volume for conformational changes, consistent with the smaller tilt angles for phenyl in Fig. 4.7(B).

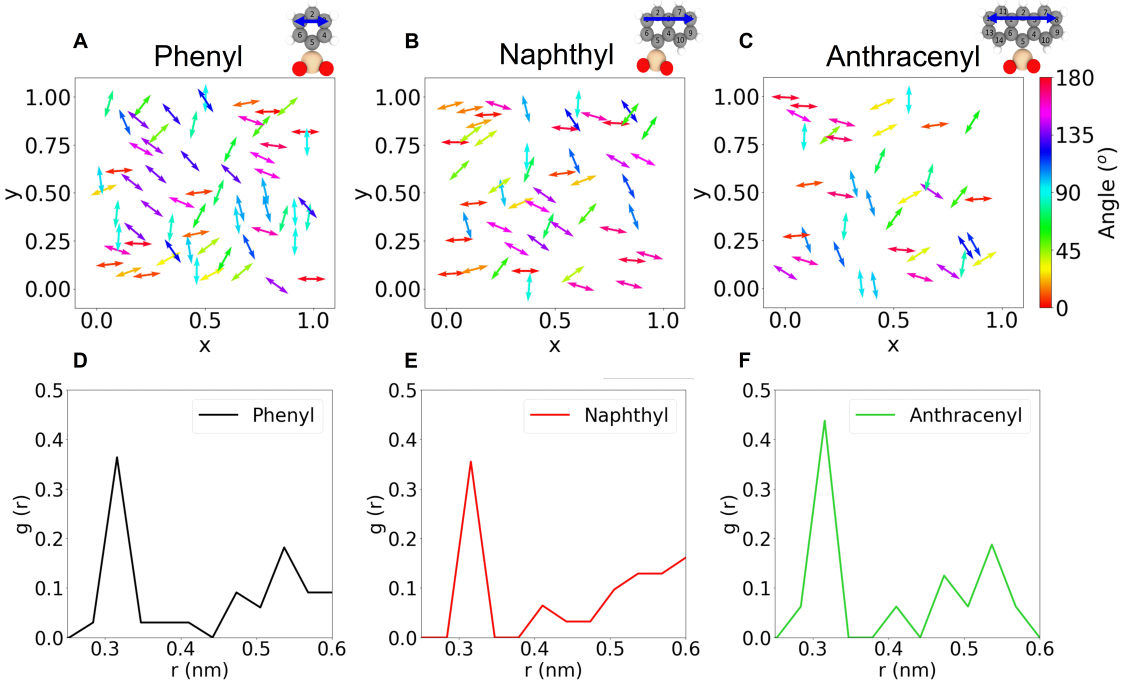


Figure 4.8: Two point vector representations of the silanol in the xy plane from representative simulations of (A) phenyl, (B) naphthyl, and (C) anthracenyl. The two point coordinates are taken from the edge carbons on the long axis of the silanol, as shown in the insets. The x- and y-axes are scaled by the total length of the simulation box in each direction. Radial distribution functions of the distance between Si atoms in (D) phenyl, (E) naphthyl, and (F) anthracenyl for all simulations.

The RDF peaks at farther distances reflect longer range ordering of the silanols. Interestingly, for phenyl and anthracenyl there are distinct peaks around 0.40, 0.47 and 0.55 nm, associated with preferred orientations of adjacent chemisorbed species. However, for naphthyl, the RDF peaks are broader and less distinct, indicating less long range order.

The naphthyl also had the least distinction between the different bonding configurations in Fig. 4.6(D) and the largest difference between the simulated and estimated surface densities in Table 4.1. The difference between naphthyl and the other two silanols is sym-

metry, with only naphthyl being asymmetric relative to the silicon atom. These results show that asymmetry decreases long-range order which, in turn, decreases the achievable surface density relative to the maximum possible value.

Finally, surface density may be affected by the interaction and bonding between silanols resulting in aggregates [148]. An example is shown in Fig. 4.9(A), where two naphthyl molecules associate via an oxygen bond. This behavior was analyzed for all three silanols by calculating the distributions of aggregate size (e.g. 1-silanol, 2-silanol, 3-silanol, etc.) during steady-state, as shown in Fig. 4.9(B).

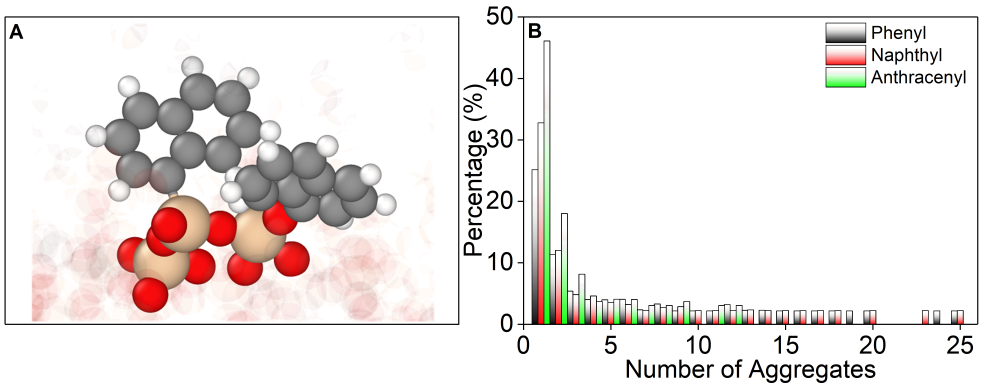


Figure 4.9: (A) Representative snapshot of a two-naphthl aggregate. (B) Distributions of aggregate size (quantified by number of bonded silanols) for each silanol calculated from trajectory data between 0.1 and 0.2 ns.

The most commonly observed configuration is 1 silanol, meaning not aggregated. However, all three molecules form multiple dimers and trimers as well as even larger aggregates. Comparing the three silanols, anthracenyl has the fewest and smallest aggregates, while the phenyl has the most and largest aggregates. Since the association reactions always occur via an Si-O-Si bond, the trend observed in the aggregation results can be associated with molecular size and surface density, where larger silanols are further apart and less likely to aggregate.

4.3.2 Acceleration of Diels-Alder Reactions by Mechanical Distortion

Having developed a surface functionalization procedure, Molecular dynamics (MD) simulations were implemented to validate and complement experimental results of com-

pressive molecular dynamics simulations. First, the anthracene monolayer deposition procedure was reproduced as shown in Fig. 4.10, and then capture pressure-driven interactions between maleimide dienophiles and the anthracene monolayer (Fig. 4.15).

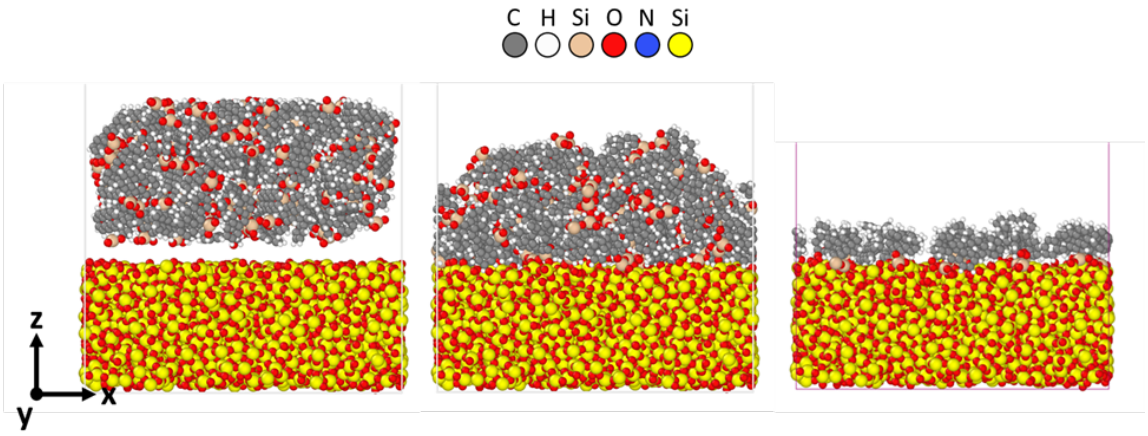


Figure 4.10: Side-view snapshots of the anthracene deposition simulation, from left to right, at in the initial configuration, after 300 ps of equilibration, and after removing all anthracene molecules not bonded to the surface.

Deposition simulations were run using the NVT ensemble [149] (constant number of particles, volume, and temperature) with initial system velocities given by a Gaussian distribution at 300, 350, and 400 K. The simulations were run for 300 ps. Snapshots of the model systems before and after the dynamic simulations are shown in Fig. 4.10. The number of covalent bonds between the diene molecules and the substrate was determined using the bond table available from ReaxFF. Area density was calculated from the number of anthracene molecules bonded with the substrate divided by the deposition area (≈32.9 nm^2). The evolution of the density with time at three different temperatures is shown in Fig. 4.11 (A), with representative perspective view snapshots of the simulations inset. The area density was calculated over the last 60 ps of the simulation and the results are shown in Fig. 4.11 (B). The average area density as the system nears steady state across all three temperatures is 1.20 ± 0.08 mol·nm^{-2}.

The reactions between the anthracene and SiO_2 were analyzed, and it was found that three different bonding scenarios were possible, depending on how many bonds formed with oxygen. Fig. 4.12 (A) shows the distribution of bonding configurations for the anthracene bonded to the surface in the 300 K simulation, with representative, close-up

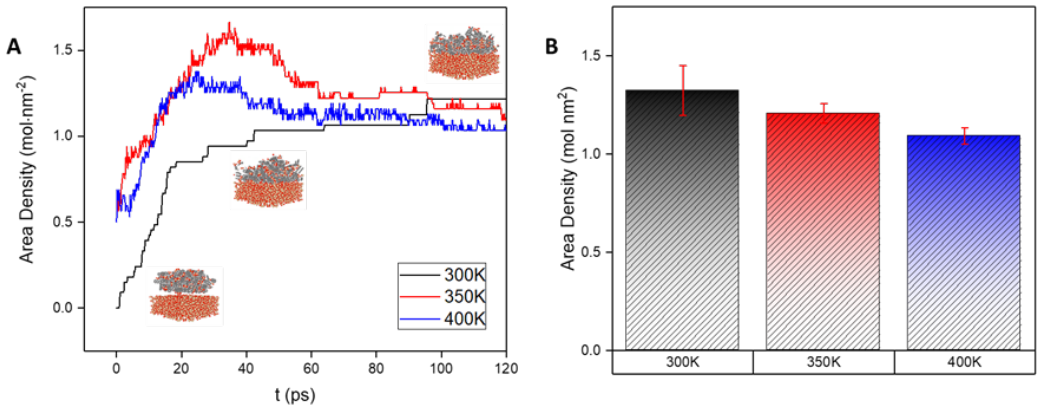


Figure 4.11: (A) Time evolution of the area density of anthracene molecules chemisorbed on the SiO_2 surface at 300, 350, and 400 K and (B) corresponding average steady-state density at each temperature, where error bars reflect the standard deviation of the data over the last 60 ps of the simulation. The average area density across all three temperatures as the system nears steady state is 1.20 ± 0.08 mol·nm^2. Error is reported as the standard deviation of the areal density at the three different temperatures.

snapshots of the three cases identified in Fig. 4.12 (B), (C), and (D). The most common bonding scenario was two oxygen atoms from the anthracene silane to form Si—O—Si bonds with the substrate, and the least was three oxygen atoms. Similar trends were observed at the other two temperatures.

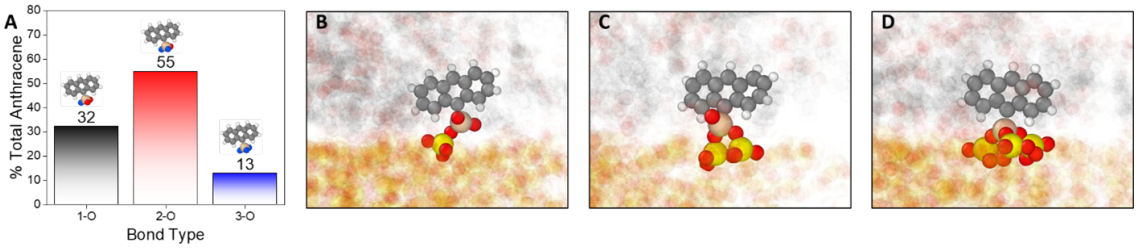


Figure 4.12: Analysis of bonding between anthracene and the SiO_2 substrate. (A) Distribution of number of number of bonds between Si in the anthracene and O on the substrate. The most common coIormation is two oxygen bonds (2-O). Close up snapshots of the three possible bonding configurations: (B) 1-O, (C) 2-O, and (D) 3-O.

One point for validating our deposition simulations was comparing theoretical molec-

ular distances of the expected monolayers to experimental data.

For that we determined the mean spacing between anthracene molecules before the reaction, and between each adduct after the reaction, from the molecular dimensions of the molecules and the surface density data obtained from the QCM experiments as shown in Fig. 4.13. For simplicity, we treated the anthracene molecules as square boxes with 0.73 nm × 0.73 nm dimensions, which theoretically would be the 0.53 nm^2 area for 1 anthracene molecule. This is a reasonable estimate if we assume the molecules are randomly packed and with random in-plane orientation. From QCM data we calculated the actual area for 1 anthracene = 0.89 nm^2, which provides minimum 0.94 nm^2 center-to-center space between each anthracene molecules. (1 nm^2 / 1.12 molecule = 0.89 nm^2 or 0.94 nm × 0.94 nm). In a similar way, the center-to-center space distance between 2 adduct molecules were found to be 10.3 Å.

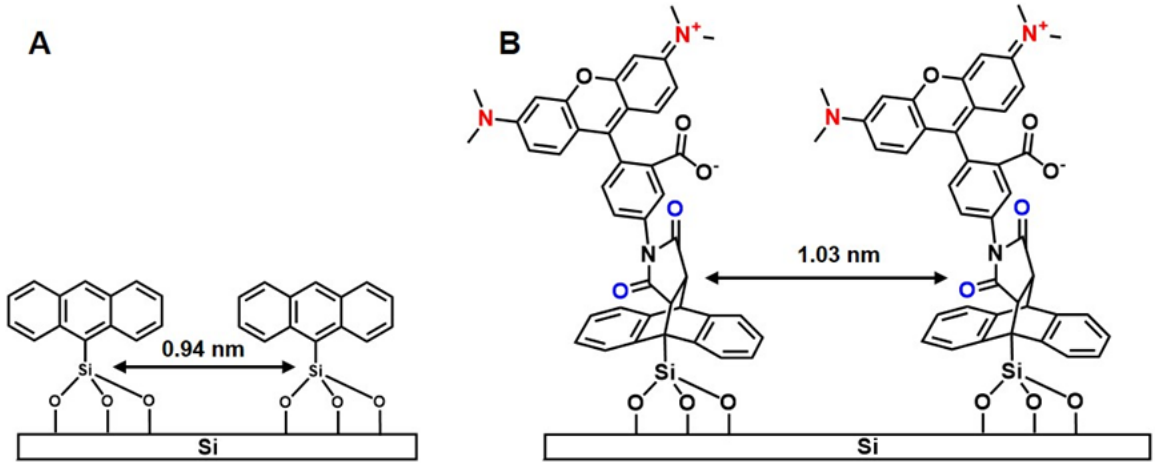


Figure 4.13: Calculation of molecular spacing for (A) anthracene monolayer and (B) Diels-Alder adduct.

Molecular dynamics (MD) simulations were run to model anthracene monolayer deposition on the surface of an amorphous SiO_2 substrate and to find center-to-center distance between surface anchored 9-anthracenyltrimethoxysilane molecules as shown in Fig. 4.14.

The response of the anthracene to compression was tracked in terms of the change in configuration of the atoms. Representative snapshots of anthracene molecules at the low (1.7 GPa) and high (3.0 GPa) pressure cases are shown in Fig. 4.16 (B) and (C). Two key obsevations can be made. To quantify the configurational response of the molecules to pressure, the angle of the plane of the carbon rings in each molecule with respect to the

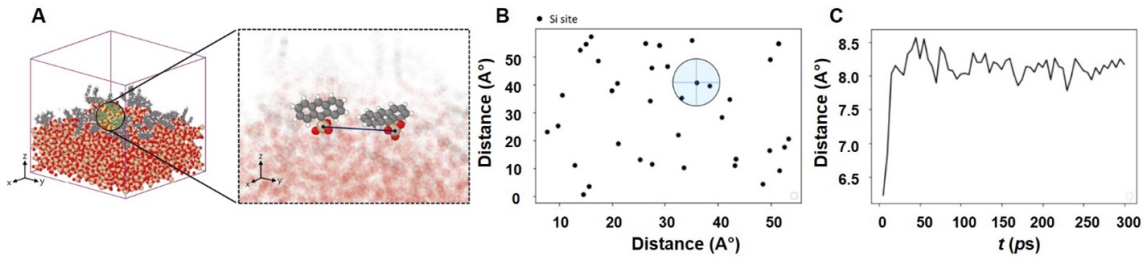


Figure 4.14: Calculation of molecular spacing from (A) Molecular Dynamics simulations of 9−anthracenyltrimethoxysilane molecules chemisorbed on to SiO_2 substrate. The pair-wise distances for Si atoms was calculated for (B) the closest neighbors within 12 Å cut−off−radius from the reference Si atom and (C) averaged over time once equilibrium had been reached at around 200 ps.

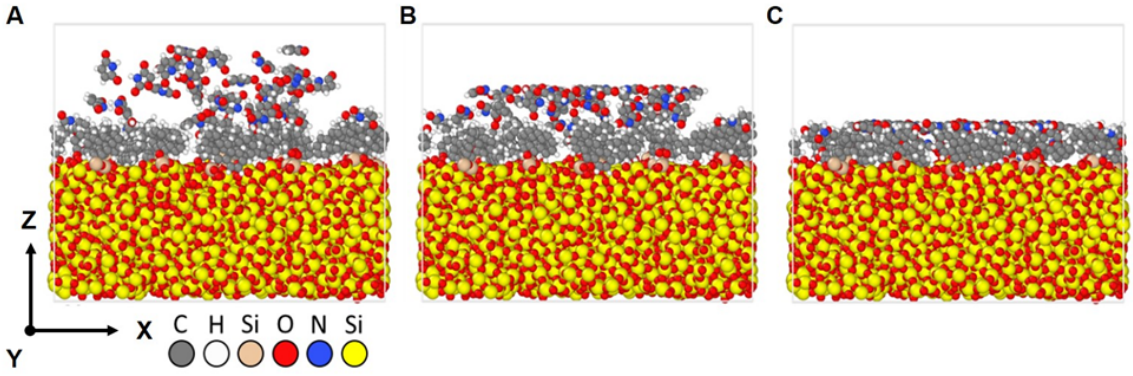


Figure 4.15: Snapshots of simulations of compression-driven bonding between maleimide and anthracene monolayers, (A) before applying pressure, (B) at 1.7 GPa, and (C) at 3.0 GPa.

plane of the surface was calculated. As shown in Fig. 4.16 (A), the angle depends on both pressure and the bonding configuration. Specifically, the angle decreases with pressure, with the molecules farther from vertical (plane of the rings normal to the SiO_2 substrate) at the higher pressure. Also, the angle is smaller for molecules with only one bond to the surface, consistent with bond angle deflection being less constrained when fewer bonds are present. Recall from Fig. 4.12 (A) that the most common configuration is 2-O, so the angles shown for that case are the most likely to be observed in the simulation.

The deflection of the molecule is important because it affects the alignment of force along the reaction pathway. For the external force to drive this reaction, it should act in

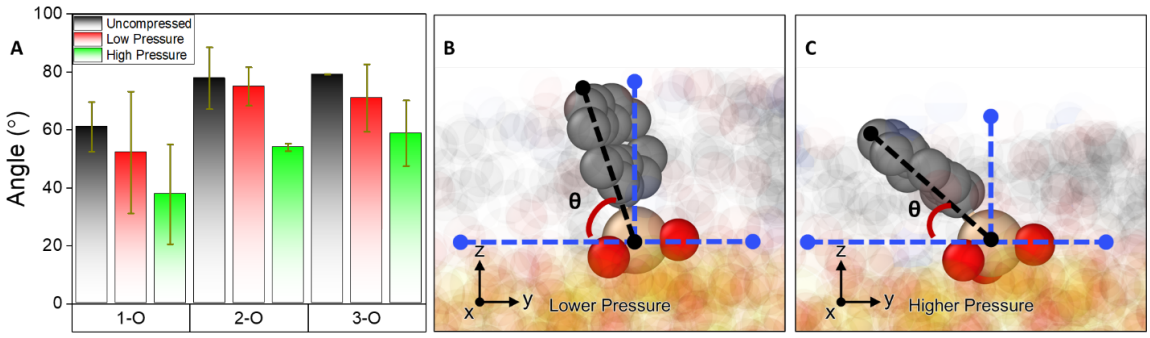


Figure 4.16: (A) Distribution of bending angle in response to applied pressure in the simulations and representative snapshots of the molecule with the bending angle defined at (B) low and (C) high pressures. Compression causes the molecule to bend towards the surface. Error bars are reported as one standard deviation from the mean of three independent calculations.

the direction normal to the plane of the rings. The simulations show that, for the most common bonding configuration (2-O), the equilibrium (zero applied pressure) angle is only about 80 °, i.e., the molecules are nearly vertical. Compression moves the molecules away from this configuration towards the horizontal orientation. The more the molecule bends, the more of the applied force acts along the reaction coordinate. Using the average angles in Fig. 4.16 (A) and the assumption that the force exerted by the wall is evenly distributed across the molecules, the force distribution per molecule was calculated, using the relation $F_N = F_z \cos\theta$ as shown in Fig. 4.17, where F_N is force applied along the reaction coordinate (normal to the plane of the anthracene rings), and F_z is force applied by the tip normal to the SiO_2 surface. The force per molecule is largest at the highest pressure and for the 1-O case where the molecule as the most flexibility to bend towards the horizontal configuration. Table 4.2 summarizes the observed results in Fig. 4.16 (A) and Fig. 4.17 (A).

Error bars are reported as one standard deviation from the mean of three independent calculations.

In addition to bending of the entire molecule in response to compression, the force causes deformation of the bonds and bond angles within the molecule. Based on the findings from DFT completed byt our collaborators, we characterized the distribution

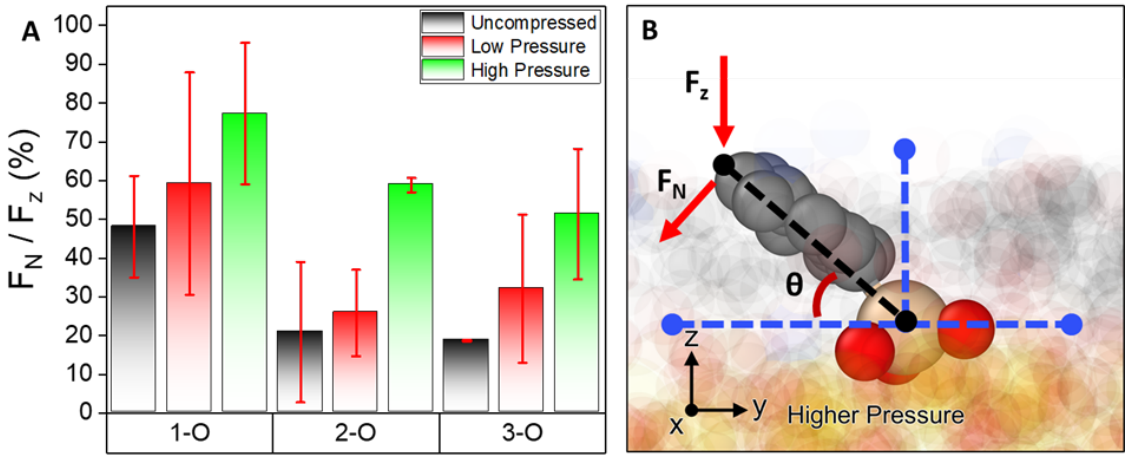


Figure 4.17: (A) Distribution of force acting in the direction normal to the anthracene rings at equilibrium and in the low- and high-pressure cases. Error bars are reported as one standard deviation from the mean of three independent calculations. (B) Only part of the applied force, F_z, acts in the direction normal to the plane of the rings, F_N, and is approximated from the angle of the molecule with respect to the direction normal to the SiO_2 surface as $F_N = F_z \cos\theta$.

Pressure	Bond Type	$\theta(^\circ)$	F_N/F_z
None	1-O	61.1 ± 8.6	48.1 ± 13.1
-	2-O	77.8 ± 10.7	20.9 ± 18.2
-	3-O	79.2 ± 0.1	18.7 ± 18.1
Low	1-O	52.3 ± 21.0	59.2 ± 28.7
-	2-O	74.9 ± 6.6	25.8 ± 11.2
-	3-O	71.1 ± 11.6	32.1 ± 19.1
High	1-O	37.8 ± 17.2	77.3 ± 18.3
-	2-O	53.9 ± 1.3	58.9 ± 1.86
-	3-O	58.8 ± 11.3	51.3 ± 16.8

Table 4.2: Bending angle, θ, and percentage of applied force, Fn/Fz, for different pressures and oxygen bond configurations.

of CCH angles in all molecules without compression and at the low- and high- pressure cases in the simulations. As shown in Fig. 4.18. The average CCH angles for each case are identified as dashed vertical lines and show that this angle deviates more from its equilibrium value (the average value from the simulation without compression, shown as the black dashed line) with increasing pressure. However, the distributions also shift towards the left with increasing pressure, indicating there are more molecules with CCH angles further from equilibrium at higher pressure.

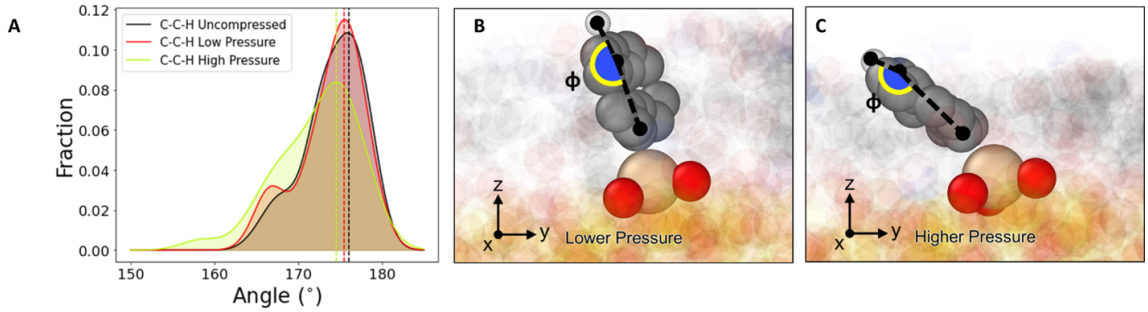


Figure 4.18: (A) Distribution of CCH angles for all molecules during the simulations. The average angle (dashed vertical lines) shift slightly left (away from the equilibrium, uncompressed value) with pressure, but the fraction of molecules with far-from-equilibrium angles increases with pressure. Representative snapshots of the anthracene during the compression simulations at (A) low and (B) high pressure with the CCH angle identified.

4.4 Conclusions

Reactive simulations were used to study the covalent functionalization of amorphous silica with silanol aromatic hydrocarbons. Surface density increased with decreasing molecular size, consistent with the maximum densities estimated from molecule geometry in a closest-packed configuration. The simulation densities were smaller than the estimated maximum values and the biggest difference between simulation and estimation was observed for naphthyl. Three possible chemical bonding configurations were observed and it was shown that all three silanols preferentially formed fewer covalent bonds, facilitating bending or rotation. Tilt angles were also calculated and shown to be smaller for smaller molecules. Local conformational ordering, analyzed qualitatively and quantitatively, was found to increase with molecule size. However, the least long-range order

was exhibited by the asymmetric naphthyl silanol, a result that was correlated to the larger difference between the simulation and estimated surface density. Finally, analysis of aggregation of surface-bound species showed that smaller size and higher density were also associated with the formation of more and larger aggregates. These result show that both size and symmetry affect the surface density achievable in covalent functionalization of surfaces with silanol aromatic hydrocarbons. These simulation-based approaches can inform our understanding how molecular structure affects surface density which can guide the selection or design of molecules to achieve an ideal surface density and, in turn, ideal properties, for a specific surface or application.

Next, MD simulations were used to validate the surface density of anthracenyl molecules on a functionalized surface. Calculations showed that the anthracene molecules chemisorb onto the SiO_2 substrate, forming a stable monolayer with an average area density of $1.20 \pm 0.08\ mol\ \cdot\ nm^{-2}$ across temperatures of 300, 350, and 400 K. The simulations revealed that the most common bonding scenario involved two oxygen atoms from the anthracene silane forming Si—O—Si bonds with the substrate.

Furthermore, the mean spacing between anthracene molecules before the reaction and between each adduct after the reaction were consistent with experimental data, validating the deposition simulations.

Compression simulations showed that Diels-Alder reactions are accelerated under mechanical distortion. The anthracene molecules respond to tip-induced compression by bending towards the surface, with the bending angle decreasing as pressure increases. The fraction of molecules with distorted CCH angles also increases with higher pressure, indicating significant deformation. This deformation aligns the force more effectively along the reaction coordinate, enhancing the reaction rate. The distribution of force acting in the direction normal to the anthracene rings increases with pressure, especially for molecules with fewer bonds to the surface.

Overall, the simulations provided insights into the behavior of anthracene monolayers under compression and the acceleration of Diels-Alder reactions. The findings suggest that mechanical distortion can be an effective means of enhancing reaction rates, with potential applications in material science and surface chemistry.

Chapter 5

Summary and Future Work

5.1 Summary

This dissertation research was directed towards studying the chemical processes occurring on surfaces, with a focus on the growth of surface layers for applications in friction reduction and surface functionalization to enable the investigation of mechanically driven chemical reactions.

Initially addressing the question of how the coating life of MoS_2 is affected when doped with Ni, we conducted an experimental study evaluating sputtered undoped and 7% Ni-doped by weight Dry Film Lubricants (DFLs). The short and long test procedures provided evidence that, at low contact pressures, Ni-doping improves the wear life of MoS_2 DFL. Furthermore, the origin of this improvement was investigated via SEM analysis and associated with the larger size of detached MoS_2 debris or flakes found in the wear track. Similarly, it was proposed that the wear life of MoS_2 coatings cannot be correlated to wear depth but instead to the size of lubricious wear particles that can lubricate the wear track during shear. Summarizing the results, a model was prepared to show the differences between Ni-doped and undoped MoS_2 wear processes. However, to further understand the role of the Ni-dopant in enabling the formation of larger lubricious wear particles, insight into the sputtering process and resulting DFL microstructure was needed.

As mentioned in Chapter 2, the need for an atomic-level method to evaluate the formation of Ni-doped and undoped MoS_2 DFL led to the development of a novel reactive molecular dynamics potential. In Chapter 3, we evaluated a new ReaxFF potential parameterized to match DFT-calculations energies of Mo-substituted, S-substituted, oc-

tahedral, and tetrahedral intercalation structures of the Ni-dopant. To demonstrate its applicability, a sputtering deposition procedure was implemented to grow MoS_2 DFL using molecular dynamics simulations. The sputtered Ni-doped and undoped films were annealed and fast quenched to evaluate the crystallization process. Radial distribution functions showed the transition from amorphous to crystal, with atom-pair distances showing peaks at expected locations for MoS_2 crystals.

With the Mo/S/Ni ReaxFF potential available, we implemented the sputtering deposition procedure to generate films with different Ni concentrations. The sputtered films were characterized by evaluating density, crystallinity, radial distribution function, and Ni-cluster formations. The key findings were that the highest density and crystallinity were observed just above the MoS_2 substrate, irrespective of Ni concentration or temperature. Ni formed clusters of varying sizes, with larger clusters at higher concentrations. Temperature differences caused minimal changes in nanostructure, except for slight increases in long-range ordering of Mo and Ni atoms.

Analogous to the experimental work done in Chapter 2, the sputtered MoS_2 films were compressed and sheared in simulations. Shearing simulations showed that films with 2% and 10% Ni had lower shear stress at steady state compared to those with 0% and 15% Ni, due to the formation of lubricious wear particles with a crystalline core and amorphous, Ni-containing surfaces. This structure was unique to intermediate Ni concentrations. These findings highlight the non-monotonic dependence of tribological properties on Ni concentration, providing insights for optimizing dopant levels in future experiments. The modeling approach developed here can also be used to investigate other dopants, enhancing material performance further.

In Chapter 4, we explored the work done on understanding the covalent functionalization of amorphous silica with aromatic hydrocarbons. Simulations showed that the surface density of silanol-terminated phenyl, naphthyl, and anthracenyl molecules is lower than the maximum value calculated based on molecule geometry, and the simulation densities decrease faster with the number of aromatic rings than the geometric densities. The trends were analyzed in terms of the surface–silanol bonding configurations, tilt angles, local conformational ordering, and aggregation of surface-bound molecules under steady-state conditions. Results showed that the surface density is affected by both the size and symmetry of the aromatic hydrocarbons. We then simulated compression to provide some

insight into how immobilized aromatic hydrocarbons deform under compression during mechanochemical processes. Guided by experimental observations, these simulation-based approaches correlate with our comprehension of how molecular structure influences surface density, which can direct the choice or creation of molecules to attain an optimal surface density and potentially be used for on-surface mechanochemistry.

5.2 Future Work

A significant insight the chemical processes occurring on surfaces was presented in this body of work. However, there remain open questions and opportunities to expand how simulations guide the design and conception of new materials and chemistries.

5.2.1 Modeling MoS_2 DFLs

Sputtering deposition has shown that the Ni concentration in MoS_2 affects the microstructure and tribological properties of the simulated DFLs. To further explore this, it is important to expand the investigation to include more of the variables that might influence the microstructure formation of MoS_2 DFL, such as substrates and other dopants. Substrates play a crucial role in templating the structure of films. Carbon structures and other metal substrates would be of great interest to broaden our understanding of the parameters influencing the microstructural formation of sputtered films. It is also important to explore other dopants that are used in MoS_2 DFLs, including Ti and Sb_2O_3, that may provide better lubrication properties under a wider range of operating conditions. To achieve this, the current version of the Mo/S/Ni force field can be further improved by parameterization for new potential substrate materials and MoS_2 dopants. Moreover, investigating the influence of deposition and sliding speeds is essential, as these rates are significantly higher in simulations compared to experiments. Understanding and characterizing these effects will allow us to better correlate simulation outcomes with experimental observations. This alignment will enable a more accurate interpretation of how rapid simulation conditions translate to the slower, more controlled experimental settings, thereby enhancing our comprehension of the microstructural evolution and performance of MoS_2 DFLs across different deposition and operational scenarios.

5.2.2 Surface Mechanochemistry

There are also opportunities to build upon the work reported in Chapter 4. Firstly, one critical area for further investigation is the influence of molecular orientation and packing on mechanochemical reactions. Our simulations have indicated that the arrangement and density of surface-bound molecules can significantly impact their reactivity. Future computational studies should focus on exploring various substrate surface treatments to control molecular alignment and examining how different packing densities and orientations influence mechanochemical pathways. Secondly, understanding the role of environmental factors such as temperature, pressure, and solvent interactions on mechanochemical reactions is vital. These factors can dramatically affect reaction kinetics and product distributions. Future computational studies should incorporate varying environmental conditions to develop a more comprehensive understanding of their effects on surface mechanochemistry. This includes simulating different solvent environments to assess their impact on the stability and reactivity of immobilized molecules. Another critical gap lies in the scalability of mechanochemical reactions for practical applications. While our simulations provide valuable insights at the nanoscale, translating these findings to macroscale applications requires understanding the collective behavior of many interacting molecules. Developing multiscale modeling approaches that bridge atomistic simulations with continuum-scale models (e.g., Finite element method coupled with chemical reactions) could predict the performance of mechanochemical systems in real-world conditions.

5.2.3 Simulation Timescales

In both simulation studies reported in this dissertation, there remains a limitation related to time scale. The small time steps needed to probe the motion of the molecules – typically in the range of femtoseconds – limit the length of a simulations and therefore the number of possible observable molecule interactions within the simulation duration. For example, experimentally relevant sputtering deposition film growth rates are in the nm/sec range [97] which is orders of magnitude slower than the growth rates possible with MD simulations which typically do not exceed several nm/ns. Going forward, to partially address this issue, deposition parameters can be re-scaled to accelerate the MD simulations. One such scaling method is adjusting the deposition rates of the depositing incident atoms to allow for energy relaxation. For instance, if the deposition intervals are

too short, one can run into issues of unphysical temperature increase [123]. Alternatively, if the deposition intervals are long, it will take longer than nanoseconds to achieve a cluster formation. Another approach is to introduce thermostats that can account for frictional and random forces experienced by the depositing atoms which will increase the (picosecond) energy relaxation times between deposition cycles. It is important to stress that the re-scaling process will still result in simulations of film formation at deposition rates orders of magnitude faster than those used experimentally. Therefore, it is important to confirm the physical realism of the simulations by performing comparisons between experimental and MD simulation trends.

5.3 Concluding Remarks

In summary, this research has advanced our understanding of the interplay between dopant concentration, microstructure, and tribological performance in MoS_2 DFLs. It has also established a robust framework for using molecular dynamics simulations and ReaxFF potentials to study surface chemical processes. The study of immobilized AH has provided crucial insights into how to design material systems to study mechanically driven chemical reactions.

These findings collectively open new avenues for the design and optimization of materials for friction reduction, surface functionalization, and mechanochemistry. By integrating the mechanistic insights gained from both the MoS_2 DFLs and immobilized AH systems, we are better equipped to develop ReaxFF potentials tailored for reactions and other surface chemistry applications under mechanical stress.

This integrated approach paves the way for future advancements in surface chemistry and materials science, offering a comprehensive understanding that can drive innovative solutions in these fields.

Bibliography

(1) Radisavljevic, B.; Radenovic, A.; Brivio, J.; Giacometti, V.; Kis, A. *Nat. Nanotechnol.* **2011**, *6*, 147–150.

(2) Gregoritza, M.; Brandl, F. P. *Eur. J. Pharm. Biopharm.* **2015**, *97*, 438–453.

(3) Vazirisereshk, M. R.; Martini, A.; Strubbe, D. A.; Baykara, M. Z. *Lubricants* **2019**, *7*, 57.

(4) Hinnemann, B.; Moses, P. G.; Bonde, J.; Jørgensen, K. P.; Nielsen, J. H.; Horch, S.; Chorkendorff, I.; Nørskov, J. K. *J. Am. Chem. Soc.* **2005**, *127*, 5308–5309.

(5) Vazirisereshk, M. R.; Ye, H.; Ye, Z.; Otero-de-la-Roza, A.; Zhao, M.-Q.; Gao, Z.; Johnson, A. T. C.; Johnson, E. R.; Carpick, R. W.; Martini, A. *Nano Lett.* **2019**, *19*, 5496–5505.

(6) Vazirisereshk, M. R.; Hasz, K.; Carpick, R. W.; Martini, A. *J. Phys. Chem. Lett.* **2020**, *11*, 6900–6906.

(7) Vellore, A.; Romero Garcia, S.; Johnson, D. A.; Martini, A. *Tribol. Lett.* **2021**, *69*, 10.

(8) Killeffer, D. H.; Linz, A. *Soil Science* **1953**, *75*, 83.

(9) Conley, P., *Space vehicle mechanisms: Elements of successful design*; Conley, P. L., Ed.; John Wiley & Sons: Nashville, TN, 1998.

(10) Donnet, C.; Erdemir, A. *Surf. Coat. Technol.* **2004**, *180-181*, 76–84.

(11) Sun, X. In *Encyclopedia of Tribology*, Wang, Q. J., Chung, Y.-W., Eds.; Springer US: Boston, MA, 2013, pp 3165–3172.

(12) Zabinski, J. S.; Donley, M. S.; Walck, S. D.; Schneider, T. R.; Mcdevitt, N. T. *Tribol. Trans.* **1995**, *38*, 894–904.

(13) Simmonds, M. C.; Savan, A.; Pflüger, E.; Van Swygenhoven, H. *Surface and Coatings Technology* **2000**, *126*, 15–24.

(14) Nainaparampil, J. J.; Phani, A. R.; Krzanowski, J. E.; Zabinski, J. S. *Surf. Coat. Tech.* **2004**, *187*, 326–335.

(15) Renevier, N. M.; Fox, V. C.; Teer, D. G.; Hampshire, J. *Surf. Coat. Tech.* **2000**, *127*, 24–37.

(16) Teer, D. G. *Wear* **2001**, *251*, 1068–1074.

(17) Tedstone, A. A.; Lewis, D. J.; O'Brien, P. *Chem. Mater.* **2016**, *28*, 1965–1974.

(18) Ye, M.; Zhang, G.; Ba, Y.; Wang, T.; Wang, X.; Liu, Z. *Appl. Surf. Sci.* **2016**, *367*, 140–146.

(19) Stoyanov, P.; Chromik, R. R.; Goldbaum, D.; Lince, J. R.; Zhang, X. *Tribol. Lett.* **2010**, *40*, 199–211.

(20) Paul, A.; Singh, H.; Mutyala, K. C.; Doll, G. L. In *44th Aerospace Mechanisms Symposium*, 2018, p 141.

(21) Li, H.; Li, X.; Zhang, G.; Wang, L.; Wu, G. *Tribol. Lett.* **2017**, *65*, 38.

(22) Lince, J. R. In *Encyclopedia of Tribology*; Springer US: Boston, MA, 2013, pp 782–785.

(23) Hamilton, M. A.; Alvarez, L. A.; Mauntler, N. A.; Argibay, N.; Colbert, R.; Burris, D. L.; Muratore, C.; Voevodin, A. A.; Perry, S. S.; Sawyer, W. G. *Tribol. Lett.* **2008**, *32*, 91–98.

(24) Stupp, B. C. *Thin Solid Films* **1981**, *84*, 257–266.

(25) Gupta, D.; Chauhan, V.; Kumar, R. *Inorg. Chem. Commun.* **2020**, *121*, 108200.

(26) Gao, M.-R.; Chan, M. K. Y.; Sun, Y. *Nat. Commun.* **2015**, *6*, 7493.

(27) Kaindl, R.; Bayer, B. C.; Resel, R.; Müller, T.; Skakalova, V.; Habler, G.; Abart, R.; Cherevan, A. S.; Eder, D.; Blatter, M.; Fischer, F.; Meyer, J. C.; Polyushkin, D. K.; Waldhauser, W. *Beilstein J. Nanotechnol.* **2017**, *8*, 1115–1126.

(28) Ostadhossein, A.; Rahnamoun, A.; Wang, Y.; Zhao, P.; Zhang, S.; Crespi, V. H.; van Duin, A. C. *The journal of physical chemistry letters* **2017**, *8*, 631–640.

(29) Ponomarev, I.; Polcar, T.; Nicolini, P. *The Journal of Physical Chemistry C* **2022**, *126*, 9475–9481.

(30) Mohammadtabar, K.; Guerrero, E.; Romero Garcia, S.; Shin, Y. K.; van Duin, A. C. T.; Strubbe, D. A.; Martini, A. *J. Phys. Chem. C Nanomater. Interfaces* **2023**, *127*, 12171–12183.

(31) Chen, R.; Jusufi, A.; Schilowitz, A.; Martini, A. *J. Vac. Sci. Technol. A* **2020**, *38*, 022201.

(32) Chen, R.; Konicek, A. R.; Jusufi, A.; Kliewer, C. E.; Jaishankar, A.; Schilowitz, A.; Martini, A. *J. Phys. Chem. C Nanomater. Interfaces* **2020**, *124*, 27571–27579.

(33) Taguchi, M.; Hamaguchi, S. *Thin Solid Films* **2007**, *515*, 4879–4882.

(34) Abraham, J. W.; Strunskus, T.; Faupel, F.; Bonitz, M. *J. Appl. Phys.* **2016**, *119*, 185301.

(35) Taguchi, M.; Hamaguchi, S. *J. Appl. Phys.* **2006**, *100*, 123305.

(36) Gorokh, A. A.; Grigoriev, F. V.; Katkova, E. V.; Sulimov, A. V.; Sharapova, S. A. *Moscow Univ. Phys. Bull.* **2016**, *71*, 114–117.

(37) Grigoriev, F. V. *Moscow Univ. Phys. Bull.* **2015**, *70*, 521–526.

(38) Barth, J. V.; Costantini, G.; Kern, K. *Nature* **2005**, *437*, 671–679.

(39) Sui, T.; Song, B.; Wen, Y.-H.; Zhang, F. *Sci. Rep.* **2016**, *6*, 22696.

(40) Zhang, S.; Niu, H.; Zhang, Y.; Liu, J.; Shi, Y.; Zhang, X.; Cai, Y. *Journal of chromatography. A* **2012**, *1238*, 38–45.

(41) Filler, M. A.; Bent, S. F. *Prog. Surf. Sci.* **2003**, *73*, 1–56.

(42) Berman, D.; Krim, J. *Prog. Surf. Sci.* **2013**, *88*, 171–211.

(43) Lai, C.-Y.; Trewyn, B. G.; Jeftinija, D. M.; Jeftinija, K.; Xu, S.; Jeftinija, S.; Lin, V. S.-Y. *J. Am. Chem. Soc.* **2003**, *125*, 4451–4459.

(44) Corno, M.; Delle Piane, M.; Choquet, P.; Ugliengo, P. *Phys. Chem. Chem. Phys.* **2017**, *19*, 7793–7806.

(45) Ilyas, A.; Odatsu, T.; Shah, A.; Monte, F.; Kim, H. K. W.; Kramer, P.; Aswath, P. B.; Varanasi, V. G. *Adv. Healthc. Mater.* **2016**, *5*, 2199–2213.

(46) Sayed, E.; Haj-Ahmad, R.; Ruparelia, K.; Arshad, M. S.; Chang, M. W.; Ahmad, Z. *AAPS PharmSciTech* **2017**, *18*, 1507–1525.

(47) Valles, D. J.; Zholdassov, Y. S.; Korpanty, J.; Uddin, S.; Naeem, Y.; Mootoo, D. R.; Gianneschi, N. C.; Braunschweig, A. B. *Angew. Chem. Int. Ed Engl.* **2021**, *60*, 20350–20357.

(48) Zholdassov, Y. S.; Valles, D. J.; Uddin, S.; Korpanty, J.; Gianneschi, N. C.; Braunschweig, A. B. *Advanced materials (Deerfield Beach, Fla.)* **2021**, *33*, e2100803.

(49) Rimola, A.; Costa, D.; Sodupe, M.; Lambert, J.-F.; Ugliengo, P. *Chem. Rev.* **2013**, *113*, 4216–4313.

(50) Sulkanen, A. R.; Sung, J.; Robb, M. J.; Moore, J. S.; Sottos, N. R.; Liu, G.-Y. *J. Am. Chem. Soc.* **2019**, *141*, 4080–4085.

(51) Tao, F.; Bernasek, S. L., *Functionalization of Semiconductor Surfaces: Tao/semiconductor surfaces*; Tao, F. (, Bernasek, S. L., Eds.; Wiley-Blackwell: Hoboken, NJ, 2012.

(52) Veerbeek, J.; Huskens, J. *Small Methods* **2017**, *1*, 1700072.

(53) Hong, Y.; Chen, W.; Fang, H.; Zuo, B.; Yuan, Y.; Zhang, L.; Wang, X. *J. Phys. Chem. C Nanomater. Interfaces* **2019**, *123*, 19715–19724.

(54) Bowal, K.; Pascazio, L.; Wang, H.; Chen, D.; Kraft, M. *Proc. Combust. Inst.* **2021**, *38*, 1115–1123.

(55) Diaz, L.; Liauw, C. M.; Edge, M.; Allen, N. S.; McMahon, A.; Rhodes, N. *J. Colloid Interface Sci.* **2005**, *287*, 379–387.

(56) Stålgren, J. J. R.; Eriksson, J.; Boschkova, K. *J. Colloid Interface Sci.* **2002**, *253*, 190–195.

(57) Sauerbrey, G. *Zeitschrift für Physik* **1959**, *155*, 206–222.

(58) Diels, O.; Alder, K. *Justus Liebigs Ann. Chem.* **1928**, *460*, 98–122.

(59) Andersen, J. M.; Mack, J. *Chem. Sci.* **2017**, *8*, 5447–5453.

(60) Bachmann, T.; Rychlik, M. *Molecules* **2018**, *23*, 2117.

(61) Kahn, S. D.; Pau, C. F.; Overman, L. E.; Hehre, W. J. *J. Am. Chem. Soc.* **1986**, *108*, 7381–7396.

(62) Leftwich, T. R.; Madachik, M. R.; Teplyakov, A. V. *J. Am. Chem. Soc.* **2008**, *130*, 16216–16223.

(63) Van Duin, A. C. T.; Dasgupta, S.; Lorant, F.; Goddard, W. A. *J. Phys. Chem. A* **2001**, *105*, 9396–9409.

(64) Han, Y.; Jiang, D.; Zhang, J.; Li, W.; Gan, Z.; Gu, J. *Front. Chem. Sci. Eng.* **2016**, *10*, 16–38.

(65) Black, J. E.; Iacovella, C. R.; Cummings, P. T.; McCabe, C. *Langmuir* **2015**, *31*, 3086–3093.

(66) Bhuiyan, F. H.; Kim, S. H.; Martini, A. *Appl. Surf. Sci.* **2022**, *591*, 153209.

(67) Bhuiyan, F. H.; Li, Y.-S.; Kim, S. H.; Martini, A. *Faraday Discuss.* **2023**, *241*, 194–205.

(68) Soria, F. A.; Zhang, W.; Paredes-Olivera, P. A.; van Duin, A. C. T.; Patrito, E. M. *The Journal of Physical Chemistry C* **2018**, *122*, 23515–23527.

(69) Yang, H.; Zheng, X.; Sun, Y.; Yu, K.; He, M.; Guo, Y. *Comput. Mater. Sci.* **2017**, *139*, 48–55.

(70) Sun, H. *Macromolecules* **1995**, *28*, 701–712.

(71) Jansen, M. J.; Jones Jr, W. R.; Pepper, S. V. *Tribol. Lett.* **2003**, *14*, 61–67.

(72) Fusaro, R.; Khonsari, M. *NASA Technical Report* **1993**, *4*, 59–92.

(73) Song, I.; Park, C.; Choi, H. C. *Rsc Advances* **2015**, *5*, 7495–7514.

(74) Roberts, E. W. *Thin Solid Films* **1989**, *181*, 461–473.

(75) Fleischauer, P. D. *Thin Solid Films* **1987**, *154*, 309–322.

(76) Roberts, E. W. *NASA. Lewis Research Center 20th Aerospace Mechanics Symposium* **1986**, 103–119.

(77) Hilton, M. R.; Bauer, R.; Fleischauer, P. D. *Thin Solid Films* **1990**, *188*, 219–236.

(78) Li, H.; Xu, T.; Wang, C.; Chen, J.; Zhou, H.; Liu, H. *J. Phys. D Appl. Phys.* **2005**, *38*, 62–69.

(79) Khare, H. S.; Burris, D. L. *Tribol. Lett.* **2013**, *52*, 485–493.

(80) Voevodin, A. A.; O'Neill, J. P.; Zabinski, J. S. *Surf. Coat. Technol.* **1999**, *116-119*, 36–45.

(81) Voevodin, A. A.; Fitz, T. A.; Hu, J. J.; Zabinski, J. S. *Journal of Vacuum Science & Technology A: Vacuum, Surfaces, and Films* **2002**, *20*, 1434–1444.

(82) Voevodin, A.; Zabinski, J. *Compos. Sci. Technol.* **2005**, *65*, 741–748.

(83) Curry, J.; Argibay, N.; Babuska, T.; Nation, B.; Martini, A.; Strandwitz, N.; Dugger, M.; Krick, B. *Tribol. Lett.* **2016**, *64*, 1–9.

(84) Serles, P.; Sun, H.; Colas, G.; Tam, J.; Nicholson, E.; Wang, G.; Howe, J.; Saulot, A.; Singh, C. V.; Filleter, T. *Adv. Mater. Interfaces* **2020**, 1901870.

(85) John, P. J.; Cutler, J. N.; Sanders, J. H. *Tribol. Lett.* **2001**, *9*, 167–173.

(86) Donnet, C.; Martin, J. M.; Le Mogne, T.; Belin, M. *Tribol. Int.* **1996**, *29*, 123–128.

(87) Tagawa, M.; Ikeda, J.; Kinoshita, H.; Umeno, M.; Ohmae, N. In *Protection of Space Materials from the Space Environment*; Springer Netherlands: Dordrecht, 2001, pp 73–84.

(88) Liang, T.; Sawyer, W. G.; Perry, S. S.; Sinnott, S. B.; Phillpot, S. R. *J. Phys. Chem. C* **2011**, *115*, 10606–10616.

(89) Ross, S.; Sussman, A. *The Journal of Physical Chemistry* **1955**, *59*, 889–892.

(90) Haltner, A. J.; Oliver, C. S. *Ind. Eng. Chem. Fundam.* **1966**, *5*, 348–355.

(91) Pardee, R. P. *Asle Transactions* **1972**, *15*, 130–142.

(92) Panitz, J. K. G.; Pope, L. E.; Lyons, J. E.; Staley, D. J. *J. Vac. Sci. Technol. A* **1988**, *6*, 1166–1170.

(93) Curry, J. F.; Wilson, M. A.; Luftman, H. S.; Strandwitz, N. C.; Argibay, N.; Chandross, M.; Sidebottom, M. A.; Krick, B. A. *ACS Appl. Mater. Interfaces* **2017**, *9*, 28019–28026.

(94) Uemura, M.; Saito, K.; Nakao, K. *Tribol. Trans.* **1990**, *33*, 551–556.

(95) Levita, G.; Righi, M. C. *Chem. Phys. Chem* **2017**, *18*, 1475–1480.

(96) Haider, J. In *Encyclopedia of Tribology*, Wang, Q. J., Chung, Y.-W., Eds.; Springer US: Boston, MA, 2013, pp 2323–2333.

(97) Spalvins, T. *Thin Solid Films* **1982**, *96*, 17–24.

(98) Buck, V. *Wear* **1983**, *91*, 281–288.

(99) Spalvins, T. *Journal of Vacuum Science & Technology A: Vacuum, Surfaces, and Films* **1987**, *5*, 212–219.

(100) Hilton, M. R.; Jayaram, G.; Marks, L. D. *J. Mater. Res.* **1998**, *13*, 1022–1032.

(101) Hilton, M. R. *Surf. Coat. Technol.* **1994**, *68-69*, 407–415.

(102) Manzeli, S.; Ovchinnikov, D.; Pasquier, D.; Yazyev, O. V.; Kis, A. *Nat. Rev. Mater.* **2017**, *2*, 17033.

(103) Lu, K.-Q.; Qi, M.-Y.; Tang, Z.-R.; Xu, Y.-J. *Langmuir* **2019**, *35*, 11056–11065.

(104) Choudhary, N.; Patel, M. D.; Park, J.; Sirota, B.; Choi, W. *J. Mater. Res.* **2016**, *31*, 824–831.

(105) Serles, P.; Gaber, K.; Pajovic, S.; Colas, G.; Filleter, T. *Lubricants* **2020**, *8*, 49.

(106) Das, S.; Kim, M.; Lee, J.-W.; Choi, W. *Crit. Rev. Solid State Mater. Sci.* **2014**, *39*, 231–252.

(107) Efeoglu, I. In *Encyclopedia of Tribology*; Springer US: Boston, MA, 2013, pp 3233–3252.

(108) Buck, V. *Wear* **1987**, *114*, 263–274.

(109) Bichsel, R.; Buffat, P.; Levy, F. *J. Phys. D Appl. Phys.* **1986**, *19*, 1575–1585.

(110) Cicily Rigi, V. J.; Jayaraj, M. K.; Saji, K. J. *J. Vac. Sci. Technol. A* **2022**, *40*, 032201.

(111) Babuska, T. F.; Curry, J. F.; Dugger, M. T.; Lu, P.; Xin, Y.; Klueter, S.; Kozen, A. C.; Grejtak, T.; Krick, B. A. *ACS Appl. Mater. Interfaces* **2022**, *14*, 13914–13924.

(112) Scharf, T. W.; Goeke, R. S.; Kotula, P. G.; Prasad, S. V. *ACS applied materials & interfaces* **2013**, *5*, 11762–11767.

(113) Karkee, R.; Guerrero, E.; Strubbe, D. A. *Phys. Rev. Mater.* **2021**, *5*.

(114) Guerrero, E.; Strubbe, D. A. *arXiv [cond-mat.mtrl-sci]* **2022**.

(115) Singh, H.; Mutyala, K. C.; Mohseni, H.; Scharf, T. W.; Evans, R. D.; Doll, G. L. *Tribol. Trans.* **2015**, *58*, 767–777.

(116) Vellore, A.; Romero Garcia, S.; Walters, N.; Johnson, D. A.; Kennett, A.; Heverly, M.; Martini, A. *Adv. Mater. Interfaces* **2020**, *7*, 2001109.

(117) Prakash, K.; Harish, S.; Kamalakannan, S.; Logu, T.; Shimomura, M.; Archana, J.; Navaneethan, M. *Journal of Energy Chemistry* **2023**, *80*, 335–349.

(118) Mosconi, D.; Till, P.; Calvillo, L.; Kosmala, T.; Garoli, D.; Debellis, D.; Martucci, A.; Agnoli, S.; Granozzi, G. *Surfaces* **2019**, *2*, 531–545.

(119) Wei, H.; Gui, Y.; Kang, J.; Wang, W.; Tang, C. *Nanomaterials (Basel)* **2018**, *8*, 646.

(120) Jenisha, M. A.; Kavirajan, S.; Harish, S.; Archana, J.; Kamalabharathi, K.; Kumar, E. S.; Navaneethan, M. *J. Alloys Compd.* **2022**, *895*, 162493.

(121) Zhao, J.; Jiang, J.-W.; Rabczuk, T. *Applied Physics Letters* **2013**, *103*.

(122) Sirota, B.; Glavin, N.; Voevodin, A. A. *Vacuum* **2019**, *160*, 133–138.

(123) Grigoriev, F. V.; Sulimov, A. V.; Kochikov, I.; Kondakova, O. A.; Sulimov, V. B.; Tikhonravov, A. V. *Int. J. High Perform. Comput. Appl.* **2015**, *29*, 184–192.

(124) Berendsen, H. J. C.; Postma, J. P. M.; van Gunsteren, W. F.; DiNola, A.; Haak, J. R. *J. Chem. Phys.* **1984**, *81*, 3684–3690.

(125) Momma, K.; Izumi, F. *J. Appl. Crystallogr.* **2011**, *44*, 1272–1276.

(126) McConney, M. E.; Glavin, N. R.; Juhl, A. T.; Check, M. H.; Durstock, M. F.; Voevodin, A. A.; Shelton, T. E.; Bultman, J. E.; Hu, J.; Jespersen, M. L. *J. Mater. Res.* **2016**, *31*, 967–974.

(127) Guerrero, E.; Karkee, R.; Strubbe, D. A. *J. Phys. Chem. C Nanomater. Interfaces* **2021**, *125*, 13401–13412.

(128) Hibbs, M. K.; Johansson, B. O.; Sundgren, J.-E.; Helmersson, U. *Thin Solid Films* **1984**, *122*, 115–129.

(129) Moser, J.; Lévy, F.; Bussy, F. *J. Vac. Sci. Technol. A* **1994**, *12*, 494–500.

(130) Hoffman, E. E.; Marks, L. D. *Tribol. Lett.* **2016**, *64*, 1–10.

(131) Scharf, T. W.; Kotula, P. G.; Prasad, S. V. *Acta Materialia* **2010**, *58*, 4100–4109.

(132) Faiyad, A.; Bhuiyan, F. H.; Vellore, A.; Johnson, D. A.; Kennett, A.; Martini, A. *Tribol. Lett.* **2024**.

(133) Huang, C.; Katz, H. E.; West, J. E. *Langmuir* **2007**, *23*, 13223–13231.

(134) Zholdassov, Y. S.; Yuan, L.; Garcia, S. R.; Kwok, R. W.; Boscoboinik, A.; Valles, D. J.; Marianski, M.; Martini, A.; Carpick, R. W.; Braunschweig, A. B. *Science* **2023**, *380*, 1053–1058.

(135) Gutiérrez Moreno, J. J.; Pan, K.; Wang, Y.; Li, W. *Langmuir* **2020**, *36*, 5680–5689.

(136) Zhu, W.; Zheng, G.; Cao, S.; He, H. *Scientific reports* **2018**, *8*, 10537.

(137) Hanwell, M. D.; Curtis, D. E.; Lonie, D. C.; Vandermeersch, T.; Zurek, E.; Hutchison, G. R. *J. Cheminform.* **2012**, *4*, 17.

(138) Martínez, L.; Andrade, R.; Birgin, E. G.; Martínez, J. M. *J. Comput. Chem.* **2009**, *30*, 2157–2164.

(139) Plimpton, S. *J. Comput. Phys.* **1995**, *117*, 1–19.

(140) Soria, F. A.; Zhang, W.; van Duin, A. C. T.; Patrito, E. M. *ACS Appl. Mater. Interfaces* **2017**, *9*, 30969–30981.

(141) Evans, D. J.; Holian, B. L. *J. Chem. Phys.* **1985**, *83*, 4069–4074.

(142) Stukowski, A. *Model. Simul. Mat. Sci. Eng.* **2010**, *18*, 015012.

(143) Adelman, S. A.; Doll, J. D. *J. Chem. Phys.* **1976**, *64*, 2375–2388.

(144) Jas, G. S.; Wang, Y.; Pauls, S. W.; Johnson, C. K.; Kuczera, K. *J. Chem. Phys.* **1997**, *107*, 8800–8812.

(145) Lecot, S.; Lavigne, A.; Yang, Z.; Géhin, T.; Botella, C.; Jousseaume, V.; Chevolot, Y.; Phaner-Goutorbe, M.; Yeromonahos, C. *J. Phys. Chem. C Nanomater. Interfaces* **2020**, *124*, 20125–20134.

(146) Roscioni, O. M.; Muccioli, L.; Mityashin, A.; Cornil, J.; Zannoni, C. *The Journal of Physical Chemistry C* **2016**, *120*, 14652–14662.

(147) Ghorai, P. K.; Glotzer, S. C. *J. Phys. Chem. C Nanomater. Interfaces* **2007**, *111*, 15857–15862.

(148) Aldagari, S.; Hung, A. M.; Shariati, S.; Faisal Kabir, S. K.; Ranka, M.; Bird, R. C.; Fini, E. H. *Constr. Build. Mater.* **2022**, *359*, 129500.

(149) Martyna, G. J.; Klein, M. L.; Tuckerman, M. *J. Chem. Phys.* **1992**, *97*, 2635–2643.